FACULTÉ DES ÉTUDES SUPÉRIEURES ET POSTOCTORALES

uOttawa

L'Université canadienne
Canada's university

FACULTY OF GRADUATE AND POSDOCTORAL STUDIES

Paul Salem
AUTEUR DE LA THÈSE / AUTHOR OF THESIS

M.A.Sc. (Electrical Engineering)
GRADE / DEGREE

School of Information Technology and Engineering
FACULTÉ, ÉCOLE, DÉPARTEMENT / FACULTY, SCHOOL, DEPARTMENT

Dual Polarized Sinuous Antenna and Ultra Wideband Feed Design and Integration
TITRE DE LA THÈSE / TITLE OF THESIS

M. Yagoub
DIRECTEUR (DIRECTRICE) DE LA THÈSE / THESIS SUPERVISOR

CO-DIRECTEUR (CO-DIRECTRICE) DE LA THÈSE / THESIS CO-SUPERVISOR

EXAMINATEURS (EXAMINATRICES) DE LA THÈSE / THESIS EXAMINERS

M. McNamara

A. Petosa

Gary W. Slater
Le Doyen de la Faculté des études supérieures et postdoctorales / Dean of the Faculty of Graduate and Postdoctoral Studies

Dual Polarized Sinuous Antenna and Ultra Wideband Feed Design and Integration

By:

Paul Salem, B. A. Sc.

A thesis submitted to the
Faculty of Graduate and Postdoctoral Studies
in partial fulfillment of the requirements for the degree of

Master of Applied Science
in Electrical Engineering

Ottawa-Carleton Institute for Electrical and Computer Engineering
School of Information Technology and Engineering
Faculty of Engineering
University of Ottawa

Library and
Archives Canada

Published Heritage
Branch

395 Wellington Street
Ottawa ON K1A 0N4
Canada

Bibliothèque et
Archives Canada

Direction du
Patrimoine de l'édition

395, rue Wellington
Ottawa ON K1A 0N4
Canada

Your file Votre référence
ISBN: 978-0-494-25830-9
Our file Notre référence
ISBN: 978-0-494-25830-9

NOTICE:
The author has granted a non-exclusive license allowing Library and Archives Canada to reproduce, publish, archive, preserve, conserve, communicate to the public by telecommunication or on the Internet, loan, distribute and sell theses worldwide, for commercial or non-commercial purposes, in microform, paper, electronic and/or any other formats.

The author retains copyright ownership and moral rights in this thesis. Neither the thesis nor substantial extracts from it may be printed or otherwise reproduced without the author's permission.

AVIS:
L'auteur a accordé une licence non exclusive permettant à la Bibliothèque et Archives Canada de reproduire, publier, archiver, sauvegarder, conserver, transmettre au public par télécommunication ou par l'Internet, prêter, distribuer et vendre des thèses partout dans le monde, à des fins commerciales ou autres, sur support microforme, papier, électronique et/ou autres formats.

L'auteur conserve la propriété du droit d'auteur et des droits moraux qui protège cette thèse. Ni la thèse ni des extraits substantiels de celle-ci ne doivent être imprimés ou autrement reproduits sans son autorisation.

In compliance with the Canadian Privacy Act some supporting forms may have been removed from this thesis.

While these forms may be included in the document page count, their removal does not represent any loss of content from the thesis.

Conformément à la loi canadienne sur la protection de la vie privée, quelques formulaires secondaires ont été enlevés de cette thèse.

Bien que ces formulaires aient inclus dans la pagination, il n'y aura aucun contenu manquant.

Canada

Abstract

The designs of multi-arm planar sinuous antennas and their feeding networks are presented in this thesis for operation from 2-18GHz. The sinuous antenna's superior ultra wideband performance and dual polarization capability makes it ideal for both civil and military applications like direction-finding (DF) systems. The sinuous antennas generate broadside patterns with dual linear or circular polarization over wide beamwidths with good gain over the entire frequency band. The bandwidth of the sinuous antenna is virtually unlimited and is only restricted by the design of the feed network. There has been very little publicized research geared towards this antenna due to its complicated feed network design and integration. In this thesis novel feed designs are presented in the form of ultra wideband balun structures, symmetrical 3dB 90° directional couplers, and their integration into the system. In addition to the specific designs, modifications were made to the sinuous antenna, while new techniques were developed with concentration on theoretical and practical implementation to minimizing size, weight, and costs. The results presented for the performance of the sinuous antenna show improvements over existing designs.

"Only one thing is ever guaranteed,

that is that you will definitely not achieve the goal

if you don't take the shot"

Wayne Gretzky

Acknowledgments

I am truly grateful to the many individuals that have contributed to this research project. It was all of you who made my work so enjoyable.

I would like to thank Emerson & Cuming and Rogers Cooperation for donating all the required material needed for the construction of the designs. The manufacturing of these designs was made possible with the help of the Communications Research Centre (CRC) design and fabrication team, especially Mr. Minh Huynh, who worked closely with me and offered valuable advice on the practical aspect of the implementation and the tolerances.

This work would not have been possible without the generous financial support offered by Defence Research and Development Canada (DRDC). Their cooperation in this project is greatly appreciated.

I would also like to thank the professor who inspired me to pursue my graduate education, the person responsible for most of my electromagnetics knowledge, and the reason why I chose to specialize in this fascinating field of Microwaves and Photonics. Dr. Derek McNamara I thank you for your excellent guidance and support over the past few years.

Special thanks to my good friend, fellow master's student, and future professor, Igor Aćimović. His daily presence, sarcastic remarks, and stimulating discussions and suggestions can be observed throughout this entire thesis.

I am especially grateful to Dr. Chen Wu, who took a big risk two years ago and decided to sponsor me in conjunction with the DRDC. It was he who selected this excellent topic for which I became completely devoted towards. His theoretical support and his drive for perfection has been an invaluable asset.

My deepest gratitude is due to my thesis supervisor, Dr. Mustapha Yagoub, for which his 'my door is always open' policy stayed true until the very end. His presence was all the motivation I needed to put forth my best effort. His technical advice relating to microwave circuits and applied electromagnetics was essential to the success of the project. I consider myself very fortunate to have worked directly with Yagoub as his student and his friend.

Finally, I am forever indebted to all my friends and relatives, especially my parents and sister, Paulette, for all their encouragement and endless patience. This thesis is dedicated to you.

Contrary to the belief of the great philosophers, Wayne and Garth: "You were all worthy".

Table of Contents

List of Figures

List of Tables

List of Symbols

λ	Wavelength
λ_g	Guided wavelength
f	Frequency
ε	Permittivity
ε_r	Relative permittivity
ε_o	Freespace permittivity
μ	Permeability
μ_r	Relative permeability
μ_o	Freespace permeability
Z_0	Characteristic impedance
Z_{0e}	Even mode characteristic impedance
Z_{0o}	Odd mode characteristic impedance
r	Radial distance to a point on the equiangular spiral
θ	Angle with respect to the x axis for the equiangular spiral
a	A constant for the equiangular spiral
β	Angle between the equiangular spiral and a radial line from the origin
$\underline{\delta}$	Angular rotation for the equiangular spiral
τ	Design ratio for the log periodic toothed planar antenna and the log periodic dipole array
W	Width of a tooth for the log periodic toothed planar antenna
R_n	Distance from the apex to the nth element for the log periodic dipole array
L_n	Total length of the nth element for the log periodic dipole array
α'	Half-angle subtended by the ends of radiating elements for the log periodic dipole array
σ	Spacing factor for the log periodic dipole array
d_n	Distance between the nth and (n+1)th element for the log periodic dipole array
N	Number of arms for the sinuous antenna
P	Number of cells for the sinuous antenna
R_p	Outer radius of the pth cell for the sinuous antenna
α_p	Angular width of the pth cell for the sinuous antenna
τ_p	The ratio of the inside to outside radius of the pth cell for the sinuous antenna
δ	Angle used to swing two sinuous curves to create a sinuous arm
k	Coupling factor

C_{dB}	Coupling factor in dB
w	Fractional bandwidth
B	Bandwidth ratio
H	Total thickness for the coupler
H_o	Differential thickness of the two striplines for the coupler
w	Width of the stripline for the coupler
w_o	Line spacing between two striplines for the coupler

List of Acronyms

ADS	-	Advanced Design System
AOA	-	Angle of Arrival
AR	-	Axial Ratio
BLP	-	Balanced-Line Port
BM	-	Balanced Mode
BW	-	Beamwidth
Co	-	Co Polarization
CP	-	Circular Polarization
CRC	-	Communications Research Centre Canada
CRT	-	Cathode Ray Tube
DF	-	Direction Finding
DRDC	-	Defence Research and Development Canada
DUT	-	Device Under Test
EM	-	Electromagnetic
ES	-	Electronic Support
FEM	-	Finite Element Method
HFSS	-	High Frequency Structure Simulator
LCD	-	Liquid Crystal Display
LHCP	-	Left Hand Circular Polarization
LPDA	-	Log-Periodic Dipole Array
LPTPA	-	Log-Periodic Toothed Planar Antenna
LPTTA	-	Log-Periodic Toothed Trapozoidal Antenna
MLP	-	Multi-Layered Perceptron
RADAR	-	Radio Detection and Raging
RAM	-	Random Access Memory
RF	-	Radio Frequency
RHCP	-	Right Hand Circular Polarization
SMA	-	SubMiniature Version A
TEM	-	Transverse Electromagnetic
UBLP	-	Unbalanced-Line Port
UBM	-	Unbalanced Mode
UWB	-	Ultra Wideband
VSWR	-	Voltage Standing Wave Ratio
X	-	Cross Polarization

1. Introduction

1.1 Motivation

A sinuous antenna offers a wide range of advantages for ultra wideband (UWB) systems. It is the first antenna that is planar, frequency independent, and dual linear/circular polarized with a single aperture [1]. The sinuous antennas have been compared with spiral antennas which have been used in the past for similar applications but were limited in bandwidth. This thesis will illustrate how the sinuous antenna can provide characteristics that were not previously available with any other single aperture planar antenna. Such an antenna that can simultaneously provide orthogonal senses of polarization over a theoretically unlimited bandwidth has many advantages for both civil and military applications. Unfortunately, the popularity of the sinuous antenna has been the victim of its feed network design and integration complexity which severely limits the overall system performance. There has been very little publicized research geared towards this antenna and its feed network to spark any industry use or interest. Thus, the motivation of this thesis is to eradicate the general lack of understanding of the practical design and implementation of the complete sinuous antenna system.

1.2 Organization and Contributions of the Thesis

The contributions of this thesis are focused directly on the practical design and implementation of the sinuous antenna and its ultra wideband feed network. This antenna has a primary use in military applications such as Direction Finding and is expected to replace the current spiral antennas used in military aircrafts. Thus, although all the general theory will be discussed and explained for all design specifications, this thesis will focus on the following design criteria:

- 2-18GHz band of operation
- Dual circular polarization
- Wide axial ratio beamwidth

In addition to the main contributions of this thesis, which focus on meeting the above criteria, special precautions were taken to achieve reduction in size and weight of the antenna system. The contributions will now be summarized in sequential order in agreement with the organization of this thesis.

The first chapter discusses the motivation and organization of the thesis while summarizing all the contributions.

The next chapter describes some of the necessary principles and concepts that are vital to the designs presented in the thesis. A systematic literature review and history of frequency independent and broadband planar antennas are summarized. Such a survey attempts to portray the progression in antenna design that led to the development of the sinuous antenna. This chapter then discusses the electromagnetic simulator and the method that was utilized to simulate the designs. A basic graphical representation of the coordinate system for all the radiation patterns used throughout the thesis is included as a reference for the reader.

The sinuous antenna is discussed in detail in the third chapter. Two and four arm sinuous antennas were designed, simulated, analyzed, and manufactured for 2-18GHz operation. High similarity between radiation patterns obtained for various plane cuts illustrated bidirectional broadside patterns along with wide beamwidth, for both linear and circular polarizations. An investigation was performed for unidirectional patterns using a cavity backed sinuous antenna filled with absorbing material. An alternate approach is also discussed where each arm-pair of the four arm structure was printed on different sides of the substrate to allow for easier feed integration. This chapter presents a minor but important modification to the high frequency radiation area which makes it possible to practically incorporate the feed structure.

Chapter four discusses the designs of two different feed networks in the form of baluns for mode transformation and simultaneous impedance matching over the same ultra wideband. The first balun structure was designed using a conventional metallic trace taper. The second was a simpler and shorter novel design using a slot in the ground plane for the mode transformer. This balun established up to a 45% reduction in the total length required for mode transformation and did not show any degradation in performance when compared with the conventional tapered design. Each of the designs exhibited low insertion losses and were used in the feed network for the sinuous antenna. Both designs were manufactured and measured.

The need for circular polarization was the inspiration for the fifth chapter which investigated the design and configuration of a 2-18GHz symmetrical 3dB 90° directional coupler. Two 8.34dB couplers were connected in tandem to create a realizable circuit. A stepped coupler was designed and investigated first. Secondly, a specific taper function was introduced using non-uniform line techniques to enhance the coupler's performance resulting in significant improvements in return loss and isolation as well as phase response. The coupler ports were then adjusted to allow for easy integration with the previous balun designs. The coupler was manufactured and measured.

The final chapter presents the overall system integration of the sinuous antenna, the two baluns, and the coupler. This section presents a new layout for the integration of the coupler with the baluns, which demonstrates clear advantages in its electromagnetic performance, physical size, manufacturing simplicity, and robustness. Such a layout opens up a very interesting area for future research in a completely planar sinuous antenna system. The coupler-balun structure is then integrated with the sinuous antenna to create a new, tightly packed antenna system configuration. The results presented for the performance of the sinuous antenna show improvements over existing designs.

Finally, all the conclusions are summarized along with discussions of future work and further improvements. Special attention was placed on the theoretical and practical development of this antenna system.

The contributions discussed above can all be summarized by the following points:

- The analysis of the two and four arm sinuous antennas and modification of the high frequency radiation feed point.

- The design and construction of a novel ultra wideband balun exhibiting equal or better performance than the traditional tapered balun with approximately half the length.

- An investigation into the transformation from an ultra wideband symmetrical 3dB 90° directional stepped coupler to a carefully tapered coupler using non-uniform line techniques with significant performance enhancement. Much emphasis on the theoretical and practical aspects of its design and construction was placed for a significant reduction in size and weight.

- The introduction of a novel technique to integrate the coupler with two baluns onto a single structure while enhancing the transition with the sinuous antenna for dual circular polarization. Such a device demonstrates advantages in performance such as return loss and isolation while maintaining a structurally simple manufacturing process and reduced overall size.

1.3 Publications Based on the Contributions of the Thesis

1.3.1 Refereed Contributions

- Salem, P., Wu, C., Yagoub, M.C.E., "Non-Uniform Tapered Ultra Wideband Directional Coupler Design and Modern Antenna System Integration", *IEEE MTT-S International Microwave Symposium.* San Francisco, CA. USA. (Pending Acceptance)

- Salem, P., Wu, C., Yagoub, M.C.E., "Neural-Based Model of Spiral Antenna Radiation Patterns for Detection of Angle of Arrival", *IEEE International Workshop on Antenna Technology: Small Antennas and Novel Metamaterials.* White Plains, NY. USA. (Publication Date: March 2006)

- Salem, P., Wu, C., Yagoub, M.C.E., "Novel Ultra Wideband Printed Balun Design using the FEM and FDTD Methods", *IEEE Antennas and Propagation Society International Symposium. Washington*, DC. USA. July 2005.

- Salem, P., Wu, C., Yagoub, M.C.E., "Four Arm Dual Circular Polarized Sinuous Antenna Design for 2-18GHz Operation", *IASTED International Conference on Antennas, Radar, and Wave Propagation.* Banff, AB. Canada. Vol. 2, 377-382. July 2005.

1.3.2 Non-Refereed Contributions

- Salem, P., Yagoub, M.C.E., "Dual Polarized Sinuous Antenna and Ultra Wideband Feed Design", Defence Research and Development Canada Contracted Report. Document Number: CR 2005-035. 2005.

- Salem, P., Yagoub, M.C.E., "Use of Neural Networks to Model Spiral Antenna Radiation Patterns", Defence Research and Development Canada Contracted Report. Document Number: CR 2005-024. 2005.

2. Literature Review

2.1 Frequency Independent Antennas

The theoretical foundation of frequency independent antennas was laid down by Rumsey at the University of Illinois [2]. The pattern characteristics and the impedance of any radiating antenna can be determined by its specific shape and size in terms of wavelength at a given operating frequency. A frequency independent antenna is an antenna that does not change its properties when scaled arbitrarily to a smaller or larger size. This would hold only if the scaled structure remains the same as the original or its rotated form. Thus, by Rumsey's principle, the impedance and pattern properties of any antenna will in fact be frequency independent if the antenna geometry is specified entirely by angles irrespective of any particular dimensions. This implies that the electrical characteristics of the antenna do not change with frequency.

2.2 Log-Periodic Concept

A development that closely paralleled the concept of frequency independent antennas was the log-periodic antennas introduced by DuHamel and Isbell in 1957 [3]. If an antenna is transformed to itself or its rotated form when scaled by a specific constant τ, it would become a periodic function with identical characteristics at frequencies f and τf. Since the period of the periodic function is of the logarithmic form ($|\log\tau|$), we call these antennas log-periodic [4]. A log-periodic antenna is said to be defined by angles and a scale factor τ. By setting τ close to unity, we can limit the deviation of performance within the desired band. If τ and/or the angles were to depend on a specific parameter of the dimensions of the antenna it would be referred to as quasi-log-periodic.

2.3 Self Complementary Condition

The self-complementary condition specifies that when a planar conducting strip is interchanged with the non-conducting surface, the structure remains identical to a rotated version of the original. Babinet's principle demonstrates that any self-complimentary structure would maintain a frequency independent input impedance [7]. This is because if the input impedances of the original and complimentary structure are the same, their product will always be a constant regardless of the frequency.

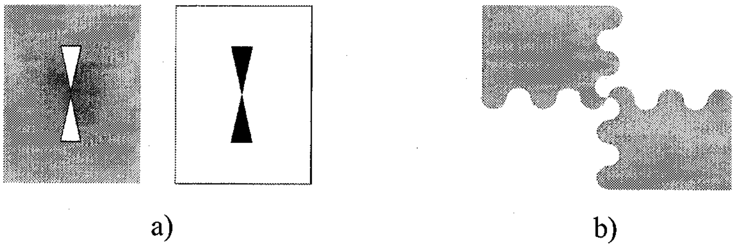

Figure 1. Examples of (a) Complementary Pair, (b) Self-Complementary

2.4 Broadband and Frequency Independent Antenna Review

Since the early 1940s wideband antennas have been the main focus of research and design. In 1943, Schelkunoff designed the biconical antenna and explained its performance using Maxwell's equations [8]. He also presented analytical equations for antenna impedance characteristics for several antenna structures of similar shape to the biconical. Biconical antennas are still widely utilized for broadband applications and have triggered various new designs such as the planar bow-tie antenna designed by Brown and Woodward in 1952 [2]. In the late 1950s, the spiral antennas were introduced in the class of frequency independent antennas, pioneered by the research of Rumsey. The Equiangular and Archimedean spirals were the first to be introduced and still remain as the two most popular spirals. Spiral antennas can achieve up to 10:1 bandwidths, providing circular polarization in a small, low-profile geometry [2][4]. As the spiral antennas were being optimized, DuHamel and Isbell designed the first ever successful log-periodic antenna incorporating a planar self-complimentary structure consisting of two angular strips supporting curved teeth [4]. In 1982, DuHamel then went on to invent and patent the sinuous antenna which was based on the log-periodic principle and inspired by the limitation of the spiral antennas, which could not achieve dual polarization over wide bands.

A broadband antenna that can simultaneously provide orthogonal senses of polarization has been of particular interest for many years. Different techniques have been realized to achieve such requirements using crossed log-periodic dipole arrays and specifically configured spiral antennas with minimal success. Some of the common problems were due to an impractical size of the antenna, E and H plane radiation pattern beamwidths did not match, or simply were not frequency independent [4][9]. Two and four arm spiral antennas have been configured to achieve dual polarization by modifying the feeding networks. In either case, the bandwidth achieved was less than 3:1 [9]. To enhance the bandwidth, one could add more arms; however this would complicate the feed network to the point of impracticality.

When Duhamel invented the sinuous antenna, he realised that a circumferential current distribution should help align the E and H plane radiation pattern beamwidths [4]. In order to keep the overall size of the antenna at a minimum, he designed an interleaved configuration. In the end, the sinuous antenna preserved the advantages of the spiral antenna, such as its small size, low-profile, good beamwidth, and gain, while providing dual linear or dual circular polarization over extreme bandwidths.

2.4.1 Biconical Antenna

The concept of the biconical antenna is based on the fact that the thicker the radiating element, or wire, the wider the impedance bandwidth. If the conductors were flared the bandwidth would be even further increased [10]. The biconical antenna was not planar, nor was it capable of ultra wide bandwidth, but it was one of the key antennas to pioneer the research towards increasing bandwidth capabilities.

2.4.2 Bow-Tie Antenna

The bow-tie antenna (Figure 2) is a planar structure based on the finite biconical antenna. It incorporates the general shape with the advantage of simpler geometry allowing less weight and cost of production. The bow-tie antenna provides dipole-like omni-directional broadside patterns with a bandwidth greater than 2:1.

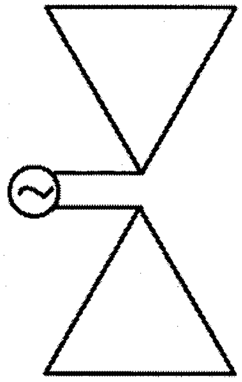

Figure 2. Bow-Tie Antenna

2.4.3 Spiral Antenna

2.4.3.1 Equiangular Spiral

Dyson constructed the first spiral antenna in 1958 based on the following equations obtained for the Equiangular or log spiral curve [2]:

$$r = a^{\theta} \quad or \quad \ln r = \theta \ln a \tag{1}$$

where, referring to Figure 3,
$r =$ *radial distance to point P on spiral*
$\theta =$ *angle with respect to x axis*
$a =$ *a constant*

The radius of the spiral and the width of each arm increases exponentially with a rotation angle. We can then determine the rate of change of radius with angle:

$$\frac{dr}{d\theta} = a^{\theta} \ln a = r \ln a \tag{2}$$

β is the angle between the spiral and a radial line from the origin given by:

$$\ln a = \frac{dr}{rd\theta} = \frac{1}{\tan \beta} \tag{3}$$

Thus,

$$\theta = \tan \beta \ln r \tag{4}$$

An example of a log spiral curve is shown in Figure 3 [11] with r=1 at θ=0 and r=2 at θ=π. From the above equations, the constant *a* and the angle β are determined to be 1.247 and 77.6° respectively.

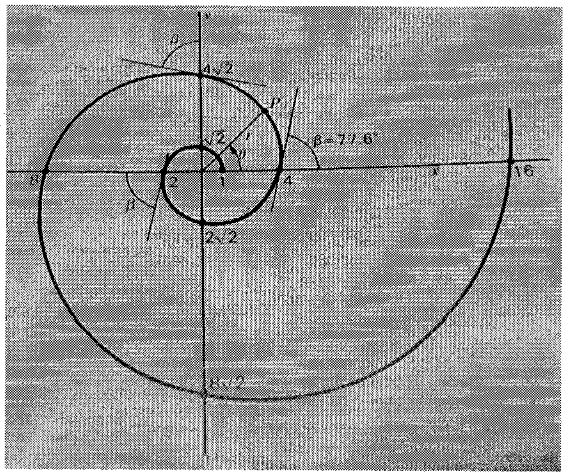

Figure 3. Log Spiral Curve

We can then use δ as an angular rotation to create the spiral from the curve. The geometry of spiral antenna illustrated in Figure 4 [11] is created from the following curves:

$$r_1 = a^{\theta} \qquad r_2 = a^{\theta-\delta} \qquad r_3 = a^{\theta-\pi} \qquad r_4 = a^{\theta-\pi-\delta}$$

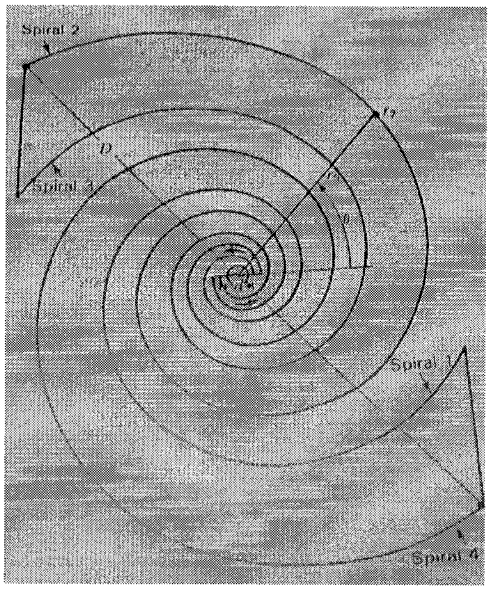

Figure 4. Equiangular Spiral Antenna

If δ is set to π/2 we have four spirals at 90° angles with metallization between spirals 1-4 and 2-3 as shown in the diagram. The outer radius of this antenna is approximately $\lambda_L/4$, where λ_L is the wavelength of the lowest frequency of operation. The spiral antenna is circularly polarized with a beamwidth of approximately 60°-90° over a bandwidth as wide as 8:1.

2.4.3.2 Archimedean Spiral

The Archimedean spiral antenna (Figure 5) is the more popular of the two spirals which was defined back in the third century B.C. by Archimedes of Syracuse. Although this antenna is even more broadband than the equiangular antenna, obtaining bandwidths up to 10:1, it does not officially adhere to the frequency independence principle. This is because the spacing between each arm is specified by a constant as opposed to an angle. However, a tight Archimedes spiral becomes a near approximation of a tightly curled equiangular spiral [2].

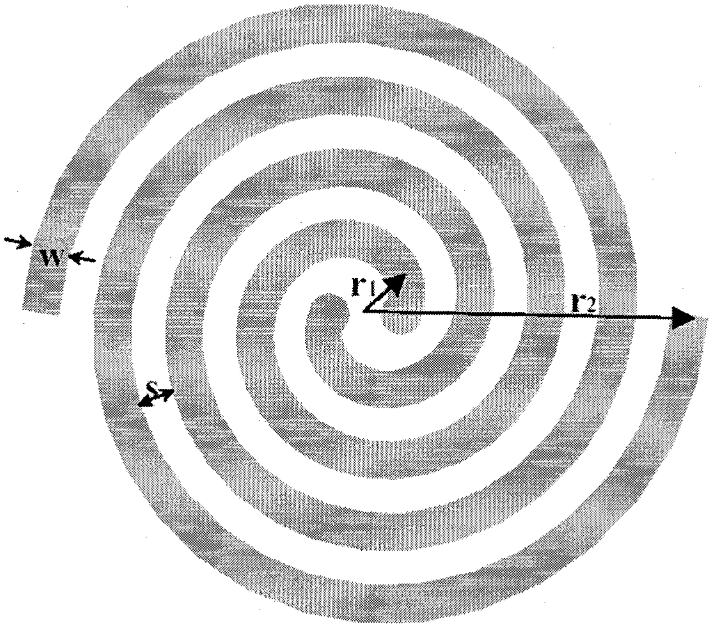

Figure 5. Archimedean Spiral Antenna

The Archimedean spiral is designed to radiate at the region where the circumference of the spiral equals one wavelength. This is called the active region of radiation. Each arm of the spiral is excited 180° out of phase with respect to one other, so that for the active region of radiation, the currents at complementary points on each arm of the spiral add constructively in the far field.

2.4.4 Log-Periodic Antenna

The log periodic antennas evolved from the concept of frequency independent antennas whose theoretical foundation was laid out by Rumsey. Rumsey's work became the motivation for the development of log-periodic antennas by his student, DuHamel, which then resulted in the introduction of the well known Log-Periodic Dipole Antenna (LPDA) by Isbell [3][12][13]. Its development was the result of two previous designs using the log periodic principles: Log-Periodic Toothed Planar Antenna (LPTPA) and the Log-Periodic Toothed Trapezoidal Antenna (LPTTA).

2.4.4.1 Log-Periodic Toothed Planar Antenna (LPTPA)

The LPTPA (Figure 6) was the first log-periodic antenna. It respects the angle criteria such that if the width of one tooth is W_O the next smaller ones would have widths τW_O, $\tau^2 W_O$, $\tau^3 W_O$ and so on [14]. Thus if the width of the widest tooth is W_1, then the width of the n^{th} tooth, W_n is:

$$\begin{gathered} W_n = W_1 \tau^n \\ where\ \tau = \frac{W_{n+1}}{W_n} \end{gathered} \tag{5}$$

Each width is approximately a quarter wavelength wide at its respective frequency or active region of radiation. If we take the logarithm of the tooth-width relation we observe that $\log W_n$ increases periodically and hence the name log-periodic. It can also be shown that the electrical properties of this antenna at a frequency f_O will be repeated at all frequencies by $\tau^n f_O$.

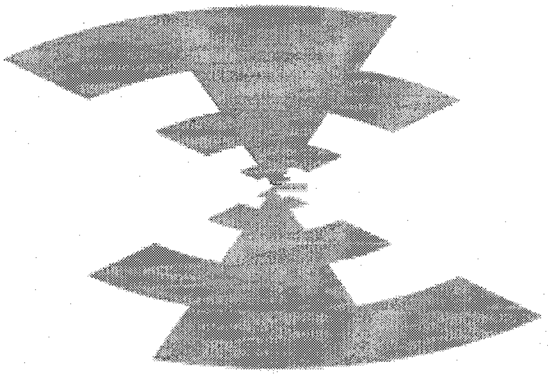

Figure 6. Log-Periodic Toothed Planar Antenna [3]

2.4.4.2 Log-Periodic Toothed Trapezoidal Antenna (LPTTA)

The LPTPA was then slightly modified to obtain the LPTTA as depicted in Figure 7. Although these two antennas are similar in principle, the LPTTA is said to be the earliest link to the onset of the discovery of the LPDA.

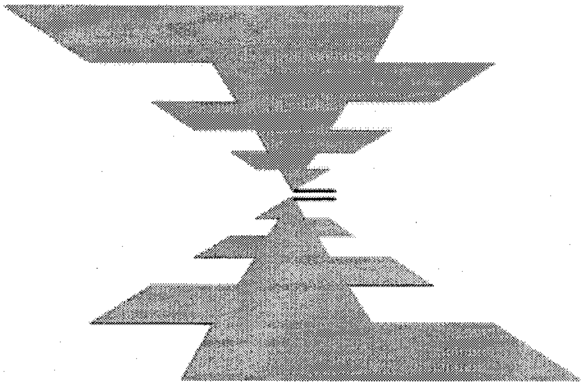

Figure 7. Log-Periodic Toothed Trapezoidal Antenna [3]

2.4.4.3 Log-Periodic Dipole Array (LPDA)

The LPDA is a wideband antenna with moderate gain constructed out of an array of dipole elements. As shown in Figure 8, the successive dipoles are connected alternately to a feeder which is a balanced transmission line. At a given frequency, radiation energy will travel along the feeder until it arrives at an active region of radiation for which the electrical lengths of the elements and phase relationships are optimum [10]. As frequency is swept, the resonating element is replaced by its adjacent.

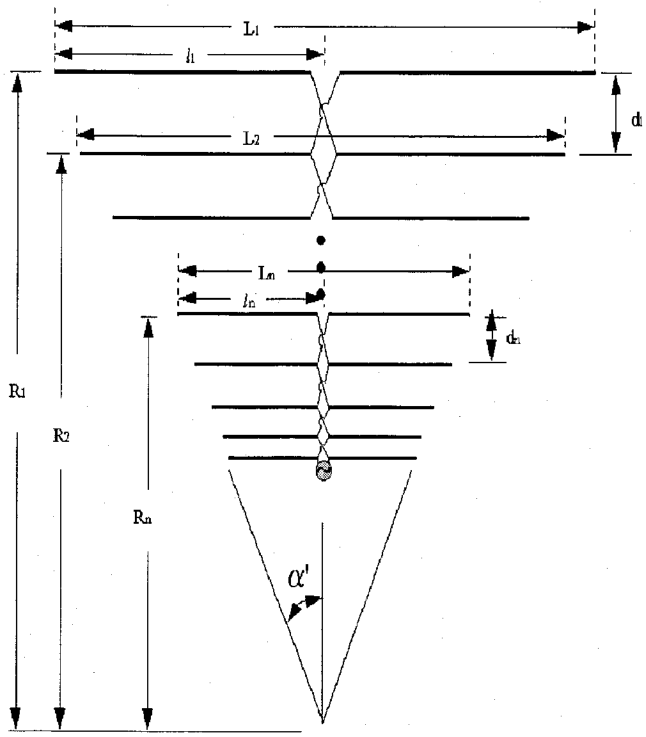

Figure 8. Log-Periodic Dipole Array [3]

The design parameters used to describe the geometry of the LPDA are τ, $\alpha`$, and σ. If the element dipole lengths and distances are represented by L_n and R_n respectively for the nth dipole element [3], then:

$$\frac{L_1}{R_1} = \frac{L_n}{R_n} = 2\tan\alpha` \qquad (6)$$

where,
R_n = *distance from apex to the* n^{th} *element*
L_n = *total length of the* n^{th} *element*
$\alpha`$ = *half-angle subtended by the ends of radiating elements*
τ = *design ratio*
σ = *spacing factor*

The distance between the nth and (n+1)th element is also an important parameter which is denoted by d_n.

$$\frac{d_{n+1}}{d_n} = \frac{R_{n+1}}{R_n} = \tau \qquad (7)$$

The spacing factor, σ, can be expressed in terms of τ and $\alpha`$.

$$\sigma = \frac{1-\tau}{4\tan\alpha`} \qquad (8)$$

2.4.5 Sinuous Antenna

The sinuous antenna was invented in 1982 by R. H. Duhamel and is considered to be one of the most recent frequency independent antennas. It offers a wide range of advantages such as wide bandwidth and dual linear or dual circular polarization with a low-profile planar geometry. Such features are very attractive in numerous military and civil applications, most specifically, direction finding (DF) and reflector feeds. This antenna was inspired by the limitation of the spiral antenna which could not achieve dual polarization over wide bandwidths. Spiral antennas have been used for DF applications with some success. Appendix A includes a complete analysis on the modeling of two element spiral antennas using neural networks. In this study we modeled very basic parameters of the measured results for frequencies varying from the S to Ku bands to illustrate the effectiveness of a multi-element array. The networks that were designed were used to predict the amplitude and phase of the spiral antenna radiation fields at a given radiation direction, based on the knowledge of polarization, frequency, zenith angle (θ), and azimuth angle (ϕ). The motivation for such a task was to replace the traditional 'look-up table' in electronic support (ES) receivers with an automated program. An additional, more practical model, was also created to predict the angle of arrival (AOA) of an incoming wave based on the measured results of adjacent antenna element's received power ratios. Such work is included in Appendix A to stimulate interest in current applications. The sinuous antenna preserves all the benefits of the spiral antennas, but can achieve the opposite sense of polarization at the same time.

In the past, linear polarization has generally been the main application for the sinuous antenna due to its relatively simple implementation. This antenna has been practically ignored for its true advantage in its dual linear and dual circular polarization abilities due to its complicated feed network. The sinuous antenna will be thoroughly discussed in the next chapter and practical feed network design and integration will be provided throughout the thesis.

Before we discuss the sinuous antenna in greater detail, we will first introduce the software package that was utilized to evaluate the electromagnetic performance.

2.5 High Frequency Structure Simulator (HFSS™)

The designs, optimizations, and simulations were all preformed using the Ansoft HFSS™ [15] electromagnetic (EM) simulator. This software was chosen because it is one of the industry leading 3D EM software tools for radio frequency (RF) applications. HFSS uses the finite element method (FEM) to solve Maxwell's equations for the particular problem based on the specified boundary conditions, port excitations, materials, and the specific geometry of the structure. Each problem is set up in a similar manner:

- Indicating the solution type:
    - Driven solution
    - Eigenmode solution
- Constructing the geometry:
    - Manually draw
    - Automated macro language
- Setting up the materials of all three dimensional structures
- Setting up the boundary conditions of the problem

- Setting up the solution:
    - Adaptive frequency
    - Number of adaptive passes and convergence criteria
    - Frequency sweep
- Solving the solution
- Post process analysis
    - Radiation patterns, electric / magnetic fields, current distributions
    - S-parameters
    - Axial ratio, directivity, and gain

The finite element method is a solution space solver which requires an enclosed volume to perform all necessary calculations. HFSS defines this volume as a radiation box and applies explicit radiation boundary conditions on all its sides. The box is supposed to emulate infinite space and hence should be made large enough. The trade-off between accuracy and computer resources is based on the size of this box relative to the design structure. One needs to minimize the box size while ensuring accurate results. Ansoft Corporation recommends that the sides of the radiation box be kept approximately one quarter wavelength at the lowest frequency away from any radiating interfaces of the design structure. In the case of wideband structures, or in our case, ultra wideband structures, it becomes somewhat impractical to size the box for the lowest frequency. For the structures discussed in this thesis, some compromises were required to form a balance between precision and computer resources without jeopardizing the overall accuracy. All simulations were performed on a Pentium-4 3.2GHz computer equipped with 2.5GB RAM.

2.6 Antenna Radiation Patterns

The radiation pattern of an antenna is a graphical representation of the radiation characteristics of the antenna as a function of angles (θ and ϕ). These patterns are specified in spherical coordinates taken in the far-field region of the antenna where the magnitudes of electric and magnetic fields have inversely proportional dependence on distance (r). Many references will be made towards the dependence of the patterns on such angles throughout this thesis and thus a graphical representation is illustrated in Figure 9 as a reference for the reader.

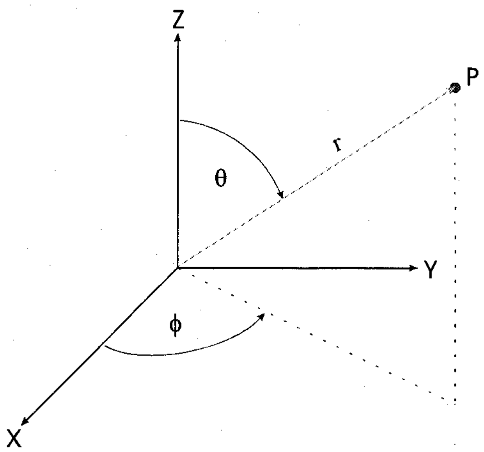

Figure 9. Spherical Coordinate System

$0 \leq \theta \leq \pi$ and $0 \leq \phi \leq 2\pi$

For the remainder of this thesis, all antennas should be assumed to be centred at the origin and lay flat in the xy plane. An antenna, such as the sinuous antenna is a bidirectional broadside antenna. By referring to the above figure, two oppositely directed radiation lobes pointing in the positive and negative z-direction are represented using $\theta=0^\circ$ and $\theta=180^\circ$ respectively.

The two dimensional radiation patterns presented in this thesis will be taken at two sets of principle cuts, primarily $\phi=0^\circ$ and $\phi=90^\circ$ and secondly at $\phi=45^\circ$ and $\phi=135^\circ$. This should provide full description of the overall three dimensional performance of the antenna.

3. Sinuous Antenna Design

3.1 Sinuous Curve and Design Parameters

The sinuous antenna is a frequency independent log-periodic or quasi-log periodic structure, which implies that it is defined by angles and a design ratio tau (τ). The antenna is constructed with N 'arms' comprised of P 'cells' that are scaled in size with respect to one another. The p^{th} cell can range from the first, outer most, and largest cell to the inner most cell P. R_p represents the outer radius of the p^{th} cell.

The design parameters of the sinuous curve are α_p and τ_p, where α_p is a positive number defining the angular width and τ_p is the ratio of the inside to outside radius of cell p or R_p/R_{p-1}. If α and τ are constant, the sinuous curve respects the log-periodic principle. If α_p and τ_p are dependent on the cell number we can call the structure quasi-log-periodic.

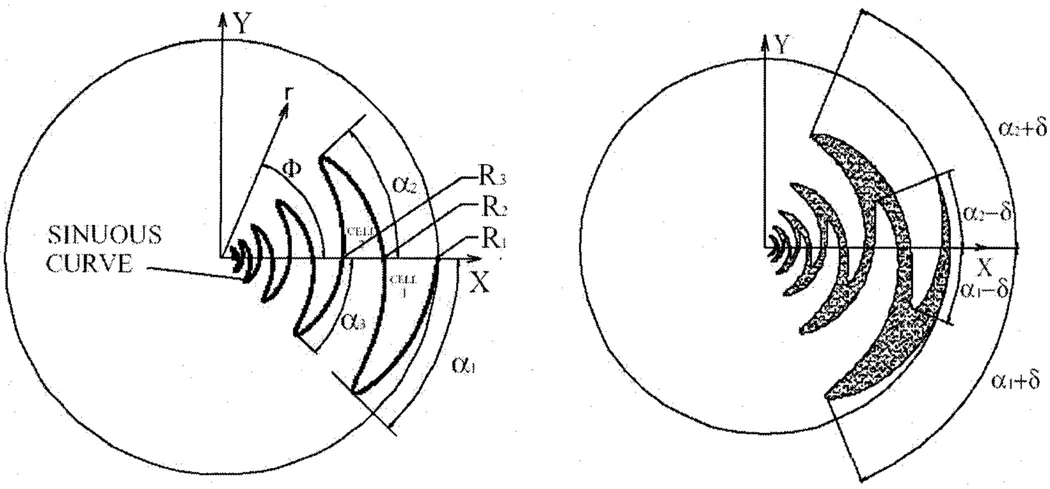

a) Sinuous Curve b) Sinuous Arm

Figure 10. Sinuous Geometry [7]

The sinuous curve equation as defined in [2, 4], for the pth cell can be written as:

$$\phi = (-1)^{p} \alpha_{p} \sin\left[\frac{180 \ln(r/R_{p})}{\ln(\tau_{p})}\right] \qquad R_{p+1} \leq r \leq R_{p} \tag{9}$$

and is shown in Figure 10a.

To generate the sinuous arm from the sinuous curve, we need to introduce one more parameter delta (δ). Figure 10b demonstrates how $\alpha_p \pm \delta$ can be used to swing two sinuous curves to create an arm.

The sinuous arm equation for the pth cell can be written as:

$$\phi = (-1)^{p} \alpha_{p} \sin\left[\frac{180 \ln(r/R_{p})}{\ln(\tau_{p})}\right] \pm \delta \qquad R_{p+1} \leq r \leq R_{p} \tag{10}$$

Although the above-mentioned design parameters are left up to the user to specify, there are some conditions and limitations that one needs to consider. The sum of α_p and δ will affect the overall efficiency, gain, and frequency response of the antenna and thus should be selected carefully. It is said that $\alpha_p + \delta < 70^\circ$ will ensure good gain and efficiency [4][9].

δ also plays an important role in the frequency independence of the antenna as it is the parameter that satisfies the self-complementary condition for an N arm sinuous antenna:

$$\delta = \frac{180}{2N} \tag{11}$$

The input impedance of each antenna arm-pair of a self complementary structure is given by:

$$Z = \frac{60\pi}{\sin\left(\frac{180}{N}\right)} \; [\Omega] \tag{12}$$

In practice, this value is expected to be somewhat less when including the effects of the relative permittivity of the substrate.

The bandwidth of the antenna will directly depend on the physical size of the radius of the sinuous curve. From the approximate relation shown below, one can obtain R_1 and R_P based on the desired lower and upper frequency limits.

$$2r(\alpha_p + \delta) \approx \frac{\lambda}{2} \tag{13}$$

Thus,

$$R_1 = \frac{\frac{\lambda_L}{4}}{(\alpha_p + \delta)} \qquad R_P = \frac{\frac{\lambda_H}{4}}{(\alpha_p + \delta)} \tag{14}$$

where λ_L and λ_H represent the lower and upper frequencies within the desired bandwidth. It will soon be shown that in the case of R_P, it may be beneficial to further reduce the radius by half. This is a direct consequence of the balanced feed needed to join opposing arms of the antenna.

Discussions were made earlier about the significance of the expansion ratio, τ, which defines the ratio of the inside to outside radius of each cell. In the section where the Log-Periodic concept was discussed, we claimed that defining τ close to unity would minimize frequency deviations. To further investigate the design parameter τ and visually validate this claim, we plotted the sinuous curve using constant design parameters with the exception of a varying τ. As τ approaches unity, the number of cells increases and thus creates a less gradual change in electrical length between each radiating region. It is precisely this property that creates a higher resolution in frequency radiating regions. As a designer, a compromise must be made between the size of the arm, the amount of coupling between adjacent arms, the number of cells, the amount of loss, and the amount of frequency radiating resolution.

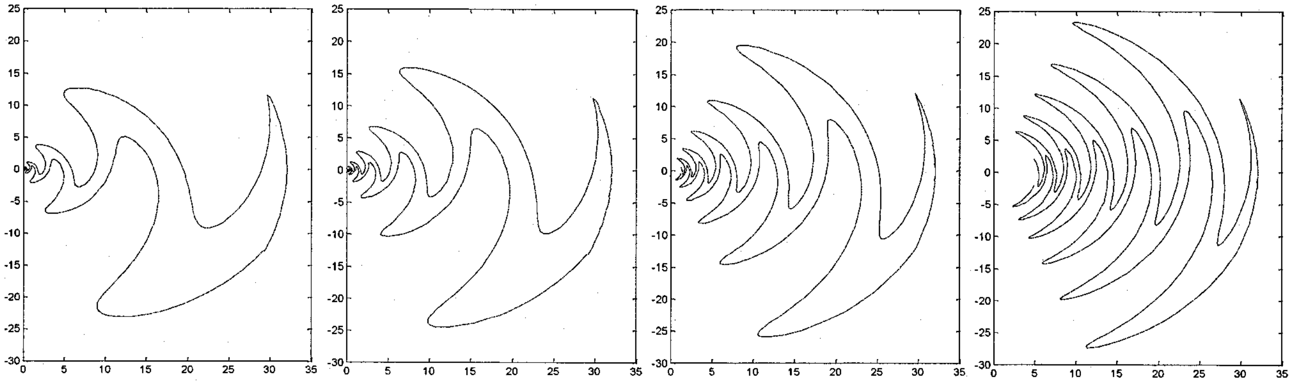

$\tau = 0.55$ $\tau = 0.65$ $\tau = 0.75$ $\tau = 0.85$

Figure 11. Expansion Ratio Variation

3.2 Sinuous Antenna Design

The ultimate objective is to research, design, and manufacture a unidirectional, low-profile, frequency independent antenna that provides good gain and beamwidth with dual circular polarization over a band of 2-18GHz. To meet the desired requirements, four arm sinuous antennas will be designed for bidirectional operation, and a cavity backed sinuous antenna will be investigated for unidirectional operation. In designing the sinuous antenna, a rigorous design methodology was applied using a step-by-step approach summarized below:

- A Matlab code was created to generate the sinuous curve based on user-specified parameters.
- The sinuous arm was designed using a self-complementary structure for a frequency range of 2-18GHz.
- Modifications were made to the geometry of the feed location region to help realize a practical feed network.
- Free-space simulations were performed and analyzed for bidirectional performance.
- Different substrates with different thicknesses were investigated, simulated, and analyzed for bidirectional performance.
- Different cavity depths and absorbing materials were investigated, simulated, and analyzed for unidirectional performance.

Before designing the four arm sinuous antenna an investigation of the two arm structure will be performed. The two arm antenna shares many of the properties as the four arm design but is limited to linear polarization. In many applications, where circular polarization is not required, the two arm structure is preferred due to its relatively simple feed network.

3.3 Generating the Geometry

To generate a single sinuous arm, a Matlab code was created using the equations presented in an earlier section. The code relies on the user to specify the basic design parameters such as:

- Number of cells per arm (P)
- Angular width (α)
- Inside to outside radius ratio (τ)
- Rotation angle (δ)
- Outer radius (R_1)

The output of the Matlab code is in the form of (x, y, z) coordinates used to generate the geometry of the sinuous curves. A secondary code using the HFSS 8.5 macro language was created to utilize the Matlab output to create the geometry inside the HFSS simulator and set up the problem. An additional code was also created using Visual C++ as a top-level control environment for the user. This code performed system tasks such as creating system files, reading the Matlab file, calling and writing to the macro code, and most importantly setting up all the pre-processing tasks, such as boundary conditions and port excitations. This procedure, beginning from the creation of the geometry in Matlab to the point of simulation in HFSS was made entirely automatic. More information on this automated procedure is provided in Appendix B.

3.4 Sinuous Antenna Specific Design and Modification of Feed Point

To design a single arm-pair for the sinuous antenna, the design procedure was followed using the previously mentioned equations. For $\alpha=45^{\circ}$, $\delta=22.5^{\circ}$, and $\tau=0.75$ the inner and outer radius of the sinuous arm was obtained.

Calculating the free space wavelength we can estimate the desired dimensions:

$$\lambda_L = \frac{c}{f_L} = \frac{3\cdot10^8}{2\cdot10^9} = 150mm \rightarrow 5905.5mil$$

$$\lambda_H = \frac{c}{f_H} = \frac{3\cdot10^8}{18\cdot10^9} = 16.66mm \rightarrow 655.9mil$$

$$R_1 = \frac{\frac{\lambda_L}{4}}{\left(\alpha_p + \delta\right)} = \frac{\frac{150\cdot10^{-3}}{4}}{45+22.5}\cdot\frac{180}{\pi} = 31.83mm \rightarrow 1253.1mil$$

$$R_P = \frac{\frac{\lambda_H}{4}}{\left(\alpha_p + \delta\right)} = \frac{\frac{16.66\cdot10^{-3}}{4}}{45+22.5}\cdot\frac{180}{\pi} = 3.53mm \rightarrow 139.0mil$$

A two arm sinuous antenna, shown in Figure 12, was created using a nine cell arm (P=9). The radiation patterns of this antenna were somewhat unsatisfactory at the upper frequency range, due to a reduced beamwidth. To further investigate, special attention was focused at the high frequency radiation area of the antenna, which is the centre of the antenna where the feed port was placed. By zooming in on the mid section of the antenna, Figure 12 highlights the source of the problem.

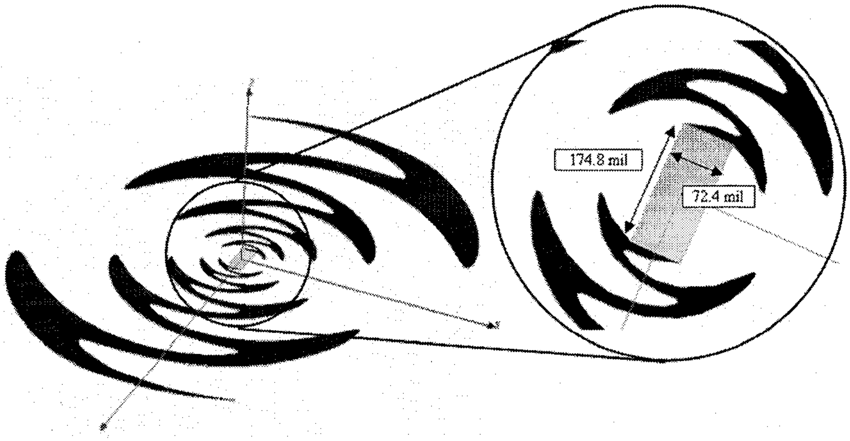

Figure 12. Feed Point Magnification of 9 Cell Two Arm Sinuous Antenna

This design was considered to be impractical and required modifications due to its feed. Ideally, each arm should be fed 180° out of phase from each other at a single feed point. The current design has an oversized feed point of width 72.4mil; this is too large and represents more then 10% of the upper frequency wavelength and will deteriorate performance at such frequencies. For this geometry, the width cannot be reduced without sacrificing the symmetry of the adjacent arms and further diminishing the performance. The solution to this will be presented following the analysis of a secondary problem which lies in the differential length of the feed.

The feed length of 174.8mil raises an impracticality issue with the design of the balun feed network. This differential length of the balanced feed would require a balun thickness close to 174.8mil, which is not a practical design. The length is a direct consequence of the calculation of R_P, representing the inner arm radius at 18GHz. This impracticality has been documented before [4], and in this thesis we will suggest a compromise by reducing the inner radius to half of the previously calculated value. Theoretically this should only enhance the performance by increasing the overall bandwidth while decreasing the differential length of the balun feed point.

Recalculating R_P:

$$R_P = \frac{\frac{\lambda_H}{8}}{(\alpha_p + \delta)} = \frac{\frac{16.66 \cdot 10^{-3}}{8}}{45 + 22.5} \cdot \frac{180}{\pi} = 1.77mm \rightarrow 69.5mil \qquad (15)$$

This inner radius is half the size of the previous radius cutting the feed length in half. In addition to the reduced radius, some other modifications were made at the contact point to further reduce the feed contact size without hurting the symmetry of the structure. The modification creates a transition region to allow a smooth transition from the balanced line port of the balun to the first radiating element of the antenna. The new arm is shown in Figure 13 and now contains 11 cells.

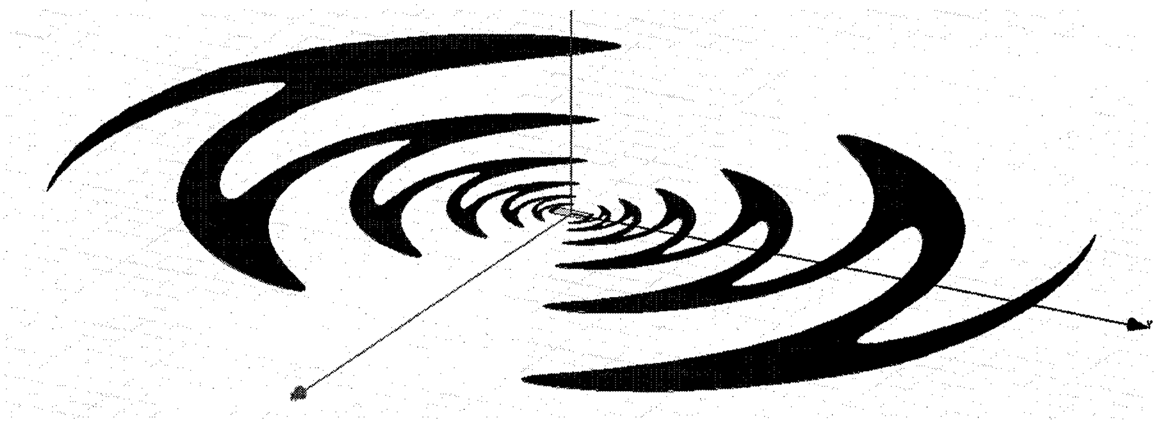

Figure 13. Improved Two Arm Sinuous Antenna

Figure 14 portrays a close up of this new feed design, which clearly illustrates not only the new dimensions, but also the difference in the contact points of the feed. This slight modification allows for an enhanced feed structure while keeping the symmetry intact.

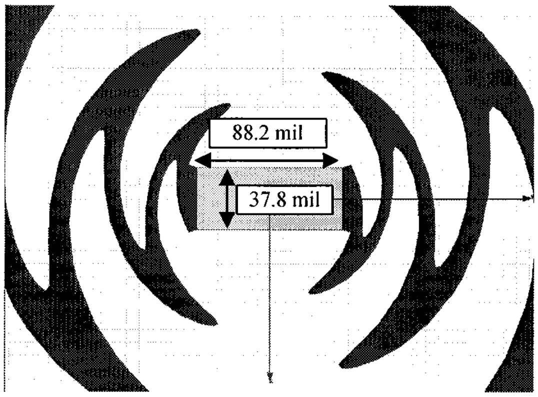

Figure 14. Feed Point Magnification of Improved Two Arm Sinuous Antenna

3.5 Two Arm Sinuous Antenna Simulated Results

The performance of the two arm sinuous antenna (Figure 13) was investigated using HFSS 9.2. All simulations were performed using an 18GHz adaptive meshing algorithm. To monitor the performance of the antenna over the 2-18GHz band, the phi directed electric fields (E_ϕ) and the theta directed electric fields (E_θ) were plotted for the two sets of principle cuts $\phi=0^\circ$ and $\phi=90^\circ$ as well as $\phi=45^\circ$ and $\phi=135^\circ$. These fields are shown in Figure 15.

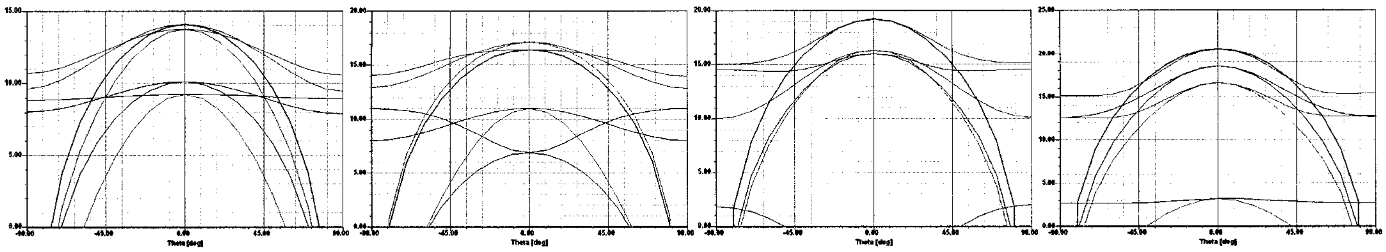

2GHz 3GHz 4GHz 5GHz

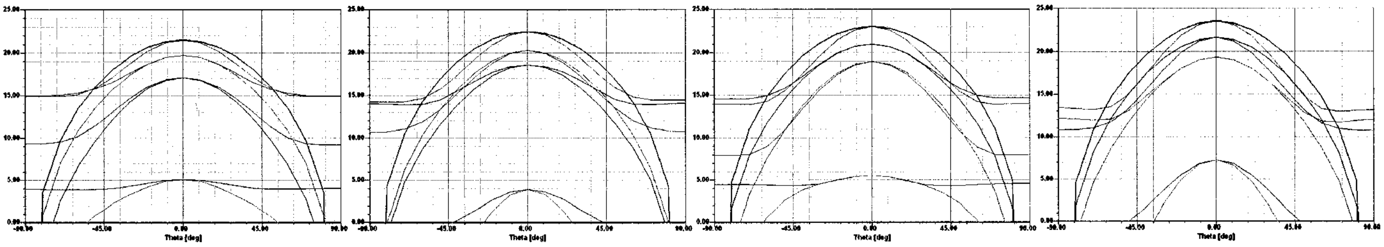

6GHz 7GHz 8GHz 9GHz

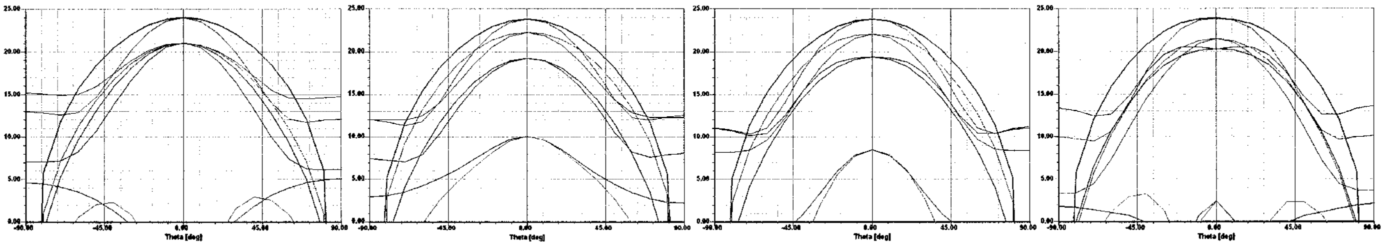

10GHz 11GHz 12GHz 13GHz

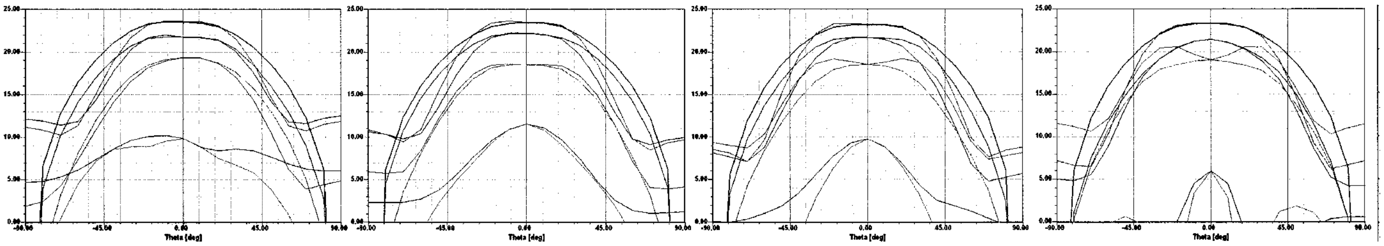

14GHz 15GHz 16GHz 17GHz

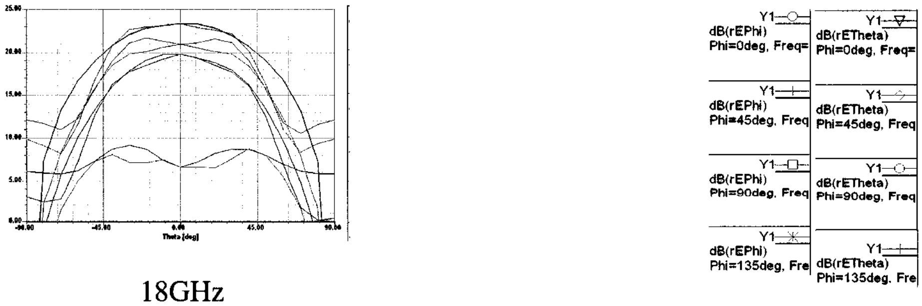

18GHz

Figure 15. Radiation Patterns for Two Arm Sinuous Antenna

In order to properly analyze the radiation patterns we refer back to the spherical coordinate system and the two arm antenna illustrated in Figure 13. From the radiation patterns of the two arm sinuous antenna and the included legend, we can conclude that at broadside:

$$\left|E_{\phi}\left(\phi = 0^{o}\right)\right| = \left|E_{\theta}\left(\phi = 90^{o}\right)\right| \qquad \textit{Cross Polarization}$$

$$\left|E_{\theta}\left(\phi = 0^{o}\right)\right| = \left|E_{\phi}\left(\phi = 90^{o}\right)\right| \qquad \textit{Co Polarization}$$

This is precisely as one would expect since the two arms shown in Figure 13 are oriented along the y axis of the coordinate system, which means the radiating elements are oriented along the x axis. The patterns do not demonstrate perfectly linear polarization, but do show a clear co-polarized field. This is much more obvious for frequencies at and beyond 4GHz.

In addition to the radiation patterns the maximum gain was analyzed with respect to frequency. This is shown in Figure 16 and represents the maximum total gain taken at broadside. The maximum gain shows a steady increase from 2GHz to 8GHz and then remains level up to 18GHz. The gain variation is expected and quite frequently the case for such and ultra wide bandwidth, especially for log-periodic structures.

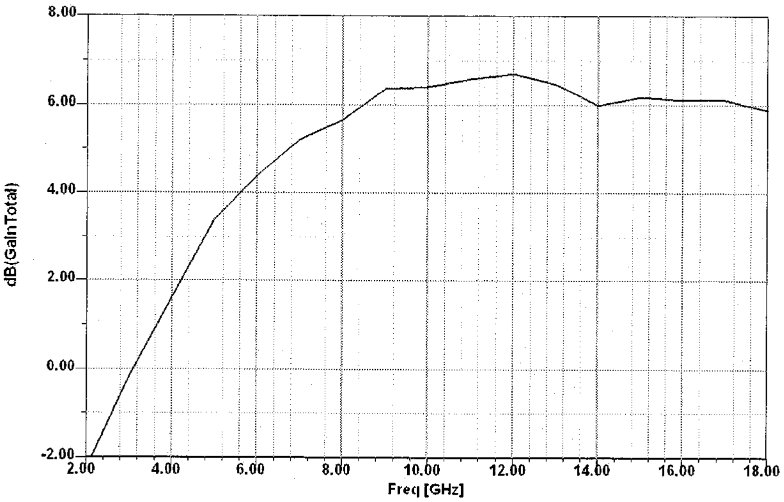

Figure 16. Maximum Gain vs. Frequency for Two Arm Sinuous Antenna

3.6 Four Arm Sinuous Antenna Simulated Results

The essence behind the performance of the sinuous antenna can be observed by the four arm self-complimentary design. The four arm sinuous antenna is composed of two two-arm structures rotated 90° from each other. Unlike the two-arm structure, the four arms act as two orthogonally polarized antennas, which can produce dual circular polarization. Dual circular polarization is achieved when orthogonal arm pairs are excited ±90° out of phase with respect to each other. This will soon be discussed in more detail.

The same design principles that were used for the two arm structure were applied for the four arm structure. The optimizations and improvements, as well as the materials, and even the general knowledge acquired for the previous design were all incorporated into enhancing the four arm structure's performance.

3.6.1 Four-Arm Structure in Free Space

The four arm free space sinuous antenna is shown in Figure 17.

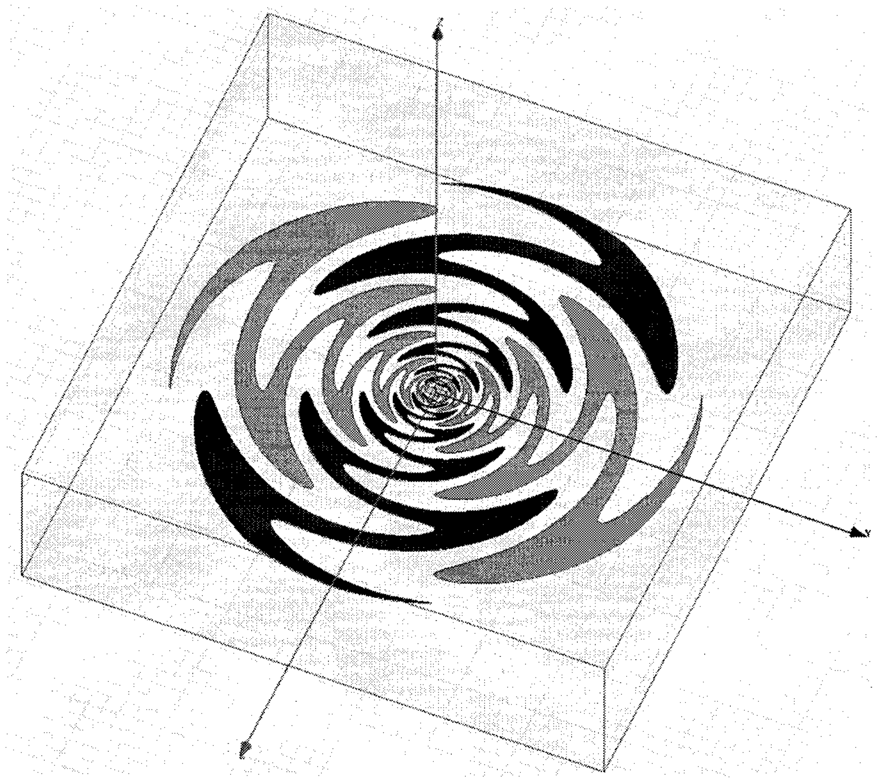

Figure 17. Four Arm Sinuous Antenna

3.6.1.1 Radiation Patterns

To monitor the performance of the antenna over the 2-18GHz band, the phi directed electric fields (E_ϕ) and the theta directed electric fields (E_θ) were plotted for the same cut planes as before. These fields are shown in Figure 18.

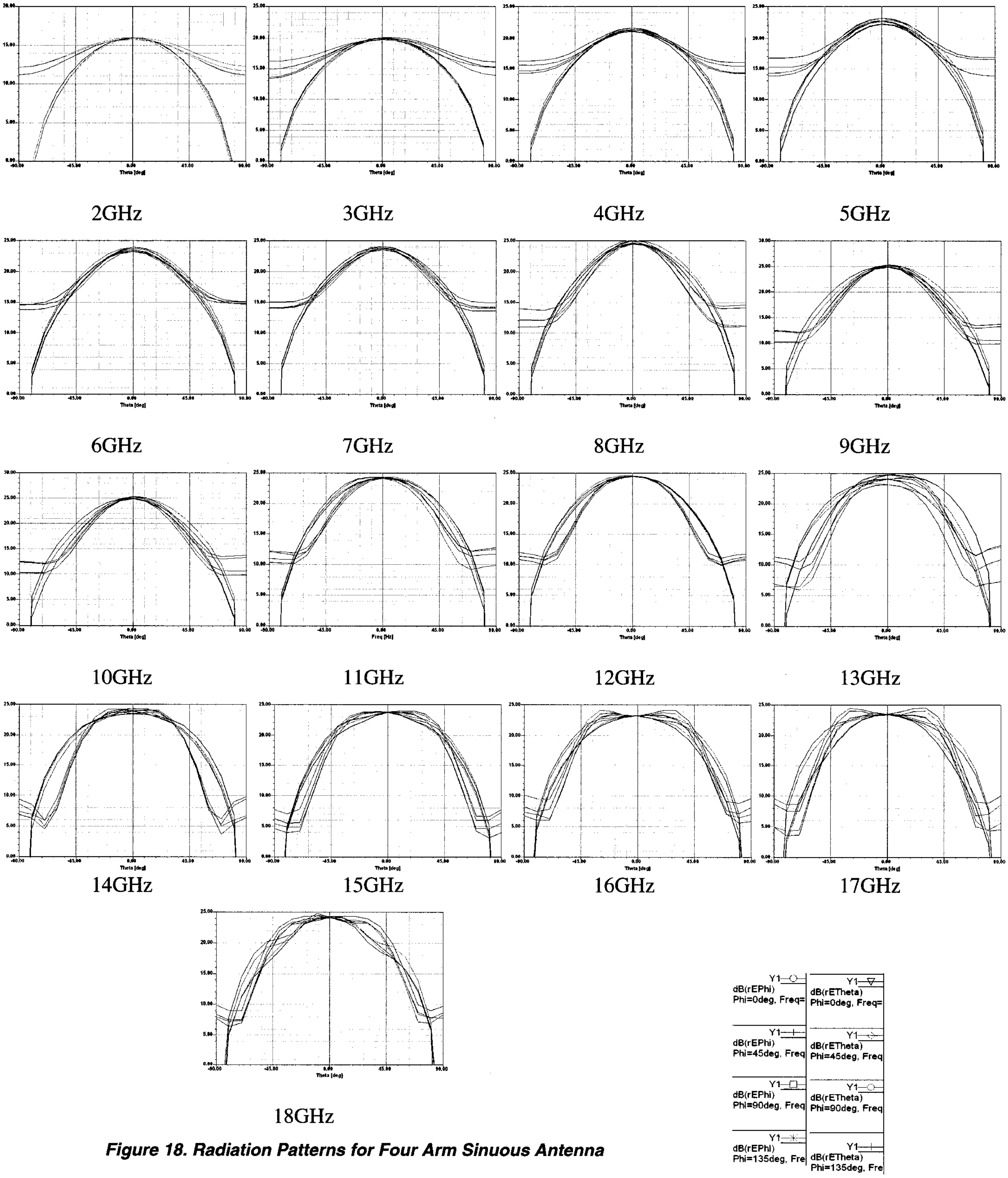
2GHz 3GHz 4GHz 5GHz

6GHz 7GHz 8GHz 9GHz

10GHz 11GHz 12GHz 13GHz

14GHz 15GHz 16GHz 17GHz

18GHz

Figure 18. Radiation Patterns for Four Arm Sinuous Antenna

The overlaps in the field patterns, especially near and around broadside, represent good symmetry in three-dimensional space. This is true because a pattern cut was taken at every 45° up to 135° in the azimuth. Regardless of the frequency, the patterns are all similar to each other, clearly illustrating the frequency independence of this antenna. In addition to bandwidth, the beamwidth is also shown to be quite wide which is in accordance with spiral antennas.

The beamwidth of the antenna pattern for the active region is inversely proportional to the radius of the active region.

$$BW \propto \frac{1}{\alpha_p + \delta} \tag{16}$$

Thus α could be adjusted so that the self-complimentary condition defined by δ remains satisfied. Conversely, one can achieve frequency dependent beamwidth using a quasi-log periodic design by simply letting τ and α be a function of the cell number, *p*. This would allow the beamwidth to be controlled and varied with frequency.

3.6.1.2 Circular Polarization

The axial ratio for circular polarization can be shown equal to:

$$AR = \frac{a}{b} = 1 \quad or \quad 0dB \tag{17}$$

Figure 19 shows the axial ratio (AR) and the total electric field (E_{TOT}) plots for both ϕ=0° and ϕ=90° respectively for 2-18GHz.

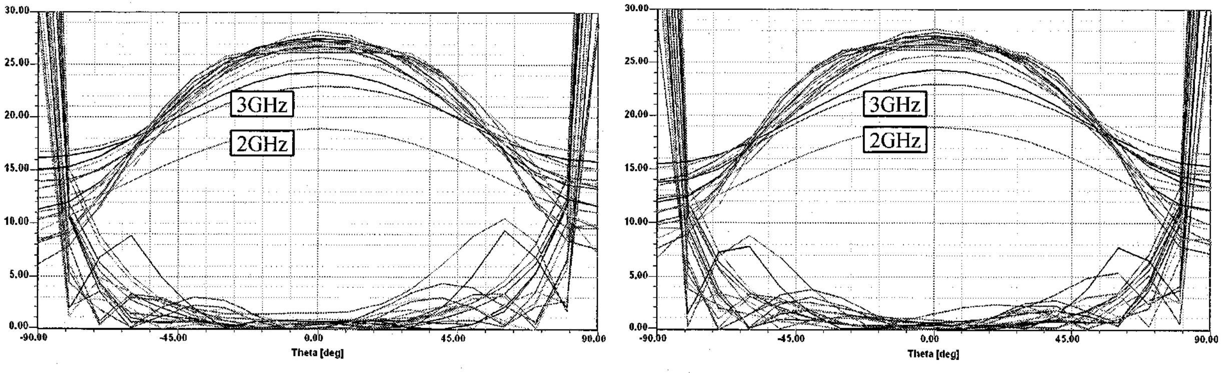

a) ϕ=0° b) ϕ=90°

Figure 19. Axial Ratio (AR) and Total Electric Fields (E^{TOT})

The two cuts show almost identical behaviour, both showing a minimum axial ratio and a maximum total electric field at θ=0°. For almost all frequencies, the axial ratio is below 1dB for an approximate beamwidth of 45°. The 3dB AR beamwidth is over 100° for all but two frequencies. As θ approaches ±90°, the axial ratio increases from close to 0db (circular) to ∞ (linear). Such theoretical results have been achieved with perfectly fed input signals supplied by the electromagnetic simulator. In practice, the sinuous antenna has never achieved such a wide AR beamwidth due to the imperfections of the feed network which degrade the overall symmetry.

As in any real system, perfect circular polarization cannot be achieved [26] so we will re-define the AR based on the following equation:

$$AR = \begin{cases} \dfrac{|E_{RHCP}| + |E_{LHCP}|}{|E_{RHCP}| - |E_{LHCP}|} & \text{Predominantly RHCP elliptical wave} \\ \\ \dfrac{|E_{RHCP}| + |E_{LHCP}|}{|E_{LHCP}| - |E_{RHCP}|} & \text{Predominantly LHCP elliptical wave} \end{cases} \tag{18}$$

The above equation can help interpret the axial ratio plotted in Figure 19 as an elliptically polarized antenna with predominantly right-hand or left-hand circular polarization [26]. The sense of polarization cannot be determined from the AR plots, but can be determined from the phase difference in the orthogonal electric fields E_θ and E_ϕ.

$$\begin{aligned} \angle E_\phi - \angle E_\theta &= -90 \quad RHCP \\ \angle E_\phi - \angle E_\theta &= +90 \quad LHCP \end{aligned} \tag{19}$$

Assuming a wave traveling in the +z direction

The phase of the electric fields depends on how the feed of the antenna was fed at the ports. Figure 20 exemplifies the two types of configurations.

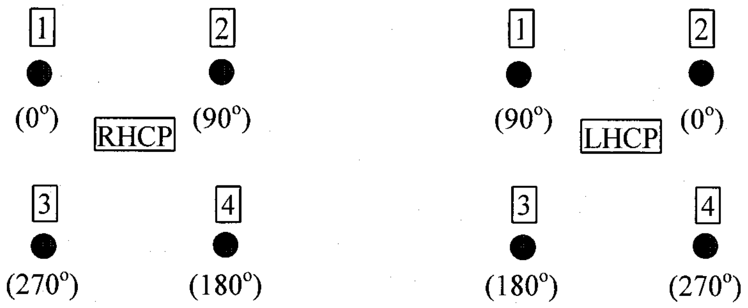

a) RHCP b) LHCP

Figure 20. Phase Feed

Biasing feed points 1 and 4 with a -90° shift creates a RHCP antenna and a +90° shift creates a LHCP antenna. In the present case, there is a -90° shift which indicates RHCP. However, since this is a dual polarized antenna, the opposite sense can also be achieved by simply switching the phase from -90° to +90° (with respect to a common reference). Dual polarization implies that both senses of polarization should be simultaneously achieved. This can be implemented using a 90° Hybrid which will apply both +90° and -90° phase shifting. In the absence of the 90° Hybrid, dual linear polarization will be attained provided there are two input signals.

3.6.1.3 Gain

The gain of the sinuous antenna is said to be similar to that of a spiral antenna [4][9]. The gain patterns of the two principle planes for each frequency are shown in Figure 21.

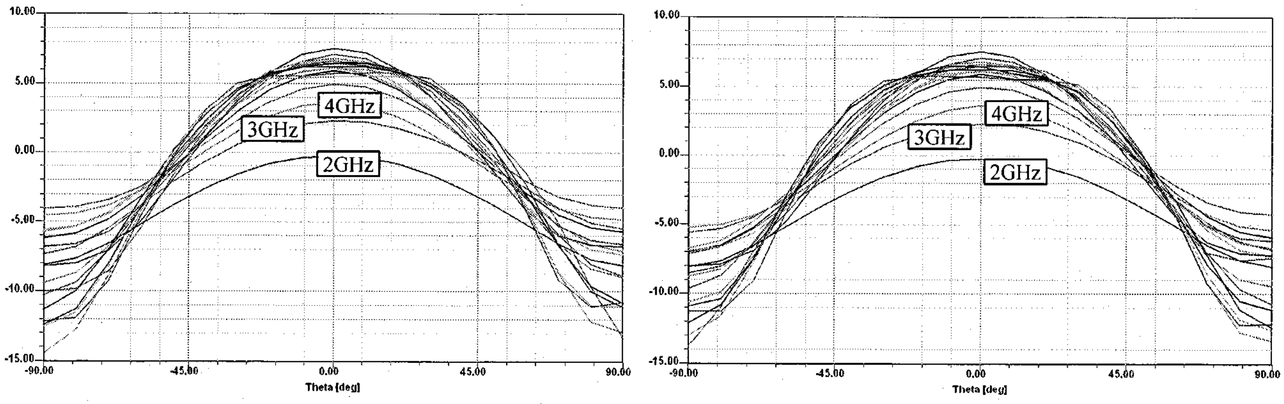

a) $\phi=0^\circ$ b) $\phi=90^\circ$

Figure 21. Gain Pattern for Four Arm Sinuous Antenna

Much like the total electric field plots shown earlier, the frequency plots for the gain overlap each other fairly well accept for the same four lower frequencies (2,3,4,5 GHz). To get a better idea of how the maximum total gain, taken at broadside, varies with frequency, Figure 22 portrays the maximum gain frequency response.

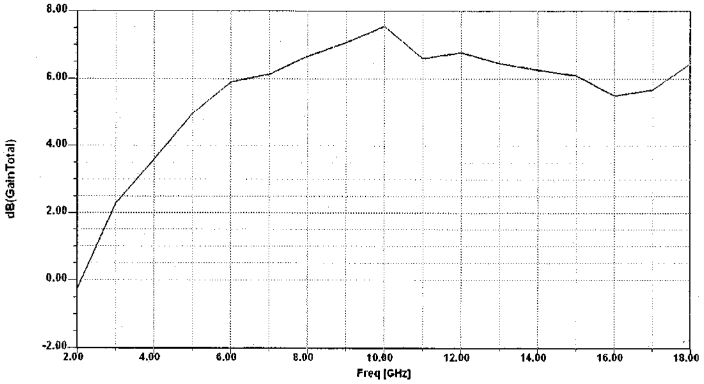

Figure 22. Maximum Gain vs. Frequency for Four Arm Sinuous Antenna

The general behaviour of this maximum gain plot is comparable with the performance of four arm spiral antennas [31].

3.6.1.4 Current Distribution and 3D Patterns

In a previous section we discussed how the sinuous curve establishes a circumferential current distribution which solves the E and H pattern uniformity problem. The product of the radius and the circumferential arm width defined by the angle $2(\alpha_p+\delta)$ can determine the active region of radiation for the sinuous antenna at any given frequency based on the following expression:

$$2r\left(\alpha_p+\delta\right)\approx\frac{\lambda}{2} \tag{20}$$

Figure 23 illustrates this property by showing the current distribution and radiation patterns for 2, 10, and 18 GHz respectively.

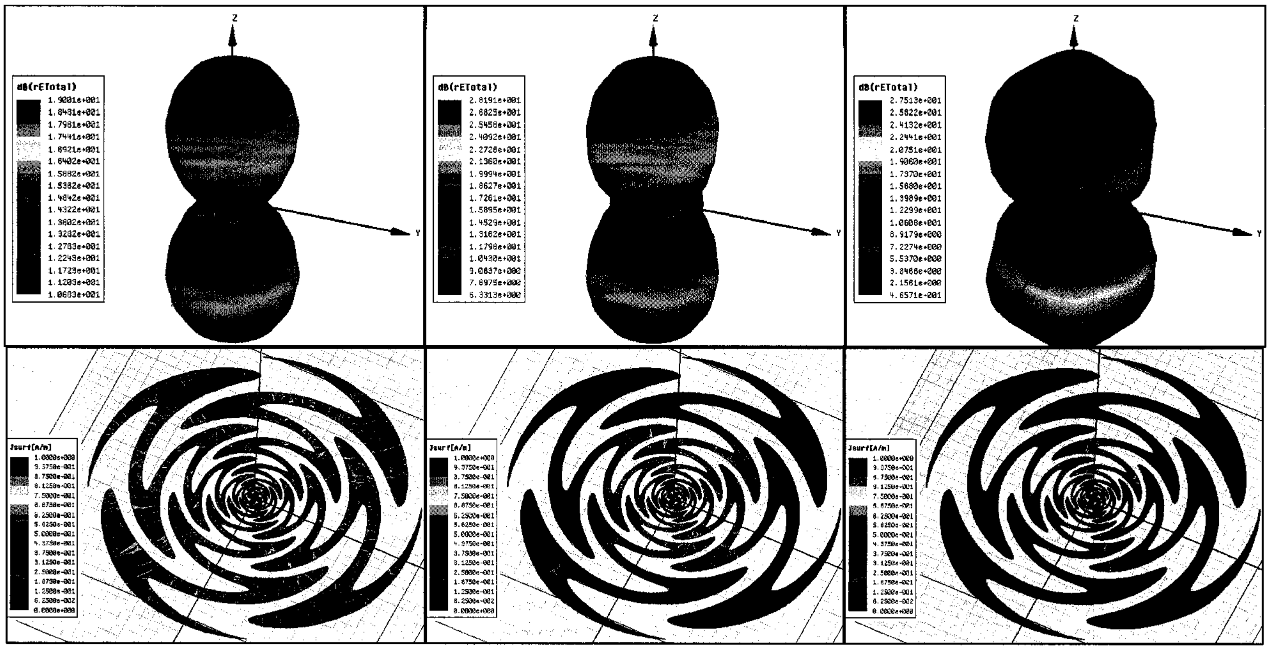

2GHz 10GHz 18GHz

Figure 23. Radiation Patterns and Current Distribution for the Four Arm Sinuous Antenna

The current distribution at the outer edges of the sinuous antenna is more intense for 2GHz than for 10 and 18GHz. This is as expected because the active region of radiation for 2GHz was specifically designed at this outer radius. Similarly, the inner radius was designed for the upper frequency. This is the reason the current distribution becomes more concentrated in the centre as one increases frequency. The three dimensional radiation patterns at each frequency are symmetrical bidirectional broadside patterns.

3.6.2 Four-Arm Structure with Substrate

The four arm sinuous antenna previously analyzed exhibited good radiation patterns, gain, beamwidth, and polarization over the entire 2-18GHz band. In order to manufacture this antenna, a substrate needs to be included. The substrate types and thicknesses considered in the design are summarized in Table 1.

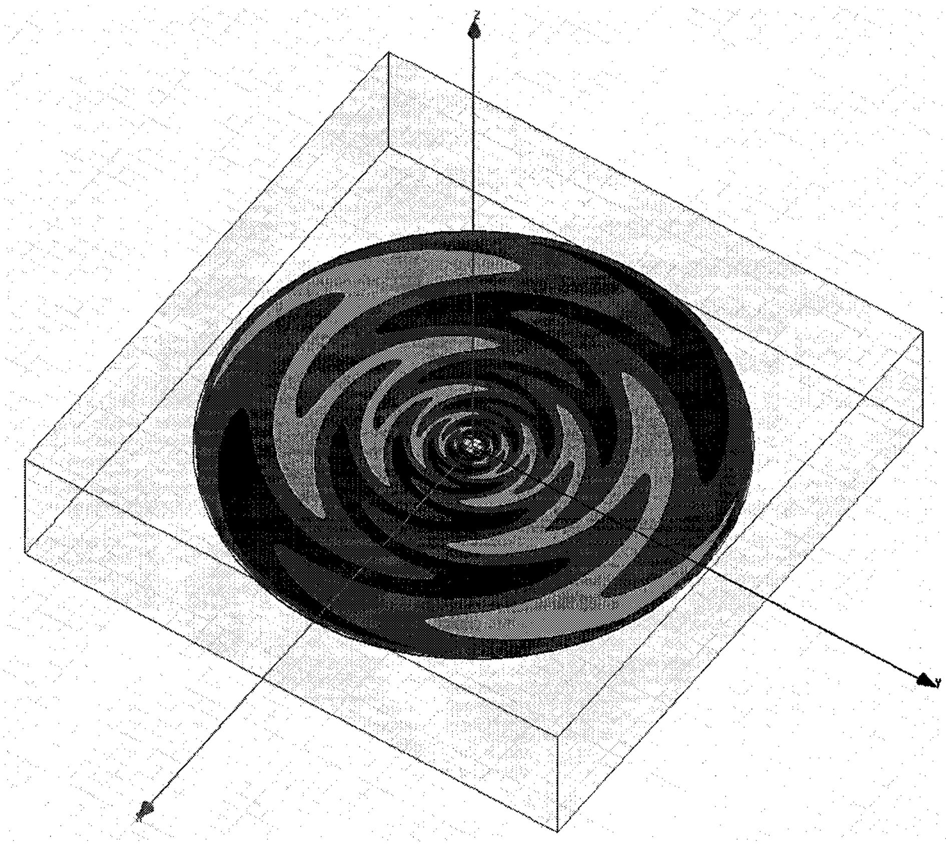

Figure 24. Four Arm Sinuous Antenna with Included 10-mil Substrate

Table 1. *Substrate Parameters*

Substrate Type	**Relative Permittivity (ε_r)**	**Relative Permeability (μ_r)**	**Loss Tangent**	**Thickness (d)**
Duroid 5880	2.2	1	0.0009	10 mil
Duroid 5880	2.2	1	0.0009	20 mil
Duroid 5880	2.2	1	0.0009	31 mil
Rogers RO4003	3.38	1	0.0027	8 mil
Rogers RO4003	3.38	1	0.0027	20 mil

In many cases, the various types of substrates and thicknesses lowered the AR beamwidth of the sinuous antenna when compared with that of the free space solution. However, the 10-mil Duroid substrate caused the least amount of degradation in performance. This structure resembled the free space solution the closest and was chosen to be presented in more detail.

The radiation patterns of the electric field components, E_ϕ and E_θ, are plotted at $\phi=0^\circ$, $\phi=90^\circ$, $\phi=45^\circ$, and $\phi=135^\circ$ for every frequency and shown in Figure 25. Figure 26 shows the total electric field and AR plots at $\phi=0^\circ$ and $\phi=90^\circ$. Figure 27 illustrates the gain performance for the same principle cuts and Figure 28 demonstrates how the maximum total gain varies with frequency.

The AR still clearly shows circular polarization. At $\phi=0^\circ$, the 3dB beamwidth is virtually unchanged from before and is close to 90° for all but one frequency (13GHz).

The gain patterns and maximum gain frequency response plots also show good resemblance with the freespace performance. There is once again a constant increase in gain from the lower frequency up to a maximum at 10GHz. As mentioned earlier, the gain dependence with frequency is expected to vary yet it still obeys the frequency independence principle of the antenna. This is true because of the frequency independent input impedance of the antenna, which ensures a good match and minimum reflection over the entire band.

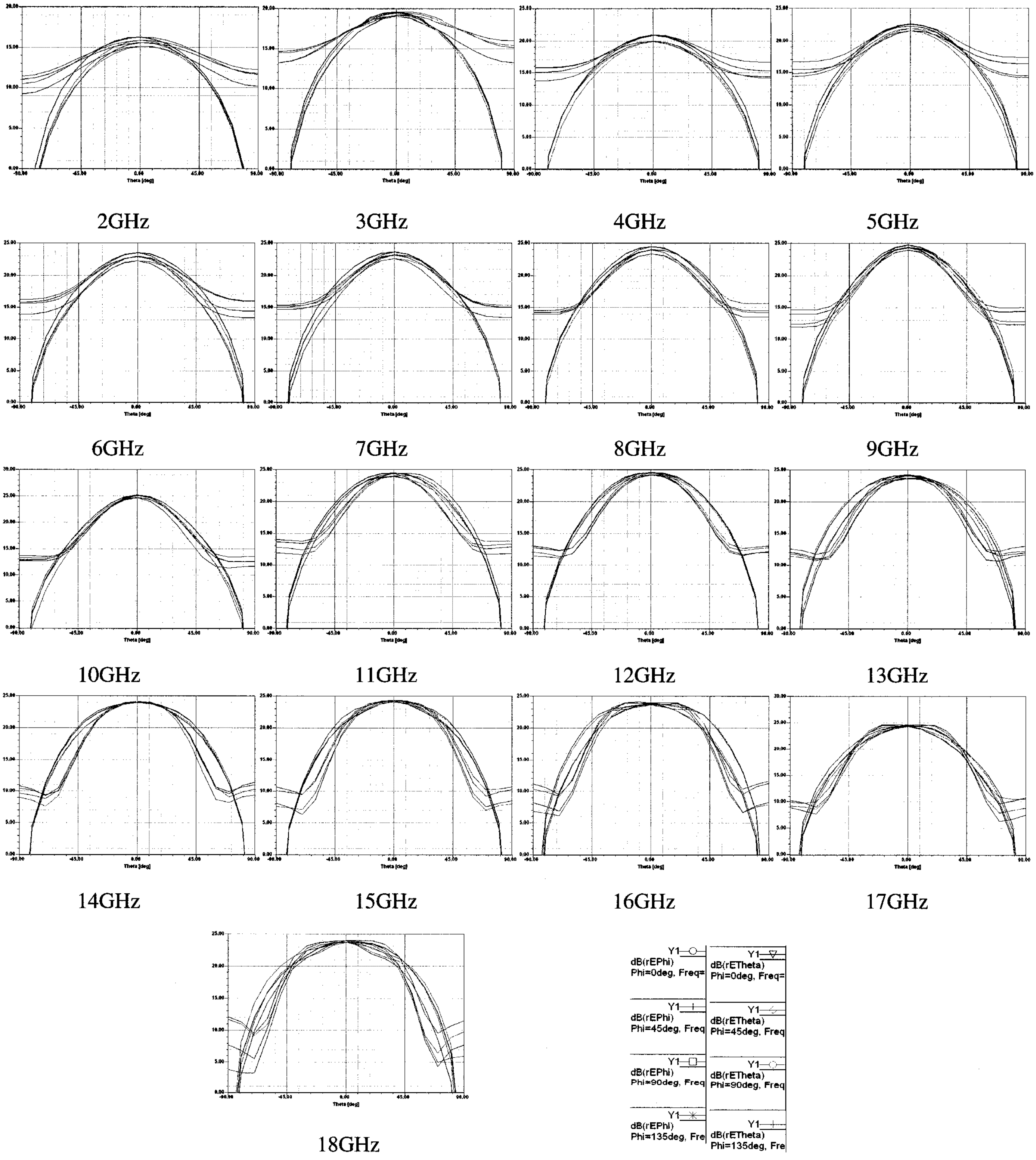
2GHz 3GHz 4GHz 5GHz

6GHz 7GHz 8GHz 9GHz

10GHz 11GHz 12GHz 13GHz

14GHz 15GHz 16GHz 17GHz

18GHz

Figure 25. Radiation Patterns for Four Arm Sinuous Antenna with 10-mil Substrate

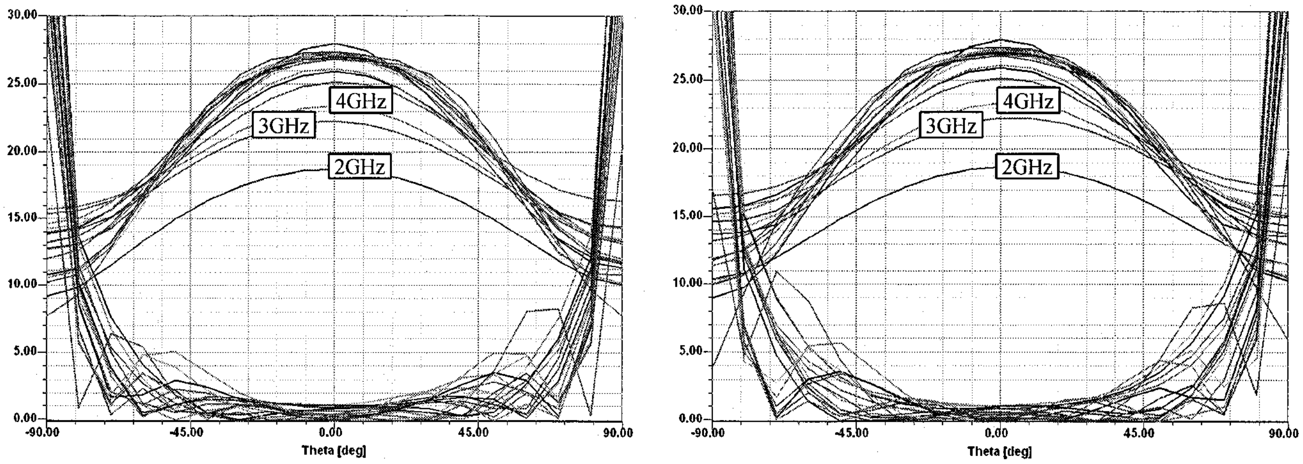

a) ϕ=0°

b) ϕ=90°

Figure 26. Axial Ratio (AR) and Total Electric Fields (E^{TOT})

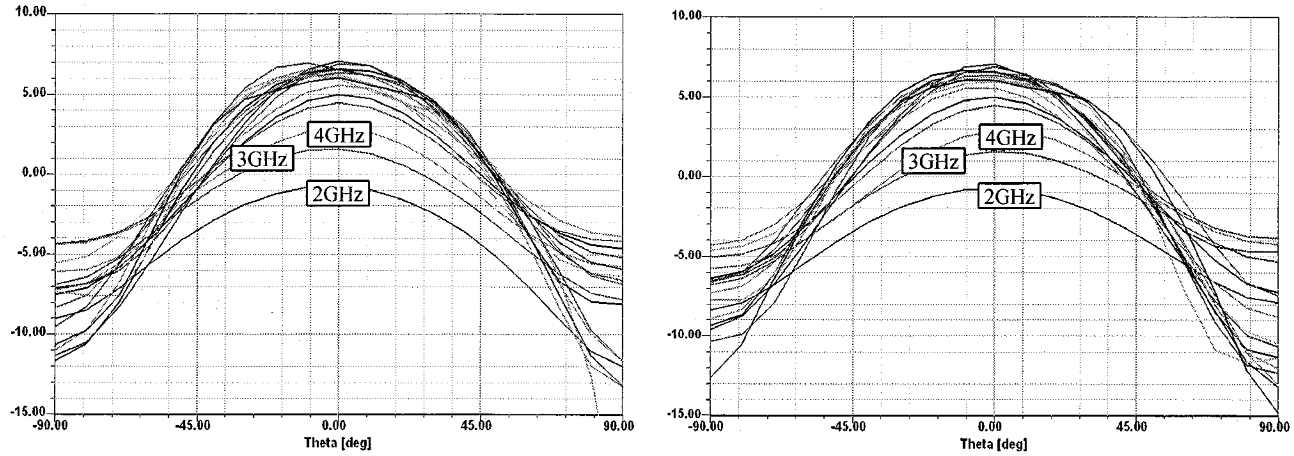

a) ϕ=0°

b) ϕ=90°

Figure 27. Gain Pattern for Four Arm Sinuous Antenna with 10-mil Substrate

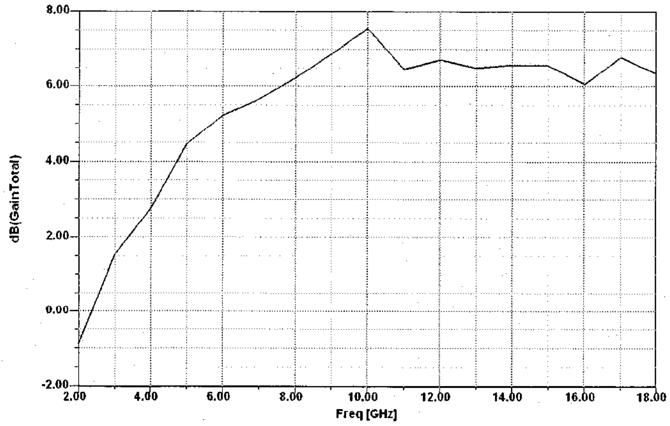

Figure 28. Maximum Gain vs. Frequency for the Sinuous Antenna with 10-mil Substrate

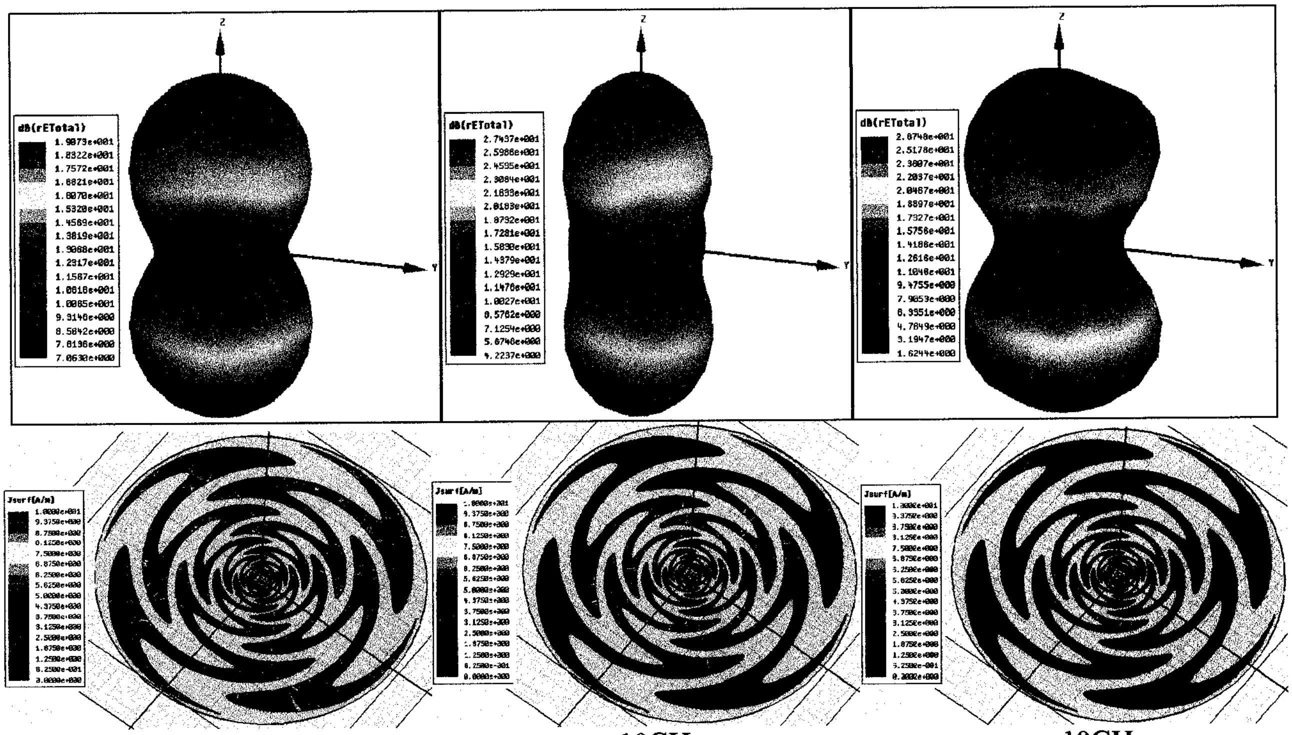

2GHz 10GHz 18GHz

Figure 29. Radiation Patterns and Current Distribution for the Sinuous Antenna

3.6.3 Four-Arm Cavity-Backed Structure

All the antennas discussed thus far have been bidirectional antennas, having both forward and backward radiation patterns. In most applications, unidirectional patterns are desired and can be achieved using a conical configuration such as that shown in Figure 30 [4].

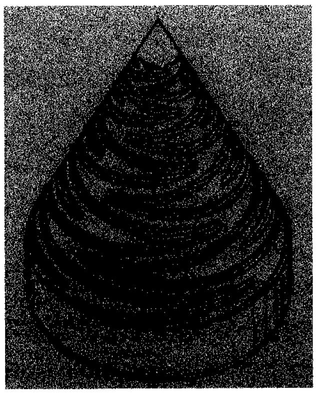

Figure 30. Six Arm Conical Sinuous Antenna

However, the conical configuration is not planar, and it adds size and complexity to the design. An alternate solution is to place a cavity on the backside of the substrate and fill it with absorbing material. If designed properly, the cavity should house the feed network, and the absorbing material should absorb all the backwards radiation. An example of the cavity backed sinuous antenna is shown in Figure 31.

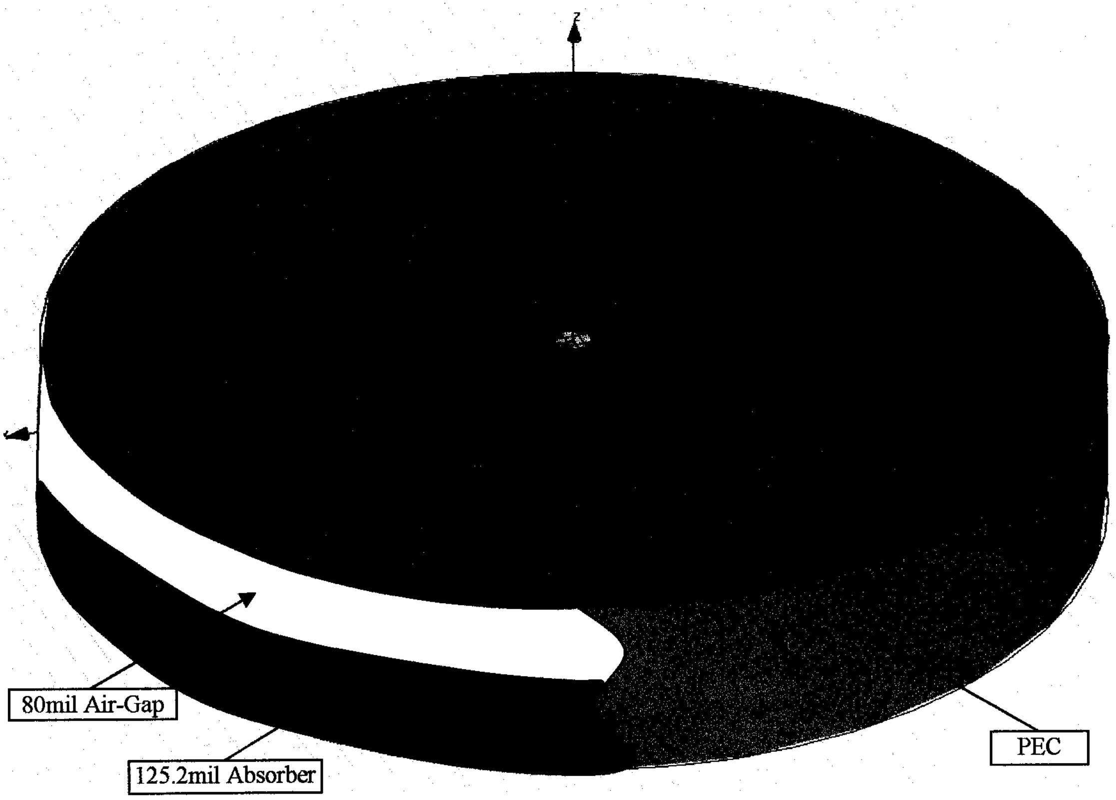

Figure 31. Cavity Backed Four Arm Sinuous Antenna

The cavity assembly is still early in its design phase mainly due to two problems that were encountered. Primarily, the depth of the cavity and the solving of the fields within the absorber require hardware resources beyond the capabilities of a 32bit machine. This problem was never resolved and only resulted in the analysis of non-converged results. The secondary problem is due to the fact that the detailed parameters on wideband absorbers are proprietary which makes it very difficult to properly model. The solution to both these problems can only be solved after manufacturing the structure and analysing the physical measurements. Thus, this thesis can only present the preliminary investigations of the depth of the metallic cavity and the type and thickness of the absorbing material. The material used for the simulations was chosen to be GDSS for which only the very basic properties were obtained. The properties for 2 and 18 GHz are summarized in Table 2 as provided by Cumming Microwaves. A tapered function was assumed as an estimated model to fill in the missing information.

***Table 2.** GDSS Absorbing Material Properties*

Frequency (GHz)	ε'	ε"	μ'	μ"	Dielectric Loss Tangent	Magnetic Loss Tangent	Absorber Thickness
2	15.35	-0.45	3.6	-1.48	0.0293	0.0411	125.2 mil
18	8.86	-0.4	1.05	-0.9	0.0451	0.8571	125.2 mil

Some observations noted while designing the cavity was the need for a spacer between the substrate and the absorbing material. Others have used honeycomb material to ease this transition [7]. Currently, an 80 mil air gap was used because it is the absolute maximum the computer could solve with some degree of confidence.

The three dimensional radiation patterns illustrate good unidirectional broadside patterns. The back lobes are no longer present due to the absorption within the GDSS. In some cases, it may be necessary to use multiple layers of GDSS for better absorption.

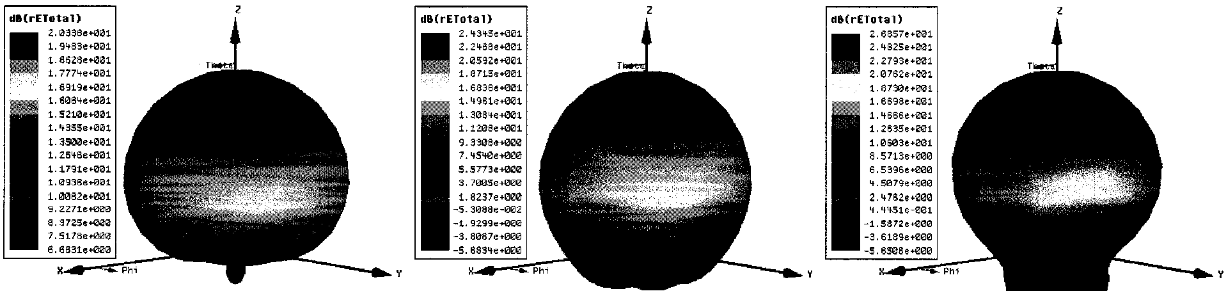

2GHz 10GHz 18GHz

Figure 32. Unidirectionnel Radiation Patterns

Maintaining a one layer GDSS absorber isolated with an 80mil air-gap, the AR 3dB beamwidth was not affected as shown for both principle cuts in Figure 33 (with an exception of the 6GHz frequency plot).

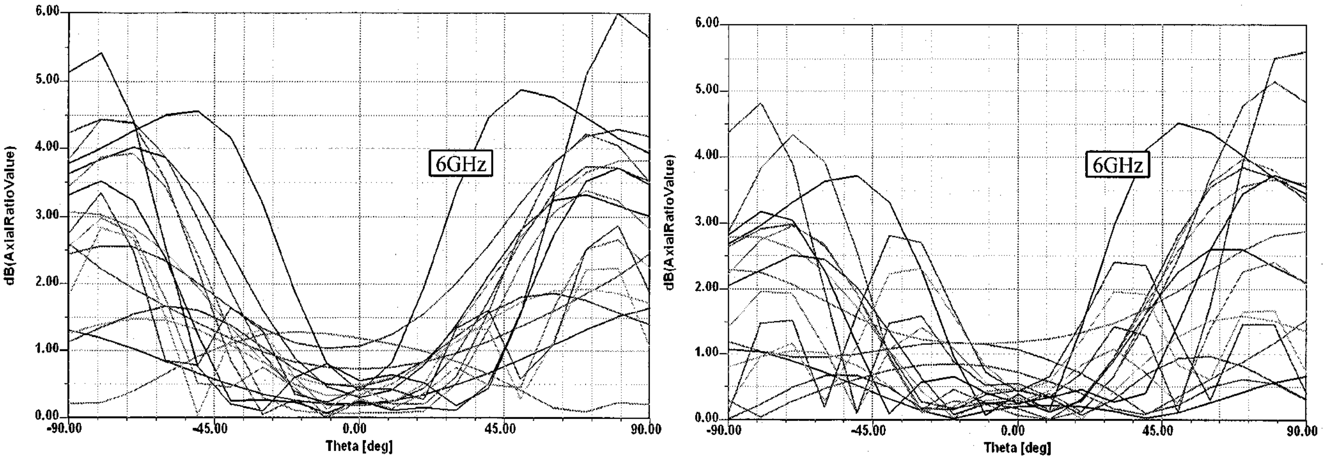

a) ϕ=0°

b) ϕ=90°

Figure 33. Axial Ratio (AR) for the Four Arm Cavity Backed Sinuous Antenna

Unfortunately, the maximum gain of the antenna was degraded and contained severe fluctuations for frequencies 2-8GHz. The fluctuations present at the lower frequency band of the gain response are due to the resonance within the cavity at 3 and 6 GHz. But it is believed that such resonance can be shifted down and out of the desired frequency band by increasing the depth of the cavity but this should increase higher order modes. However, with a larger cavity, more absorbing layers can be placed to cancel out the resonances. This could not be done due to the memory restrictions proportional to the physical size of the design. The maximum gain frequency response is shown in Figure 34.

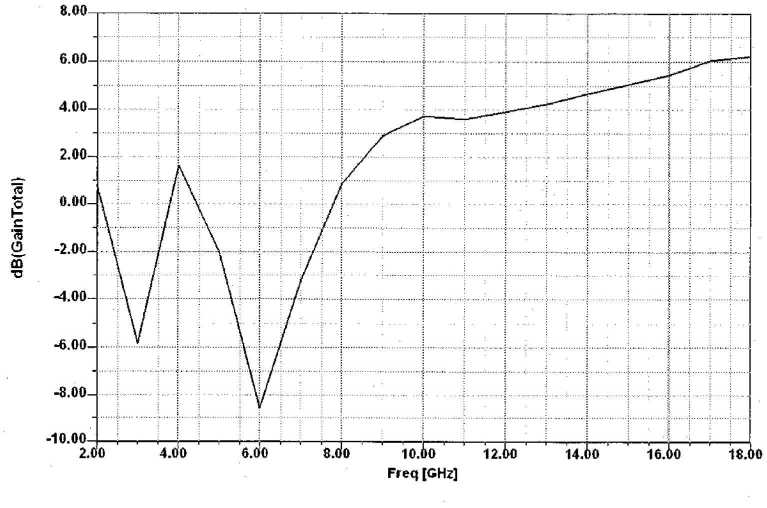

Figure 34. Maximum Gain vs. Frequency for Four Arm Cavity Backed Sinuous Antenna

The efficiency of such a method is reduced to at best 50%. This is because half the power is lost due to the absorber. It would be ideal to put a reflector instead of the absorber, but this cannot be implemented due to the wide bandwidth of operation. A sinuous antenna array, in the conventional sense cannot be implemented either.

3.6.4 Arm-Pairs Printed on both Sides of the Substrate

All sinuous antennas discussed thus far require somewhat complicated techniques when attaching the feed network to the antenna. This issue will be further discussed later in the thesis. Here, an alternate form of the four arm structure is presented to help simplify this feed complexity issue. By etching each antenna arm-pair on either side of the substrate, the two feeds will no longer cross each other on a level plane. Figure 35 depicts this configuration.

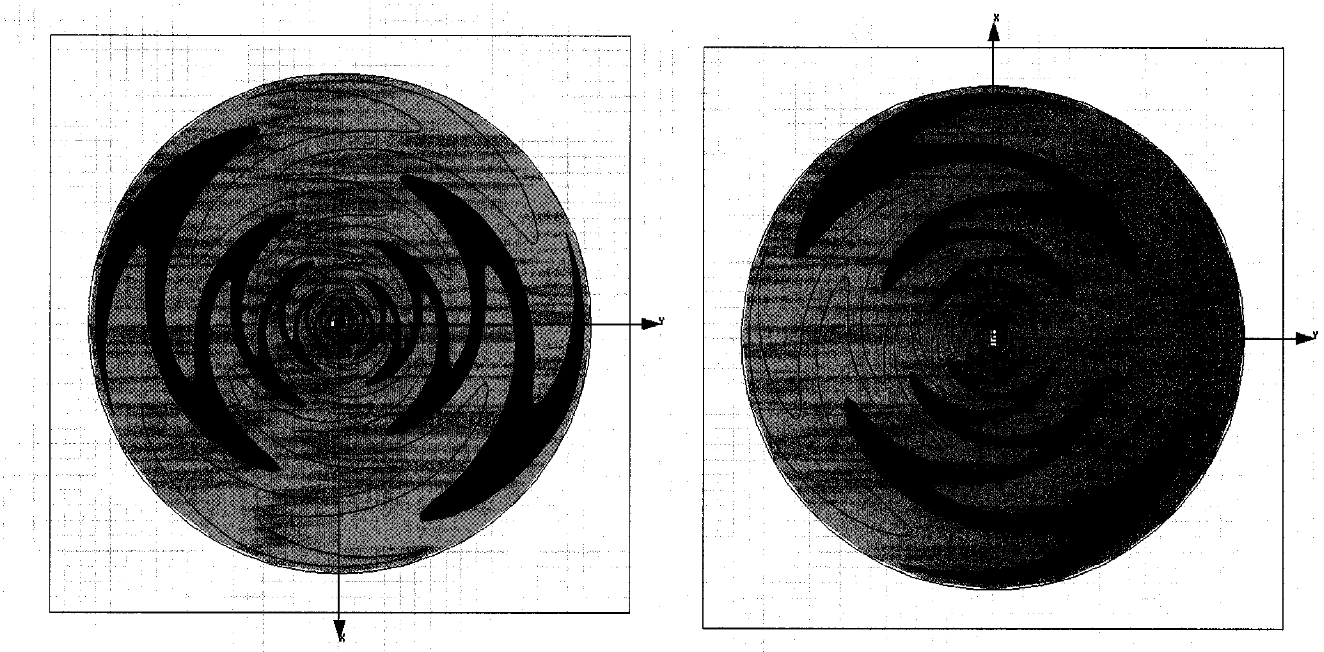

a) Top View b) Bottom View

Figure 35. Sinuous Antenna with each Arm-Pair Printed on Different Sides of Substrate

In general, the performance of the antenna had minor degradation due to the lack of symmetry between the bottom structure and the top structure. The substrate introduces a minor loss (reflection) for the bottom structure. The AR beamwidth of the antenna is reduced for the upper frequencies to about 50°, which is a bit more than half the beamwidth of the previous design which was greater than 90°.

The maximum gain versus frequency is plotted in Figure 36 to illustrate that the gain was not affected by this modification. The main difference, when compared with the previous designs is noticed at the upper frequency range where there is a slight increase in gain variation.

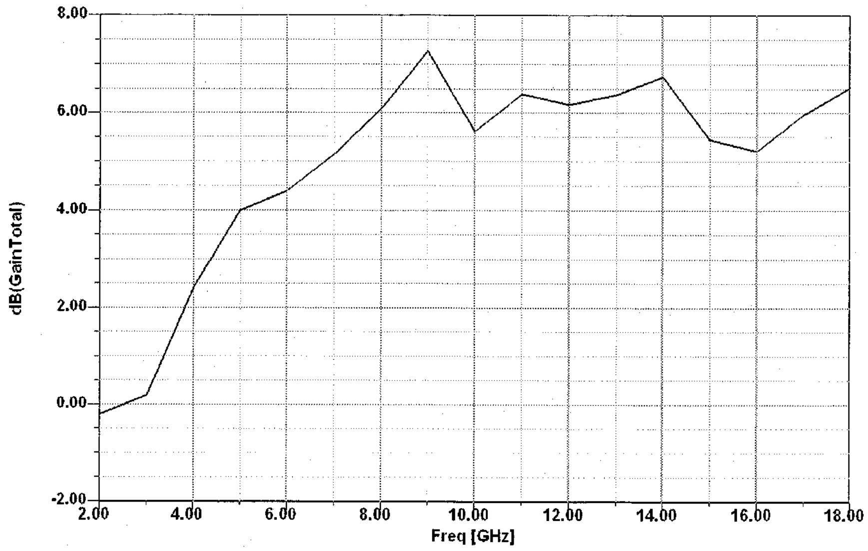

Figure 36. Maximum Gain vs. Frequency for Dual Side Printed Four Arm Sinuous Antenna

3.7 Linear and Circular Polarization Feed Networks

Thus far, we have designed and analyzed the four arm sinuous antennas without much focus on the practical aspect of how to excite the structure. Depending on the desired polarization, different feed networks should be implemented.

A simple two arm sinuous antenna is all that is required for linear polarization. However, the four arm structure is necessary to achieve dual linear polarization. A block diagram in Figure 37a represents the feed network required to achieve dual linear polarization. This requires two feed ports connected to two baluns. Similarly a block diagram in Figure 37b represents the feed network required for dual circular polarization, involving two baluns and a 90° Hybrid.

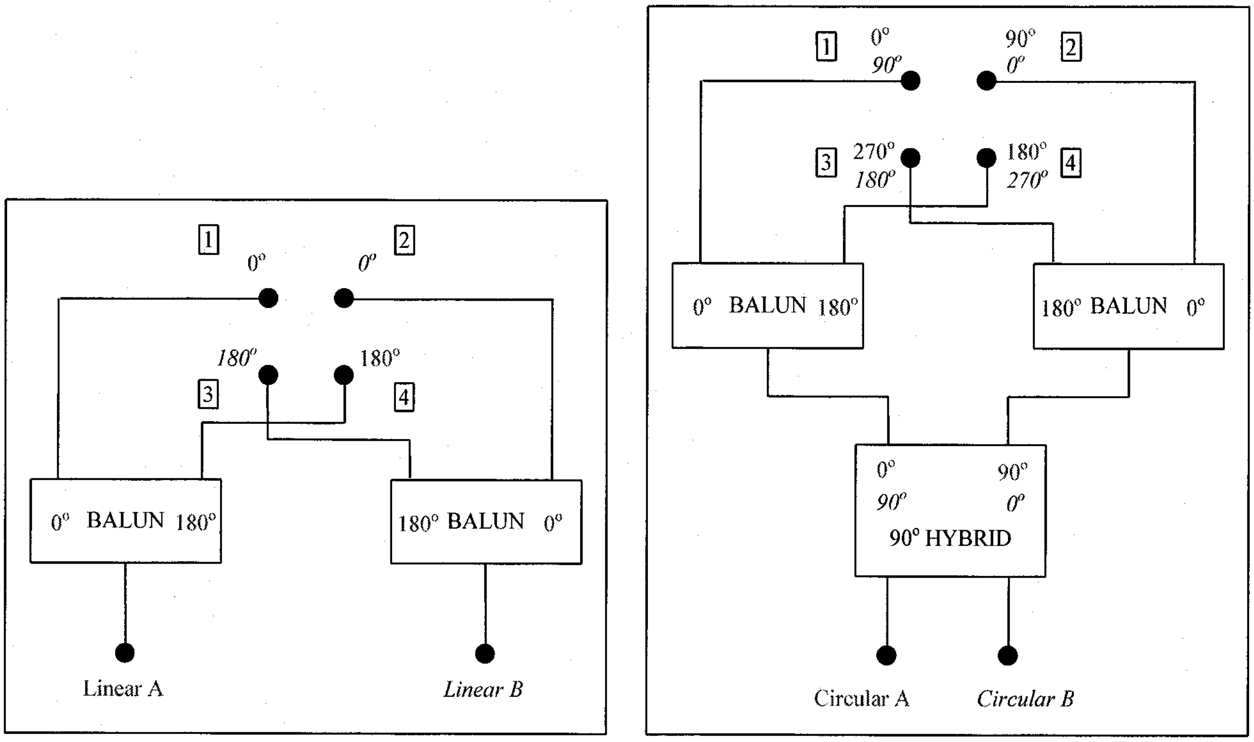

a) Linear Polarization

b) Circular Polarization

Figure 37. Feed Network for the Four Arm Sinuous Antenna

The baluns and the 90° Hybrid are most definitely the bandwidth-limiting factors for such a wideband antenna rather than the antenna itself. To achieve linear polarization, all that is required is a single balun and a single arm-pair. However, the unpopularity of the sinuous antenna arises from its complexity which only occurs with the feed integration of circular, dual linear, and dual circular polarization. This is directly due to the crossing of the balun's paired strips at the input of the antenna. It is of course physically impossible to do this without sacrificing the symmetry of the antenna through some kind of alteration. We will next perform a detailed design of two different wideband balun structures.

4. Balun Design

Research towards ultra wideband balun designs began when Marchand first introduced transmission line conversion [34] and Duncan and Minerva developed the tapered balun concept [35]. A wideband balun is the key component to feed wideband devices such as antennas and mixers. A balun is a transformer designed to transform an unbalanced mode (UBM) into a balanced mode (BM). In general the input, usually the unbalanced-line port (UBLP) will resemble microstrip and the output balanced-line port (BLP) will consist of two equally structured conductors having currents with the same magnitudes and opposite phase. For the purpose of this thesis we are interested in wideband baluns which, in addition to UBM to BM conversion, will perform an impedance transformation to achieve impedance matching over a wide range of frequency. This is desired because the self-complementary sinuous antenna has a frequency independent input impedance. There are different methods and techniques that can achieve this transition which are chosen based on various requirements such as:

- Desired bandwidth
- Size limitations
- Planar or non-planar requirements

This thesis discusses the designs and simulation results of two different balun structures that are all based on the same basic principles. Each balun consists of three sections. The first section is the UBLP, which connects to an unbalanced transmission line such as a microstrip line. The middle section is the mode transformation section, which transforms an electromagnetic wave from the UBM to the BM. The last section is the BLP which connects to a balanced line, such as coplanar or non-coplanar paired strips. The characteristic impedance of the unbalanced line is 50 ohms while the characteristic impedance of the balanced line is not fixed. The design goal is to shape the dimensions of the middle and last sections to allow the wave to smoothly convert from UBM to BM while maintaining a good return loss. The output impedance will be adjusted to match the impedance of the corresponding antenna input.

The design procedure for each balun consisted of two stages. During the first stage, a matched load, which can be very easily applied in HFSS is connected at the BLP. This allows a single port device to be simulated. Once a good return loss (|S11| dB) is obtained for the single port device, the second phase can be carried out, in which a two-port device is studied. The two-port device is constructed by two identical baluns attached back-to-back. The BLP of the second balun is connected to the BLP of the first one so that the incident wave comes from the first balun's UBLP, converts from UBM to BM and enters into the second balun, then converts from BM to UBM, which finally outputs at the UBLP of the second balun. The back-to-back configuration has certain practical advantages as it allows for easy measurement due to the 50Ω microstrip ports as well as an accurate method to measure the insertion loss. The insertion loss of the single balun structure is exactly half the insertion loss of the double structure.

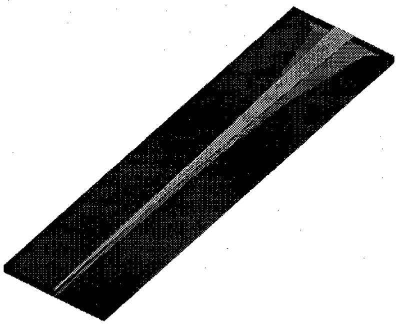

Figure 38. Conventional UWB Balun

4.1 Generating the Geometry

Much like the sinuous antenna, the first two baluns were constructed using the help of the automated code that was developed. This automated approach allows for quick optimizations and greatly reduces total time required.

4.2 Simulation Techniques

The optimization stage of the simulated results is generally the most tedious, time consuming, and hardware intensive part of the design. In many cases, many simulations were required to obtain the final product. For this reason some effort went into developing various techniques for quicker and less-memory intensive solutions.

4.2.1 Symmetry of Structure

Taking advantage of HFSS's symmetry boundary conditions we were able to automatically reduce any symmetrical problem in half through the use of a magnetic wall (H-Wall). In the case of both baluns discussed in this thesis, we used an H-Wall along the long axis of the balun. This would indicate that the number of finite elements could be reduced to half, which can reduce the FEM matrix size up to a quarter.

Depending on the nature of the structure one may choose to use an electric wall (E-Wall) for a similar purpose. The type of symmetry wall chosen would depend on how the fields are oriented within the structure. In either case an impedance multiplier must be specified to adjust for the other half of the structure. In the case of an E-Wall the impedance multiplier must be set to 2, while for an H-Wall, the impedance multiplier must be set to 0.5 [15].

4.2.2 Symmetry between Two Ports

We mentioned earlier that part of the design process is to setup a back-to-back mirrored balun for simulation. This would automatically create a two-port structure used to determine the baluns' insertion loss. Unfortunately this technique would double the size of the structure and the number of finite elements. In addition to an increase in size, we will now have a two-port problem to solve, which increases the simulation time and memory required considerably.

The solution is again in the use of E and H walls, but in an entirely different manner. This strategy reduces the back-to-back mirrored structure to a single structure, automatically eliminating half the size, and reduces the problem to a single-port problem. The idea is to simulate two smaller one-port devices, first using an E-Wall and then an H-Wall. Each wall will be placed perpendicular to the axis of the balun at the precise midpoint of the back-to-back structure.

From the two simulations we determine the return loss of the particular model (S_{11}^E *and* S_{11}^H), which can be used to obtain the overall desired parameters based on the following relations:

$$S_{11} = S_{22} = \frac{S_{11}^E + S_{11}^H}{2} \qquad S_{21} = S_{12} = \frac{S_{11}^H - S_{11}^E}{2} \tag{21}$$

It is important to note that in this case the impedance multiplier is set to 1 because we are not impinging on the cross sectional symmetry of the device.

4.3 Paired-Strip Calculation

In addition to the actual design of the balun, the input and output port widths of the upper and lower conductors must be carefully calculated. The input 50Ω port will resemble microstrip because the bottom conductor width should be significantly larger then that of the top conductor. Thus calculating the width of this conductor is quite trivial and can be done using any microstrip calculator. However, on the balanced output side, we no longer have microstrip but rather paired strips. The paired strips have equal upper and lower conductor widths. To calculate these widths for a desired impedance we can employ image theory.

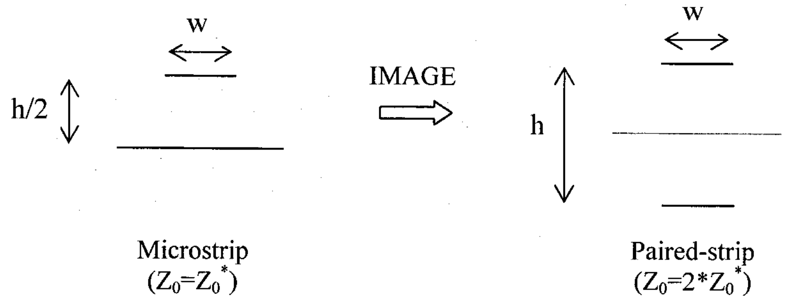

Figure 39. Image Theory Representation: Microstrip to Paired Strip

The above figure suggests how to calculate the width of a desired characteristic impedance of a paired strip line. Using a basic microstrip calculator, one only needs to specify half the desired impedance and half the actual distance between the two strips to obtain the correct width.

4.4 Tapered Balun Structure: Microstrip to Paired-Strip

The tapered balun design is a traditional wideband design consisting of a tapered transmission line that slowly converts in cross-sectional characteristics from an unbalanced line with one characteristic impedance to a balanced two-conductor line with another characteristic impedance

[35]. The balun's overall length will depend on the particular cross sectional transition of the line as well as the lowest desired frequency. The lower the frequency, the longer the balun becomes. Figure 40 shows a conventional tapered balun structure with an exponentially tapered bottom conductor and a linearly tapered top conductor. Further research would benefit on the study of different tapering methods [37], but for the scope of this project the current configuration is sufficient.

4.4.1 Simulated Results for the Tapered Balun

After numerous optimizations we were able to minimize the return loss of the balun while keeping the insertion loss at a minimum. The return loss of the balun can be further improved by having a smoother transition from one end to the other of the balun. Unfortunately this increases the balun's length and degrades the insertion loss. Thus we were able to find a compromise that satisfied all our requirements.

The final product was given a substrate thickness of 31mil and a relative permittivity (ε_r) of 2.2. The balun, shown in Figure 40, has a length of approximately half a wavelength at the lowest frequency. The width of the line at the balanced port is currently at 12 mils, but can continually be tapered down until the desired impedance is achieved for the specific antenna. Throughout this thesis we have been focusing on minimizing size as one of the key design specifications which should suggest a large permittivity value. However, due to the high input impedance of the antenna, large permittivity values would yield non-realizable width size of the baluns required for a good match. For example, if a 230Ω impedance is desired, the paired strip width for a relative permittivity of 2.2 and 3.8 would be 10mil and 5.5mil respectively based on a 31mil thickness. This was calculated based on the image theory principle shown earlier. It should now be clear as to the reason why a relatively low permittivity was chosen even though it would increase the length of the balun.

Both printed conductors have a gradual change in width of the line needed to support BM at the output. Figure 41a shows the return loss of the single port device of the balun. It can be observed that the return loss is below 20 dB for 2 to 3 GHz and 4.25 to 18 GHz. For the back-to-back baluns, the maximum insertion loss determined by the simulation is 2 dB (Figure 41b). This indicates that the maximum insertion loss of the single balun is 1 dB. It should be noted that the S11 and S22 for the back-to-back balun simulations are shown only to be used as a comparison with the measured results. They are not to be associated with return losses of the single balun.

All simulations were done using finite conductivity of copper for the conductors and appropriate loss-tangent values for the 5880Duroid board.

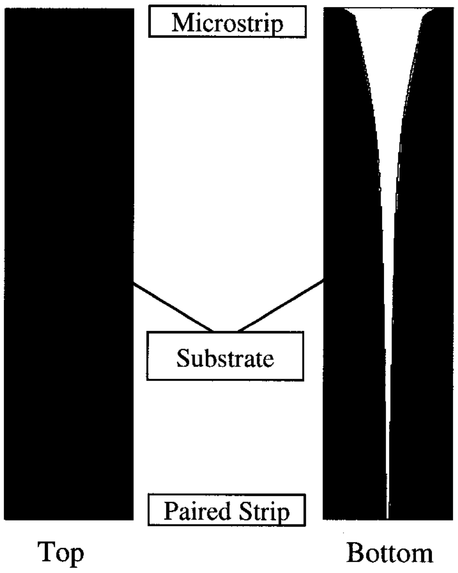

Figure 40. Tapered Balun

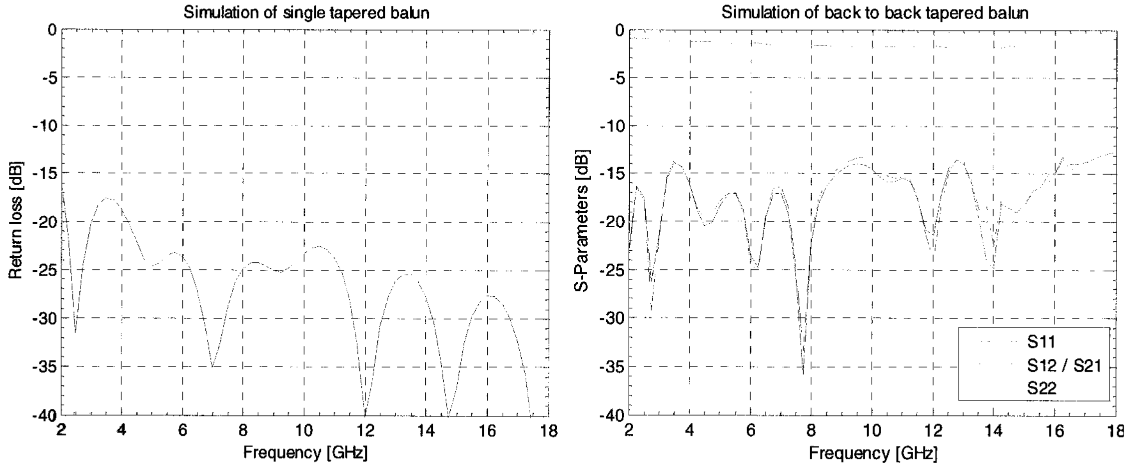

a) Return Loss with Matched Load at the BLP b) S-Parameters of Two Back-to-Back Baluns

Figure 41. Tapered Balun Simulated Results

4.4.2 Measured Results for the Tapered Balun

Both, the tapered single balun and back-to-back balun structures were manufactured. The single balun was manufactured to be used in a two arm sinuous antenna system construction, while the back-to-back balun was created for the sole purpose of measurement and comparison to the simulated back-to-back results. The constructed back-to-back structures are shown in Figure 42 with two different types of connectors. This was done as part of a study towards the effect of the connector on the device under test (DUT). The standard SMA connector with rounded centre conductor and the SMA connector with flat centre conductor were both compared. The measured insertion loss of the device with both connectors is shown in Figure 44.

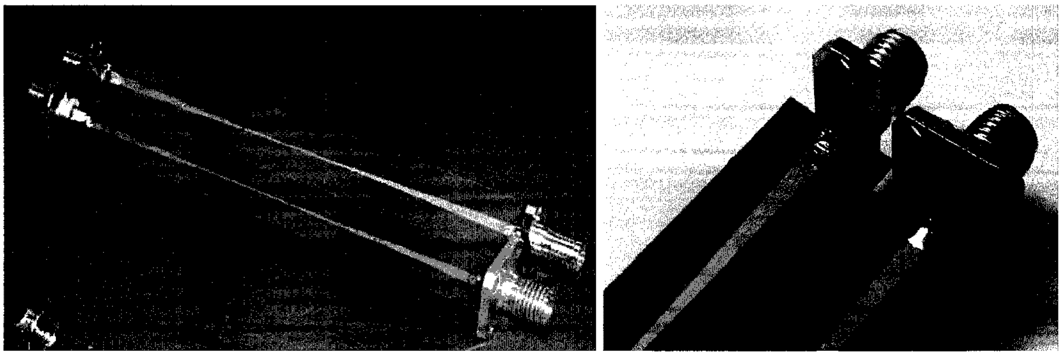

Figure 42. Tapered Back-to-Back Baluns

Figure 43. Round and Flat Centre Conductors

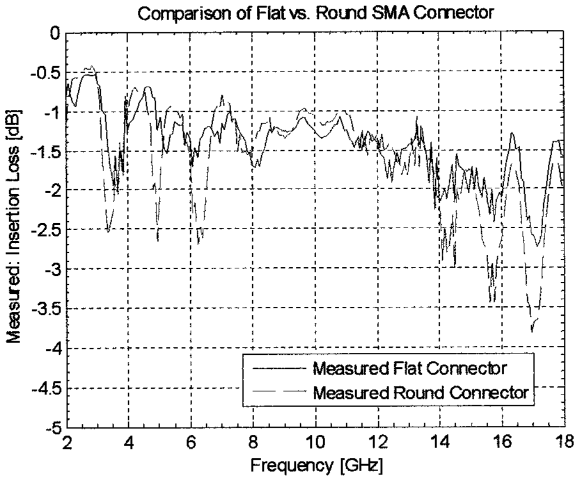

Figure 44. Comparison of SMA Connectors of the Back-to-Back Structure

As one should expect, the balun with the flat connectors yields better results (flatter response) and thus was used to compare with the simulated results which are displayed in Figure 45. In both cases the results are in good agreement with each other. However, the simulated insertion loss of the device is slightly, but notably, worse than the actual measurements at the lower frequencies. This is believed to be a direct result of the fixed, frequency independent, loss tangent available for the 5880 Duroid, which was utilized by the simulator. It is unreasonable to expect that the loss tangent would be constant throughout a band as wide as 2 to 18GHz and thus should be considered an approximation at best. The increase in loss with frequency is in accordance to what one would expect since losses are always more significant at the higher frequencies.

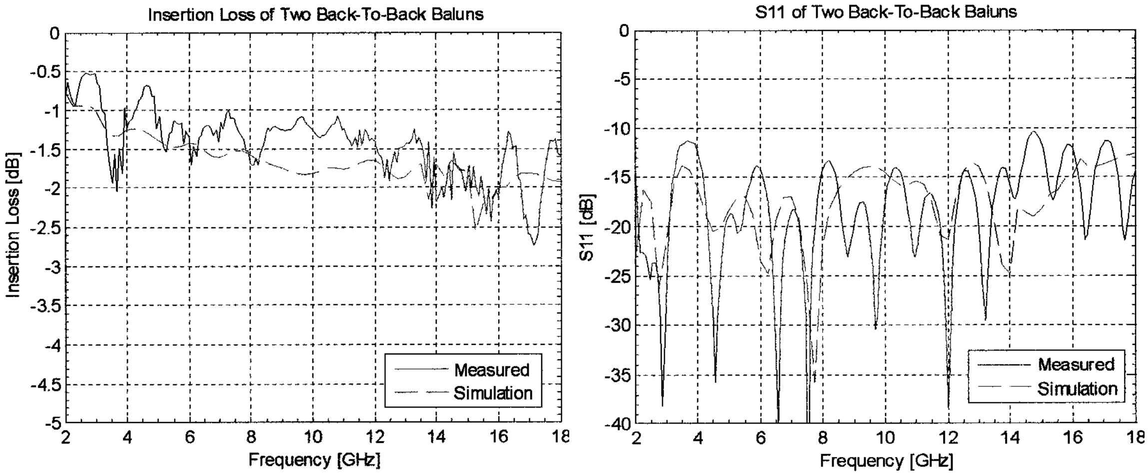

a) Insertion Loss of Two Back-to-Back Baluns b) S11 of Two Back-to-Back Baluns

Figure 45. Simulation vs. Measurement of Tapered Balun

4.5 Slotted-Ground Balun Structure: Microstrip to Paired-Strip

The second balun design is a novel structure developed to reduce the total length and complexity of the first design. This new structure eliminates the tapered functions used for UBM to BM conversion of both the upper and lower conductors. The new approach involves slots in the lower conductor which results in a microstrip to paired strip conversion. This design was constructed using an empirical approach which primarily depends on the length and width of the slots in the ground conductor. These slots are the cause of the mode transformation as evident from the geometry of the structure. The benefit is that the mode transformation section of this balun is significantly shorter than the taper of the first balun, which depended on the lowest frequency. It is important to keep in mind that a balun's only task is mode transformation, but can be used for impedance transformation as a secondary objective. The first balun's long length is due to the mode transformation (approximately half a wavelength at 2GHz) as well as the impedance transformation used for matching. However, the second balun relies on a discontinuity rather than a taper for the mode transformation section which yields a balun that is approximately 45% shorter. The balun illustrated in Figure 46 has a 50Ω impedance microstrip port and a 50Ω impedance paired strip port. It will be referred to as a 1:1 slotted-ground balun.

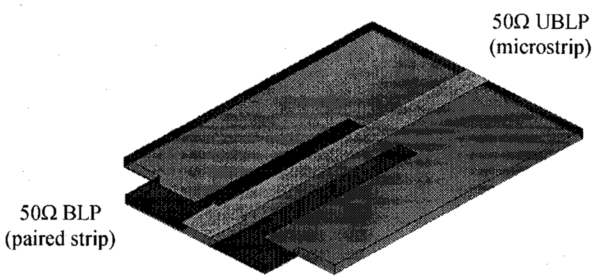

Figure 46. 1:1 Slotted-Ground Balun

Before we illustrate the simulated insertion and return loss, we can verify that this structure is indeed performing the mode transformation by monitoring the current distribution. Plots for 2, 10, and 18 GHz are presented to illustrate equal current magnitudes and 180° phase differential at the BLP of the balun.

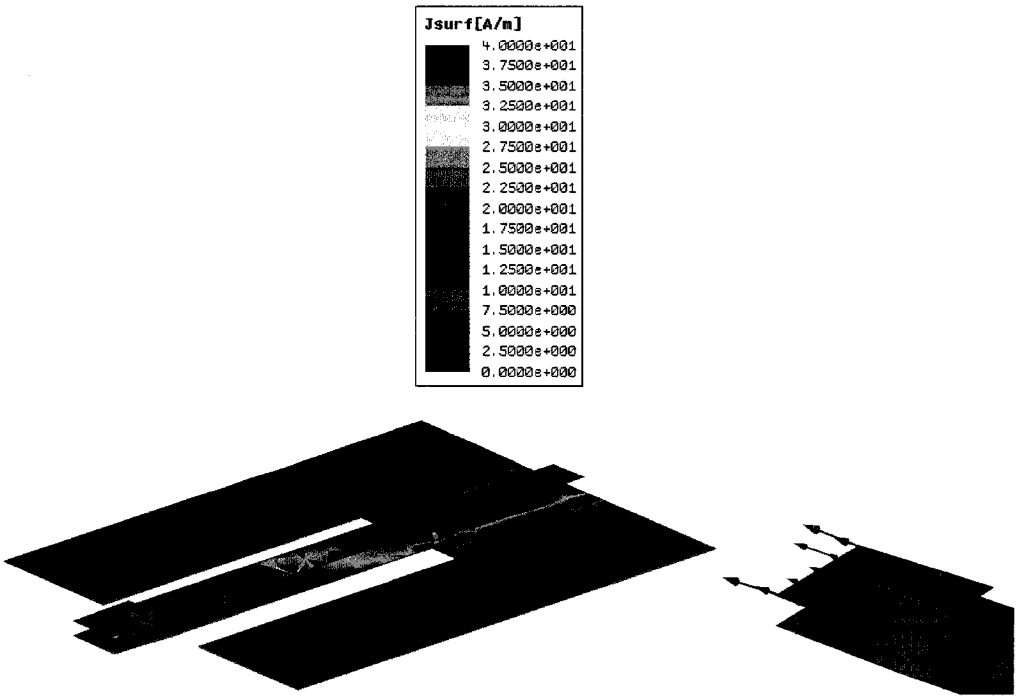

2 GHz

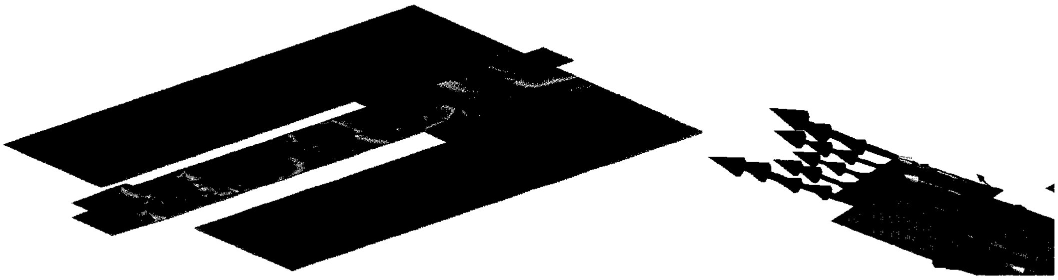

10GHz

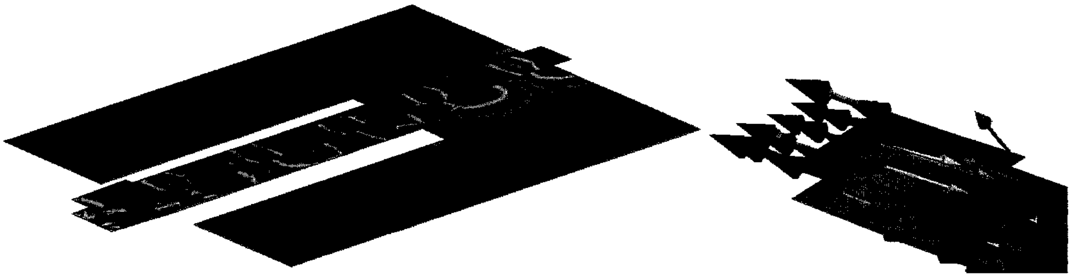

18GHz

Figure 47. Current Distribution for 2, 10, and 18 GHz

4.5.1 Simulated Results for the Slotted-Ground Balun

The performance of this 1:1 balun is illustrated in Figure 48.

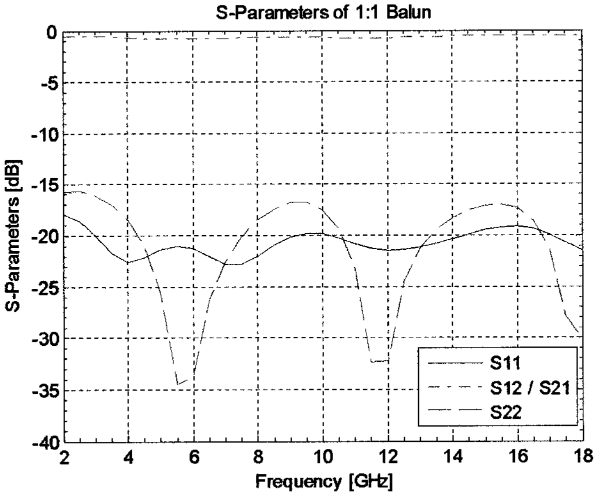

Figure 48. 1:1 Slotted-Ground Balun Simulated Results

The return loss of the structure shows a very nice flat response averaging less then 20dB. Since, for the purpose of this project, we are not interested in a 1:1 impedance transformer, the balun's width at the BLP is linearly tapered until the desired output impedance is obtained. There is a significant difference between such a taper and the taper used in the first balun discussed. In this case the taper begins with the paired strip lines, which means both the bottom and upper conductor's cross-sectional width are identical from the start to the end of the taper. Figure 49 illustrates this design. The length of this balun depends on the impedance transformation rather than the mode transformation. The 50 ohm microstrip line is etched on a 31 mil substrate. The relative permittivity of the substrate is once again 2.2. There are two slots etched in the ground plane of length 680 mils used for the mode transformation. The length and the width of these slots were found empirically and then optimized using a fully automated C++ code which used the HFSS macro language that called the Matlab provided data. To obtain a good return loss at the lower frequency band, the impedance transformation section of the balun shown in Figure 49 needs to be long enough to allow a smooth transition. When a 2 inch taper was utilized, very good return loss was obtained for the single port device as illustrated in Figure 50. However, one of the main design goals for this project was to maintain a minimum size (length) and thus such a design was unacceptable. After redesigning the impedance transformation section for a minimum frequency of about 5GHz (simply shortening the taper length) so that this balun would be approximately the same length as the conventional tapered balun previously discussed the return loss was sacrificed. Figure 51a shows that the return loss of this balun is better than 15 dB from 5 to 18 GHz, when a matched load is connected at the BLP. It is unfortunate that after such a taper the balun was not able to yield better than 10dB return loss for frequencies below 3.5GHz. The insertion loss of the back-to-back structure also illustrates a problematic region below 3.5GHz.

In comparison with the conventional tapered balun, the slotted-ground balun is more simple, less dependent on tolerances, and has a significantly reduced mode transformation section length. As the requirement of the impedance transformation ratio increases, the advantage of this slotted-ground balun decreases. Nevertheless, for the present design, this sacrificed (shortened) slotted-ground balun was constructed, but should only be utilized for frequencies above 3.5GHz.

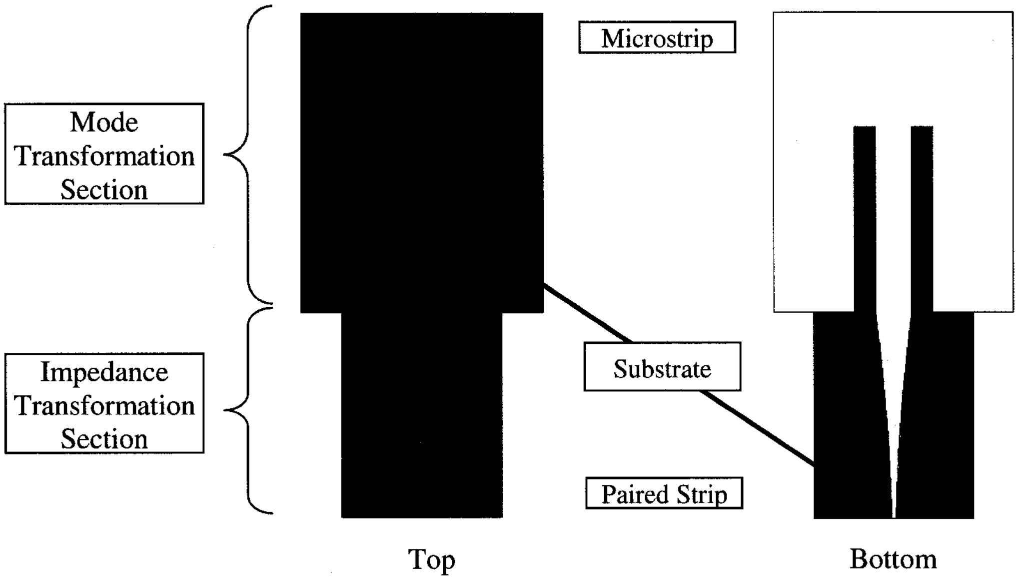

Figure 49. Microstrip to Paired Strip Slotted-Ground Balun

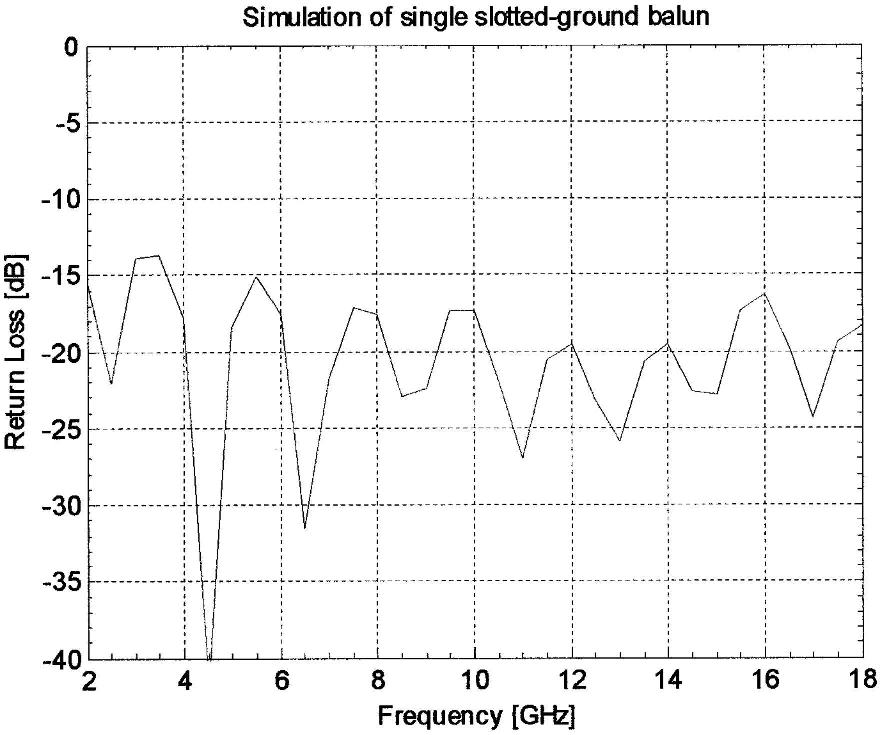

Figure 50. Slotted-Ground Balun Simulated Results

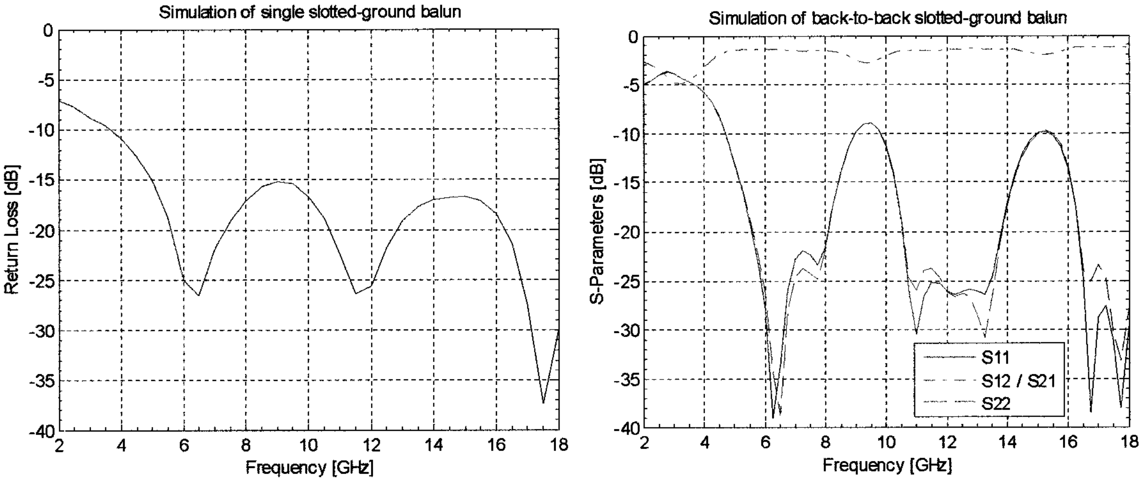

a) Return Loss with Matched Load at the BLP b) S-Parameters of Two Back-to-Back Baluns

Figure 51. Slotted-Ground Shortened Balun Simulated Results

4.5.2 Measured Results for the Slotted-Ground Balun

Once again, both the single and back-to-back baluns were manufactured. The single balun was manufactured for testing the performance of a two arm sinuous antenna system and the back-to-back structure for measurement and comparison with the simulated results. Unlike the first balun structure, this balun was measured only with the rounded and slightly inferior connectors. The measured results are illustrated in Figure 53.

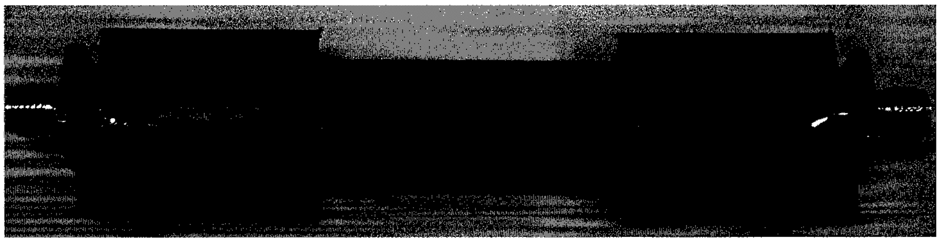

a) Top

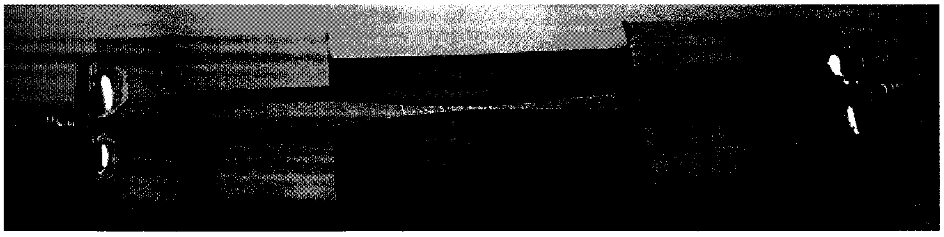

b) Bottom

Figure 52. Slotted-Ground Back-to-Back Balun

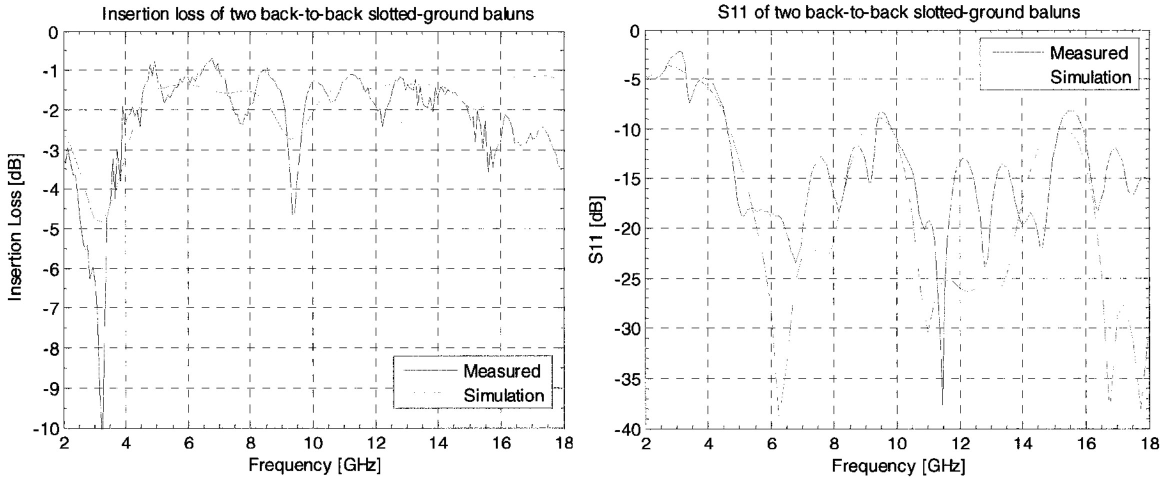

Figure 53. Simulation vs. Measurement of Slotted-Ground Balun

The insertion loss of the measured and simulated results is in very good agreement averaging approximately 1.5dB from 4 to 18 GHz. This would indicate the insertion loss of the actual balun would be 0.75dB. In general, the S11 measured results also overlap quite nicely with the simulated values; however there is some significant deviation in excess of 10 dB from 11.5 to 13.75 GHz and 16.5 to 18 GHz. The addition of the connectors, which were not modeled in the simulations have a definite part in the differences observed.

4.6 Final Remarks Regarding the Baluns

The baluns presented in this chapter have been designed for general applications and not for any specific antenna. The theory of the taper for the first balun, and the theory of the slotted-ground for the second balun can be applied over different frequency bands. The slotted-ground balun was shown to work well as a mode transformer, but was considered too long when trying to impedance match to the high input impedance of the antenna below 3.5GHz. For the most part, the measured results agreed with the simulated results and justified their use as part of the feed for the sinuous antenna. Since circular polarization is desired, an UWB coupler will now be discussed.

5. Coupler Design

The traditional 90° hybrid, also called the Branch-line hybrid, shown in Figure 54 cannot be used for such a wideband application because it depends heavily on the electrical length of a quarter wavelength section to perform the power split and the 90° phase shift.

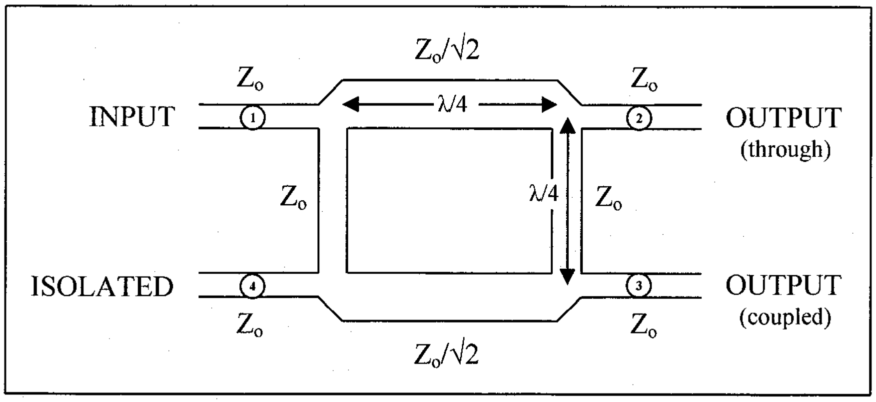

Figure 54. 90° Hybrid (Narrowband)

There has been much research towards the design of wideband quadrature couplers. The type that is most widely used is the tapered line coupler. The tapered line coupler can be either symmetrical or asymmetrical as illustrated in Figure 55. The coupling in a tapered line coupler varies continuously along the coupling region [39].

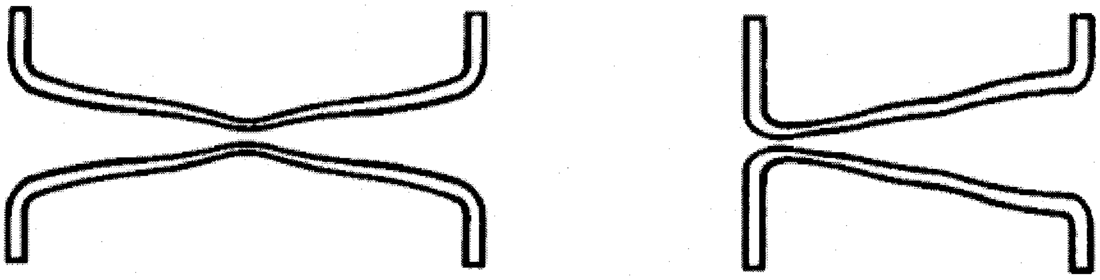

a) Symmetrically Tapered Coupler   b) Asymmetrically Tapered Coupler

Figure 55. Tapered Line Coupler

All four port couplers use the same basic principles. The ports are defined with an input port, an output port, a coupled output port, and an isolated port. When two transmission lines pass within certain proximity of one another, energy propagating from the one line couples to the other line. A 3dB 90° Hybrid operates in a similar manner but ensures the power split between the output port and the coupled output port are equal (within tolerance) and 90° phase shifted relative to one another.

The most important parameters when designing the 3dB 90° hybrid are [39]:

- *Frequency Range*: The frequency range for which the specifications are to be met.
- *Insertion Loss*: The attenuation obtained between the input port and the sum of the two output ports measured with characteristic impedance Z_o.

$$Insertion\ Loss:\quad 10\log\left(1-\frac{P_{coupled}}{P_{in}}\right) \tag{22}$$

- *Isolation*: The difference in signal levels in dB between the input port and the isolated port when the two output ports are measured with characteristic impedance Z_o. Isolation can also be defined between the two output ports.

$$Isolation:\quad -10\log\left(\frac{P_{isolated}}{P_{in}}\right) \qquad Isolation:\quad -10\log\left(\frac{P_{coupled}}{P_{out}}\right) \tag{23}$$

- *Coupling*: The attenuation of a signal at the coupled port relative to the input signal level.

$$Coupling:\quad -10\log\left(\frac{P_{coupled}}{P_{in}}\right) \tag{24}$$

- *Directivity*: The signal level at an isolated port relative to the signal level at a coupled port.

$$Directivity\ [dB] = Isolation\ [dB] - Coupling\ [dB] \tag{25}$$

- *Amplitude Balance*: The power difference between the two output ports.
- *Phase Balance*: The phase difference between the two output ports.

5.1 The Stepped 3dB Directional Coupler

To obtain the 3dB power split, the 90° phase shift, and the desired multi-octave bandwidth, a symmetrical transverse electromagnetic (TEM) mode coupled transmission line directional coupler was investigated. A symmetrical coupler will have symmetry with respect to two planes. Ports 1 and 2 will have side-to-side symmetry with respect to ports 4 and 3. Similarly ports 1 and 4 will have end-to-end symmetry with respect to ports 2 and 3 [40]. The symmetrical stepped coupler is a multi-sectional TEM mode coupled transmission line which relies on each section to provide a monotonically decreasing coupling factor when moving from the centre outwards. This means there will be 'tight' coupling in the centre and 'loose' coupling as you move towards the ends of the coupler which changes abruptly from section to section. Each section of the coupler is designed with a quarter wavelength line at the centre frequency of the desired bandwidth. This electrical length is generally selected to make the calculations easier. The coupling of each individual section in the transmission line is defined by even and odd mode impedances Z_{0e} and Z_{0o} [40][41]. Such impedances are related to the characteristic impedance as follows:

$$Z_0 = \sqrt{Z_{0e} Z_{0o}}\ \Omega \tag{26}$$

When normalized to the characteristic impedance of the input ports, the following equation will ensure perfect VSWR and isolation of the coupler [103].

$$z_{0e} \cdot z_{0o} = 1 \tag{27}$$

From the above formulas, it becomes clear that one needs only to extract the even mode impedance of the individual section to calculate the odd mode impedance, or vice versa. The coupling factor can then be calculated.

$$k = \frac{Z_{0e} - Z_{0o}}{Z_{0e} + Z_{0o}} \quad or \quad C_{dB} = 20\log k \tag{28}$$

Levy [42] and Cristal and Young [40] have done notable work in this area. In both papers, a set of tables have been constructed to list the values of normalized even mode impedances based on certain user specified criteria.

Such criteria would include:

1. The desired amount of mean coupling of the coupler.
2. The amount of odd numbered sections of the coupler.
3. The bandwidth criteria of the coupling.
4. The maximum deviation from the mean (ripple tolerance).

The four design criteria are of course related to one another through certain trade-offs. For example, the amount of sections of the coupler affects the bandwidth, the longer the coupler, the larger the bandwidth as one would expect. The drawback is of course the length of the coupler. The higher ripple tolerance will enhance the bandwidth in the coupler much in the same way higher ripple enhances the roll-off rate in a Chebyshev type filter.

The bandwidth is an extremely important parameter and can be represented by two definitions.

The fractional bandwidth (ω)

$$w = \frac{f_2 - f_1}{f_o} \qquad where\ f_o = \frac{f_1 + f_2}{2} \tag{29}$$

The bandwidth ratio (B)

$$B = \frac{f_2}{f_1} \tag{30}$$

By referring to Cristal and Young's tables, we obtained the following even mode normalized impedance values for a nine section 3dB coupler for a 2-18GHz bandwidth.

$z_{e1} = 1.04112 \quad z_{e2} = 1.12024 \quad z_{e3} = 1.29488 \quad z_{e4} = 1.74863 \quad z_{e5} = 5.18240$

noting that sections 6,7,8, and 9 will be identical to sections 4,3,2, and 1 respectively.

If one was to use these values to calculate the odd mode impedances and then use microwave transmission line theory to calculate the width of the conductors, it would become immediately known that for section 5 this would not be realizable in practice. Section 5, the tightest coupling region, would yield an even mode impedance of 259.12 Ω and an odd mode impedance of 9.64 Ω. Such values are impossible to achieve by any known techniques [42] [43].

Fortunately Shelton, Wolfe, and Wagoner [43] published a simple, but very useful concept that would make the 3dB coupler realizable. Their idea was to connect two 8.34dB couplers in tandem. To illustrate the mechanics of this, we can very easily derive the 3dB output through a basic example of 90° hybrid.

$$-8.34\,dB \;\rightarrow\; 10^{\left(\frac{-8.34}{10}\right)} = 0.14655\,W \;\rightarrow\; 10^{\left(\frac{-8.34}{20}\right)} = 0.3828\,V$$

$$-0.688\,dB \;\rightarrow\; 10^{\left(\frac{-0.688}{10}\right)} = 0.85349\,W \;\rightarrow\; 10^{\left(\frac{-0.688}{20}\right)} = 0.9238\,V$$

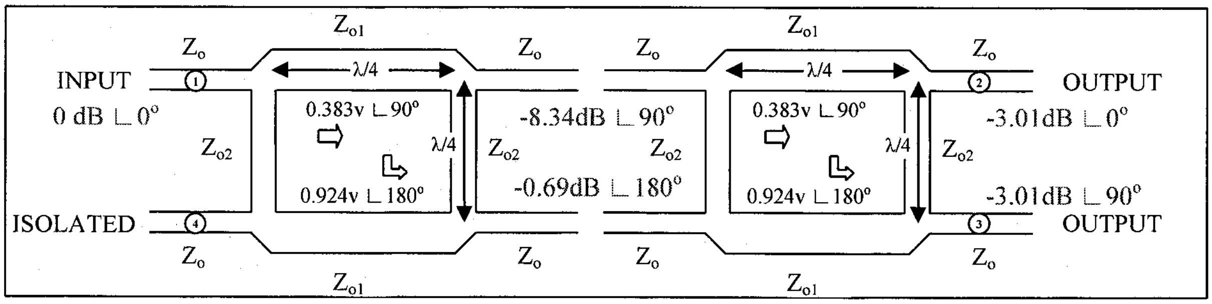

Figure 56. Two 8.34dB Couplers Connected in Tandem

Power at Port #2:

$$= 0.3828\angle 90^o \cdot 0.3828\angle 90^o + 0.9238\angle 180^o \cdot 0.9238\angle 180^o$$
$$= 0.3828^2\angle 180^o + 0.9238^2$$
$$= 0.9238^2 - 0.3828^2$$
$$= 0.7069\,V$$
$$\Rightarrow 20\log 0.7069 \;=\; -3.01\,dB$$

Power at Port #3:

$$= 0.9238\angle 180^o \cdot 0.3828\angle 90^o + 0.3828\angle 90^o \cdot 0.9238\angle 180^o$$
$$= 2\cdot 0.3536\angle 270^o$$
$$= 0.7072\angle 270^o\ V$$
$$\Rightarrow 20\log 0.7072\ \angle -90^o = \ -3.01\,dB\angle -90^o$$

Referring back to the tables in [40] for a nine section 8.34dB coupler with bandwidth of 2-18GHz, we obtain the new even mode impedance values.

$$z_{e1} = 1.02379 \quad z_{e2} = 1.06452 \quad z_{e3} = 1.14687 \quad z_{e4} = 1.33341 \quad z_{e5} = 2.21025$$

To practically implement the coupler we decided to use that of an offset double stripline configuration as shown in Figure 57. To help calculate the line parameters we used Agilent Advanced Design System (ADS) to determine the line width (w) and line spacing (w_o) for a specified permittivity, total height (H), and differential height (H_o) for each section.

Using the same material as the baluns and antennas designed in the previous chapters we designed for the following properties:

$$\varepsilon_r = 2.2 \qquad H = 67 \text{ mil} \qquad H_O = 5 \text{ mil} \qquad H_l = 31 \text{ mil}$$

The summary of results is included in Table 3.

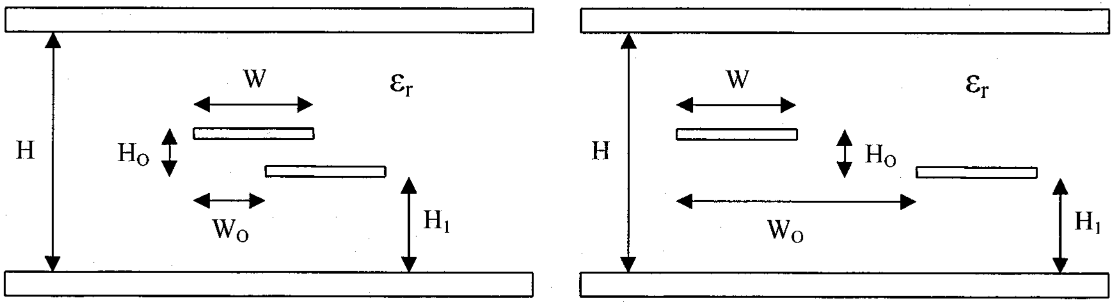

a) Tight b) Loose

Figure 57. Cross Section of an Offset Double Stripline

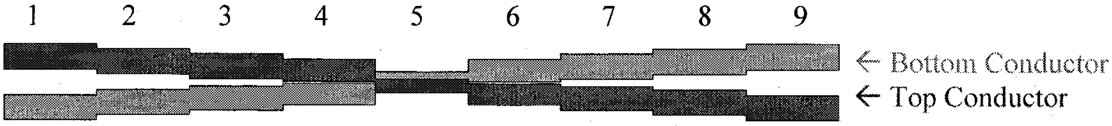

Figure 58. Nine Section Stepped 8.34dB Coupler

Table 3. Stepped Coupler Characteristics

Section:	1	2	3	4	5	ref
z_{0e} (Ω)	1.02379	1.06452	1.14687	1.33341	2.21025	Tables
Z_{0e} (Ω)	51.1895	53.2260	57.3435	66.6705	110.5125	De-normalize
Z_{0o} (Ω)	48.8381	46.9695	43.5969	37.4978	22.6219	Eq. (26)
Z_0 (Ω)	50	50	50	50	50	-
C_{dB}	-32.5759	-24.0903	-17.3174	-11.0552	-3.6070	Eq. (28)
W (mil)	54.7248	54.3075	52.5874	46.7220	29.0134	ADS
W_O (mil)	105.2095	84.3142	67.1654	49.7799	15.1752	ADS

All section lengths are $\lambda_g/4$ long. Where λ_g = 796 mil.

Based on the dimensions from Table 3, we used Ansoft HFSS to create the 3dB coupler from two tandem connected 8.34dB couplers.

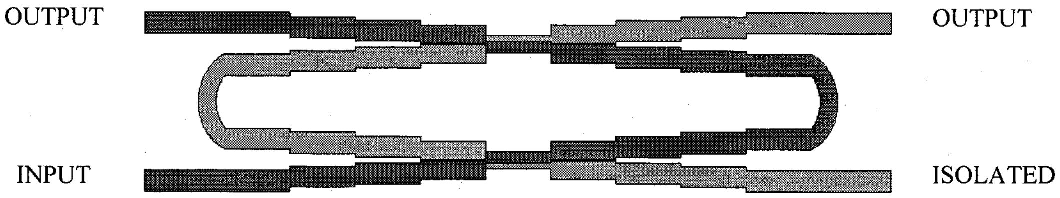

Figure 59. Stepped 3dB Coupler with Ports on the Long End

Unfortunately, the length of this coupler, approximately 2.2 inches, is much longer than the system can allow. If the baluns were to be connected to this coupler beneath the sinuous antenna, the assembly would occupy a large area, which would be way out of the system size specifications. Since, minimizing size and volume of the system are two prime objectives of the design, an alternative method is needed. One might suggest increasing the permittivity of the substrate, however that would not significantly shorten the coupler and it would again introduce complexity in practical realization due to extremely small line traces. The solution was simply to turn the length into the width as shown in Figure 60. This also allows for much simpler balun integration since the unbalanced line ports of the baluns are fairly wide. It is also convenient to orient the coupler in such a manner, because it is almost precisely the same width as the diameter of the sinuous antenna.

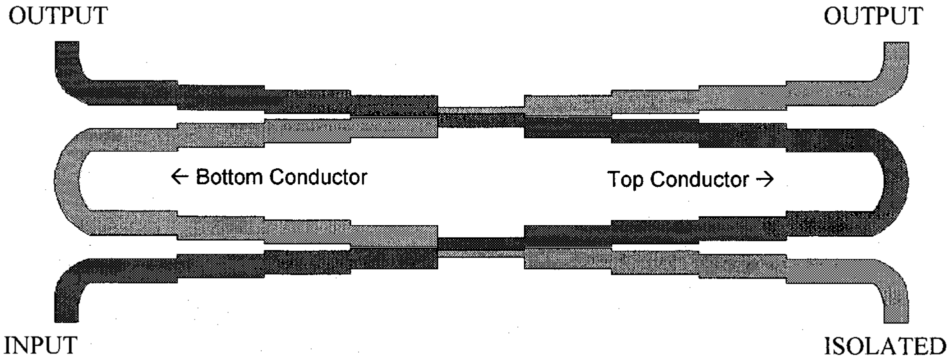

Figure 60. Stepped 3dB Coupler with Ports on the Short End

Figure 61 and Figure 62 show the HFSS simulations for the S-parameters and the phase difference between the two output ports respectively. The results are encouraging since we can observe almost perfectly equal output amplitudes and output phase shift very close to 90°. In both cases however, the performance deteriorates with the upper frequencies. This is also observed with the isolation (S_{41}) from 15 to 17.5 GHz which ranges from 15dB to 10dB and decreases the directivity of the coupler. For such a wide bandwidth, such degradation is to be expected; worse than 10dB isolation would be undesired.

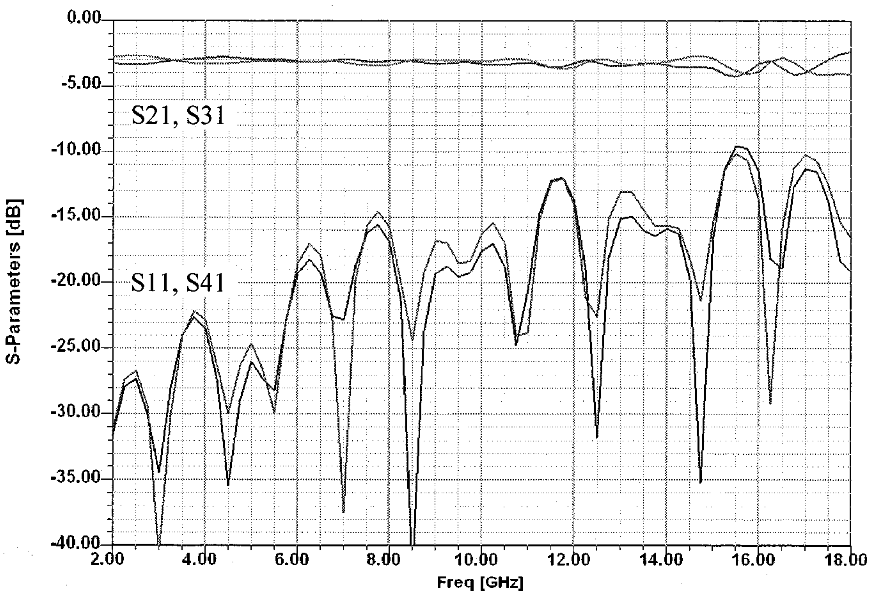

Figure 61. S-parameters of the Stepped 3dB Coupler

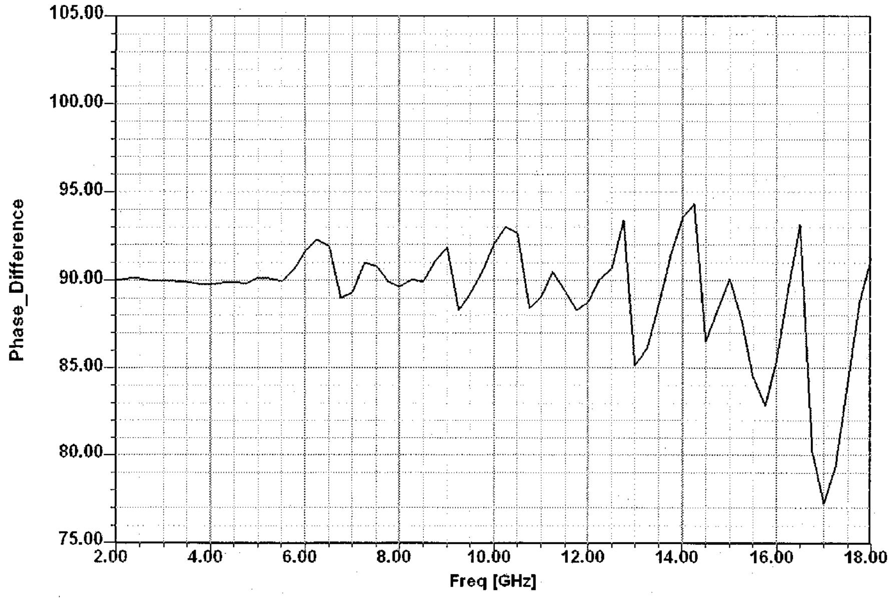

Figure 62. Phase Output of the Stepped 3dB Coupler

The essence behind the operation of the stepped coupler is based on the abrupt change in coupling between adjacent sections of the coupler. However, in practice a finite length is required for this change to occur. As the frequency is increased, this finite length becomes significantly longer and thus has a greater affect on the performance of the coupler's directivity. The parasitic reactances associated with stepped impedance devices result from non-propagating higher order modes present in the vicinity of the discontinuities. To help rid these evanescent modes, a simple linear taper was introduced between all the sections but did not yield any significant improvement in the design and thus further research in non-uniform line techniques was investigated.

5.2 The Non-Uniform Tapered 3dB Directional Coupler

As suggested earlier, the coupling versus distance characteristic of a stepped impedance device is not discrete; it is in fact smooth [44]. Thus a carefully designed taper in the coupler should be the solution to increasing the isolation and hence increasing the directivity and providing better phase balance at the higher frequencies. Tresselt [44] illustrated a method to construct a non-uniform taper that is done gradually enough to permit usage of physical coupling data based on infinitely long and uniformly coupled line modifications. This technique has the practical benefit to be completely specified without the uncertainty and discontinuity associated with the transition regions of the stepped coupler design.

The method used for our stepped coupler transition to a non-uniformly tapered coupler is based on the non-uniform line technique developed by Tresselt. The derivations for this method are fairly involved but are very well summarized in [44]. For the purpose of this thesis, we will summarize the main points and derivations but specifically we will link the design line technique to our coupler.

5.2.1 Basic Theory and Calculations

Given that coupling C, at frequency ω, is the Fourier transform of the reflection coefficient distribution, p(x), one can by inverse Fourier transform determine the required function of coupling versus distance [44][46].

$$C(\omega)=\int_{0}^{d} e^{-\frac{2jwx}{v}} p(x)dx \qquad \text{where } p(x)=\frac{1}{2}\frac{d}{dx}\ln Z_{0e}(x) \tag{31}$$

For our coupler, d will be the overall length and v is the velocity of propagation in the medium. With a few more derivations and transformations, Tresselt then states:

$$\begin{aligned} C(\omega)&=-je^{-j\left(\frac{w}{v}\right)d}\int_{-d/2}^{d/2}\sin\left(2\frac{w}{v}u\right)p_1(u)du \qquad \text{where } p_1(u)=\frac{1}{2}\frac{d}{du}\ln Z_{0e}(u) \\ C(\omega)&=je^{-j\left(\frac{w}{v}\right)d}\sum_{n=1}^{(N+1/2)}\left[\ln\left(\frac{Z((N+3)/2)-n}{Z((N+1)/2)-n}\right)\cdot\sin\left((2n-1)\frac{wd}{vN}\right)\right] \end{aligned} \tag{32}$$

Tresselt proceeds to illustrate that a new distribution function, p$_2$(u), can provide a first-order mean-coupling level of 1.0 over the frequency range of 0 to 1 radian per second.

$$p_2(u)=-\frac{1}{\pi}\frac{\sin^2\left(u/2\right)}{u/2} \tag{33}$$

Thus for our coupler, that requires a mean coupling level of -8.34dB or 0.3828 V:

$$p_2(u) = -\frac{0.3828}{\pi}\frac{\sin^2\left(u/2\right)}{u/2} \tag{34}$$

When solving for the coupling, Gibbs' overshoot phenomenon was present with a number of ripples in the output response. To neutralize these ripples a set of weighting functions are used for compensation. For example, consider a digitally generated ninth order polynomial which approximates the constant unity in an exact precise equal-ripple manner over an interval of 0 to π [44].

$$f(\theta) = 1.2626\sin(\theta) + 0.3931\sin(3\theta) + 0.2049\sin(5\theta) + 0.1170\sin(7\theta) + 0.0927\sin(9\theta) \tag{35}$$

The conventional Fourier representation in the same interval is given by:

$$g(\theta) = \frac{4}{\pi}\left(\sin(\theta) + \frac{1}{3}\sin(3\theta) + \frac{1}{5}\sin(5\theta) + \frac{1}{7}\sin(7\theta) + \frac{1}{9}\sin(9\theta)\right) \tag{36}$$

Numerical evaluation of g(*θ*), will illustrate the usual Gibbs' overshoot phenomenon. This is illustrated in Figure 63.

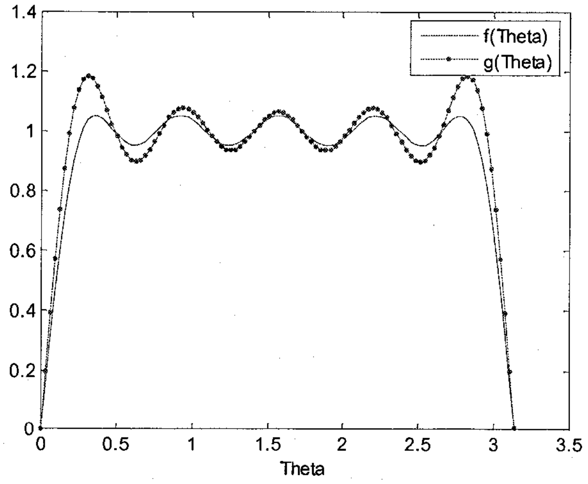

Figure 63. f(θ) and g(θ)

Weighting coefficients can be obtained by dividing the coefficients of the true equal ripple function, f(θ), with the Fourier coefficients in g(θ).

$$
\begin{aligned}
w_1 &= \frac{1.2626}{4/\pi} = 0.9916 \\
w_3 &= \frac{0.3931}{4/3\pi} = 0.9262 \\
w_5 &= \frac{0.2049}{4/5\pi} = 0.8046 \\
w_7 &= \frac{0.1170}{4/7\pi} = 0.6432 \\
w_9 &= \frac{0.0927}{4/9\pi} = 0.6553
\end{aligned}
\tag{37}
$$

While keeping this example in mind and going back to our 8.34dB coupler, we can calculate the weighting coefficients for each discrete section of the stepped coupler previously discussed. The coupling can now be calculated from equation (32).

Section:	**1**	**2**	**3**	**4**	**5**
Z_{0e} (Ω)	51.1895	53.2260	57.3435	66.6705	110.5125

$$
\begin{aligned}
C(\omega) = je^{-j\left(\frac{w}{v}\right)d}\Bigg[&0.5054\sin\left(\frac{wd}{9v}\right) + 0.1507\sin\left(\frac{3wd}{9v}\right) + 0.0745\sin\left(\frac{5wd}{9v}\right) + \\
&0.0390\sin\left(\frac{7wd}{9v}\right) + 0.0235\sin\left(\frac{9wd}{9v}\right)\Bigg]
\end{aligned}
\tag{38}
$$

From the first-order Fourier approximation to -8.34dB coupling, we obtain:

$$
\left|C(\omega)\right| = 10^{\left(\frac{-8.34}{20}\right)} \cdot \frac{4}{\pi} \cdot \left|\sin(\theta) + \frac{1}{3}\sin(3\theta) + \frac{1}{5}\sin(5\theta) + \frac{1}{7}\sin(7\theta) + \frac{1}{9}\sin(9\theta)\right| \tag{39}
$$

Again, the Gibbs' overshoot is present so weighting coefficients from a term by term comparison of equation (38) and equation (39) are calculated.

$$w_1 = \frac{0.5054}{10^{\left(\frac{-8.34}{20}\right)} \cdot 4/\pi} = 1.0369$$
$$w_3 = \frac{0.1507}{10^{\left(\frac{-8.34}{20}\right)} \cdot 4/3\pi} = 0.9276$$
$$w_5 = \frac{0.0745}{10^{\left(\frac{-8.34}{20}\right)} \cdot 4/5\pi} = 0.7643 \qquad (40)$$
$$w_7 = \frac{0.0390}{10^{\left(\frac{-8.34}{20}\right)} \cdot 4/7\pi} = 0.5601$$
$$w_9 = \frac{0.0235}{10^{\left(\frac{-8.34}{20}\right)} \cdot 4/9\pi} = 0.4339$$

Now that the weighted coefficients have been obtained for the stepped impedances of the 8.34dB coupler, we can apply them to determine the weighed area of the positive lobes of the ninth order, 8.34dB distributed coupler by adjusting the mean first order coupling level to 0.3828 as shown earlier. Such lobes are illustrated in Figure 64 of the normalized distribution function, $p_2(u)$.

$$\frac{\sin^2\left(u/2\right)}{u/2} \qquad (41)$$

The figure shows five positive and five negative lobes for a length of 20π, exactly a quarter wavelength longer than the stepped coupler length.

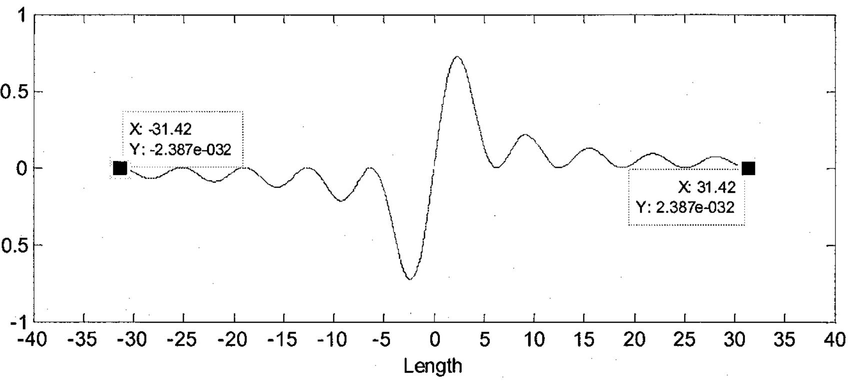

Figure 64. Distribution Function

The desired tapered line coupler can be generated from a coupling coefficient plot versus distance. The procedure is to first obtain the even-mode characteristic impedance of the distributed coupler by a point by point integration of the reflection coefficient distribution shown back in equation (31).

$$p_1(u) = \frac{1}{2}\frac{d}{du}\ln Z_{0e}(u) \qquad \xrightarrow{\text{integral of } p_1(u)} \qquad \frac{1}{2}\ln Z_{0e}(u)$$

Then each solution of u is equated to the weighted area of function, $p_2(u)$, which can provide a first-order mean-coupling level of 0.3828. The weighted area is obtained by integrating $p_2(u)$ over the length of the coupler beginning at increasing minute portions of the coupler length and then multiplying with the appropriate weighting coefficient determined by the corresponding stepped coupler section.

$$p_2(u) = \frac{0.3828}{\pi}\frac{\sin^2\left(u/2\right)}{u/2} \tag{42}$$

After solving for $Z_{0e}(u)$, the coupling coefficient $k(u)$ can be calculated from equation (28) as was done in the case of the stepped coupler. A fully automated Matlab program was created to perform the entire process starting with the stepped even mode impedances used in the stepped coupler to the determination of the even mode impedance versus distance values which ultimately was used to plot the coupling versus distance values.

To generate the new coupler, 200 discrete points were calculated over the length of the coupler. 100 points were taken at the tight coupler section (Section 5 in the stepped coupler) and 100 points were taken for the loose coupling (Sections 1 to 4 in the stepped coupler). The more points the more accurate resolution of coupling versus distance. However a compromise of 200 points was taken between resolution and the complexity of the full EM simulation mesh. We noticed that when importing such a design to Ansoft HFSS, the speed was highly dependent on the number of piecewise linear points used to create the geometry.

The resultant normalized even-mode impedance (z_{0e}) and coupling coefficient (k) functions are plotted in Figure 65. The guided wavelength represented in the graphs is at the centre frequency.

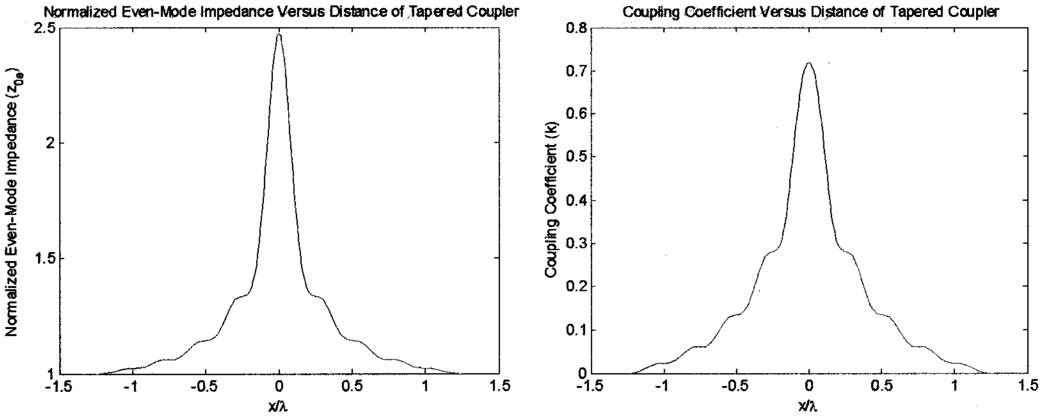

Figure 65. Normalized Even-Mode Impedance and Coupling Coefficient Functions

When compared to the original stepped coupler coupling coefficient we can see the similarities of the two figures.

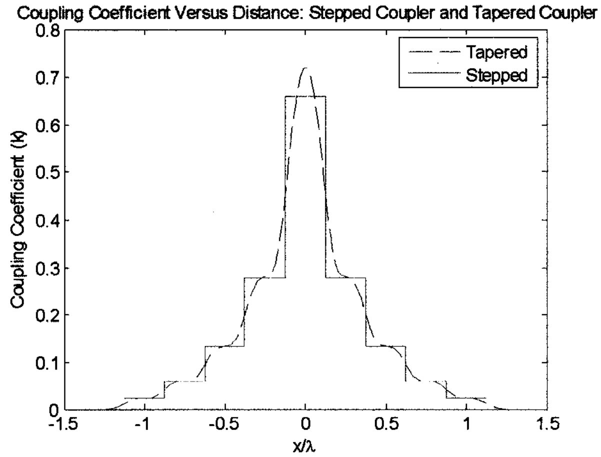

Figure 66. Stepped vs. Tapered Coupling Coefficient Function

With over 200 even-mode impedance values, it no longer becomes practical to use ADS to discretely solve the corresponding widths of the stripline configuration. Thus a secondary Matlab program was written to take the even-mode impedances as an input and output the resultant widths of the lines as well as their respective spacing from each other. The code was based on the formulations by Shelton [47] described in his paper 'Impedances of Offset Parallel-Coupled Strip Transmission Lines'. Shelton distinguishes between tight and loose coupling by illustrating the capacitance effects of parallel-plate and fringing. Appendix C summarizes all the equations used for the calculation of coupling. Randomly selected points were then used to confirm a 100% accuracy when compared with the ADS solutions.

The output of this program illustrates the line width and line spacing as well as the layout of the coupler in space. These plots are shown in Figure 67 and Figure 68 respectively.

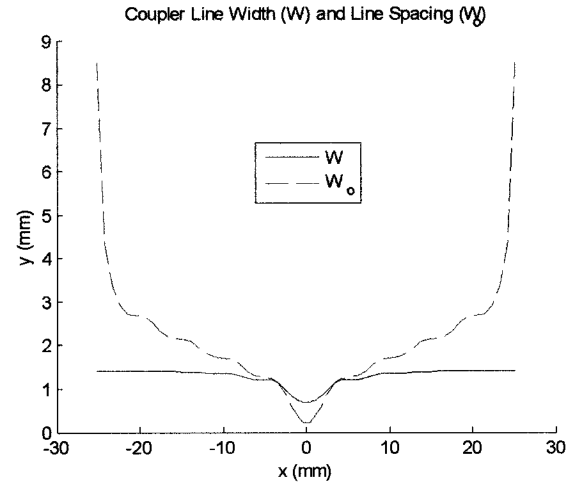

Figure 67. Coupler Line Width and Line Spacing

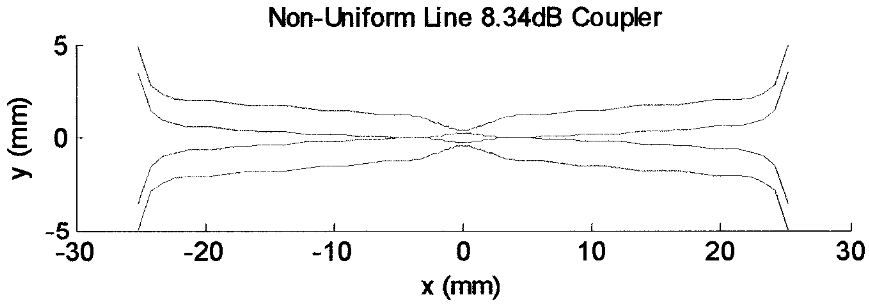

Figure 68. Non-Uniform Tapered 8.34dB Coupler

5.2.2 Non-Uniform 3dB Coupler Simulated Results

After importing the Matlab generated 8.34dB coupler into HFSS 9 via the HFSS 8.5 macro program created for the sinuous antenna, we created the 3dB coupler just like the stepped design. We will now proceed to compare the results between the two types of couplers designed. The plots obtained by HFSS are all based on an 18GHz adaptive mesh with 250MHz step of converged results. The top and bottom surfaces of the couplers were defined as perfect electrical conductors as the boundary conditions.

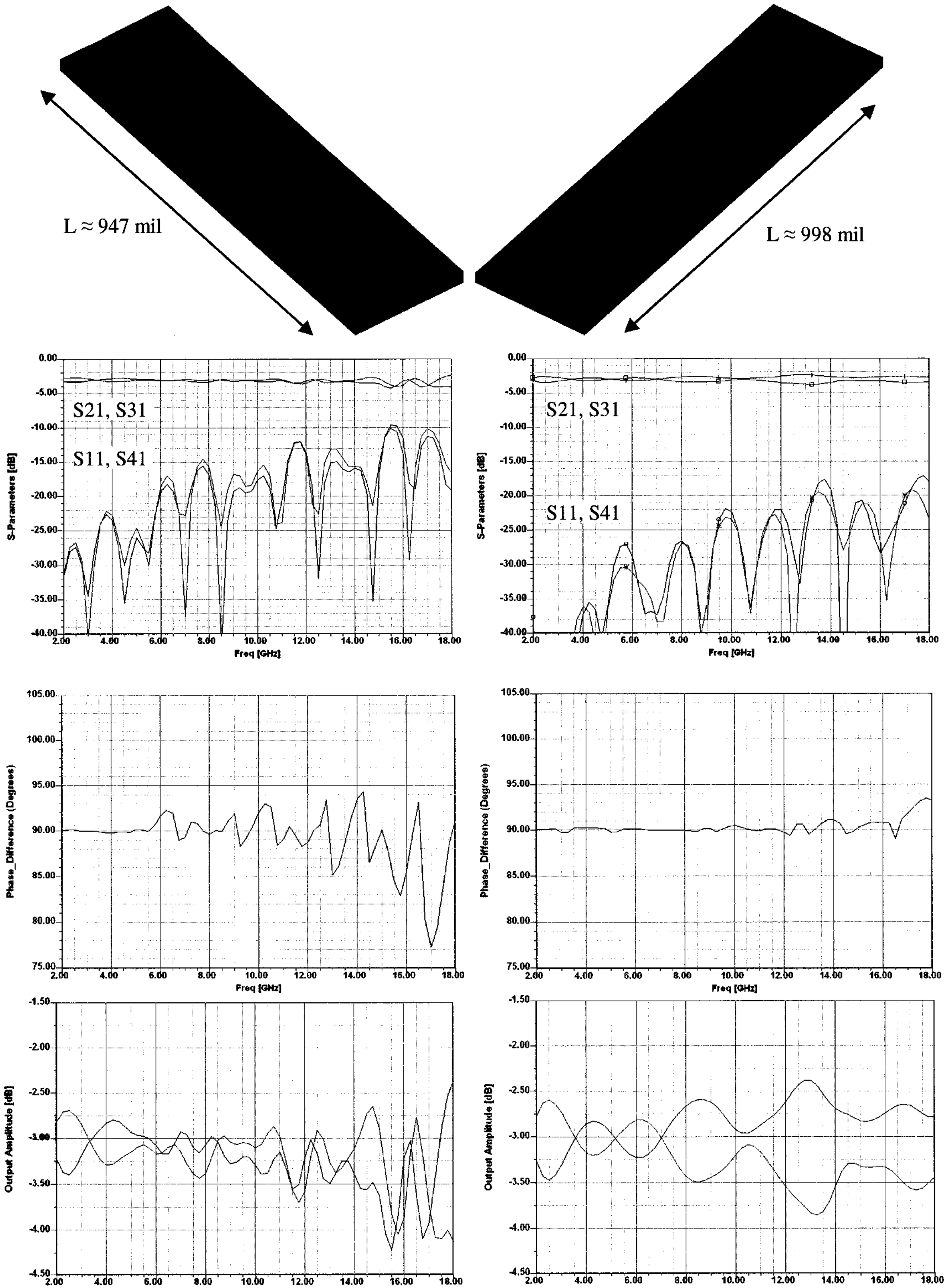

a) Stepped Coupler b) Non-Uniform Tapered Coupler

Figure 69. Stepped vs. Tapered Coupler Simulated Results

The results of the new coupler show a clear and significant improvement in performance throughout the entire band of operation. The return loss and isolation, and hence the directivity of the coupler were improved by about 10dB from 15 to 18 GHz. The performance in the rest of the band, for the most part had even a more substantial improvement. Another considerable improvement would be the 90° phase difference output of the coupler. Such improvement is noticeable from 5 to 18 GHz. The output amplitude balance did not show any significant improvement, and in some cases had minor deterioration. Unlike the stepped coupler, the output of the tapered coupler was centred around -3dB over the entire band. This of course is desired, however, in some applications, it is more important to minimize the difference of the two output levels then it is to keep a mean coupling level of -3dB. The troubled frequency band of the new coupler is limited to about 2GHz, ranging from 12 to 14 GHz. Such minor deficiencies are always to be expected for such an ultra wide bandwidth design. These results show improvement in performance for equal bandwidth couplers compared to the results of other authors [48].

5.2.3 Non-Uniform 3dB Coupler Manufacturing Considerations

To manufacture the coupler, three 5880Duroid sheets are sandwiched together. The upper and lower sheets have a thickness of 31mils and contain a tapered microstrip line. The middle sheet is unclad with a thickness of 5mils. Perhaps a more desirable approach would be to etch both conductive lines on the middle sheet as opposed to the upper and lower boards. This however was not done for reasons that should become evident in the next chapter.

5.2.3.1 Tolerances

Much thought has been placed towards the manufacturing of the coupler. Based on the simulation and optimization phase of the design, and the nature of stripline couplers, it was clear that such a design has very low tolerances for errors introduced by the fabrication process. There were a few issues that we had to carefully consider before manufacturing:

1. The etching tolerance
2. The tolerance error on the permittivity of the dielectric material
3. The tolerance error on the thickness of the dielectric material
4. The permittivity of the bonding film used to glue the three boards together
5. The thickness of the bonding film used to glue the three boards together
6. The dielectric losses of the dielectric material
7. The alignment between the two conducting transmission lines

The first three points have been studied and tested to show negligible deterioration in performance. However, when we attempted to understand the affects of the thickness of the dielectric material, we noticed that this would be a problematic area if one exceeded the tolerance even by a small margin. The tolerance on the thickness of the permittivity, according to the process used at the Communications Research Centre Canada (CRC) was only a few percent and hence was a minor concern. The major problem that resulted was on the same topic of thickness but on the account of the boding film. The bonding film utilized for the construction of the coupler was Rogers 3001, which had a fairly constant relative permittivity of 2.28 and a thickness of 1.25 to 1.65 mils. The permittivity was not an issue due to its proximity to the permittivity of the Duroid that was used (ε_r=2.2). However, the thickness of the glue did pose a significant problem which would affect the separation between the two conductive lines, which would influence the coupling coefficient function. The addition of this finite thickness is an issue that will need to be addressed and eventually can be compensated in a re-design. The variation of this thickness is unpredictable and cannot be modeled. Further investigation towards the nature of the variation suggested that most of the bonding film would be squeezed out to the sides of the conductive traces. This would play in favour of keeping the relative spacing between the conductors close to 5 mils.

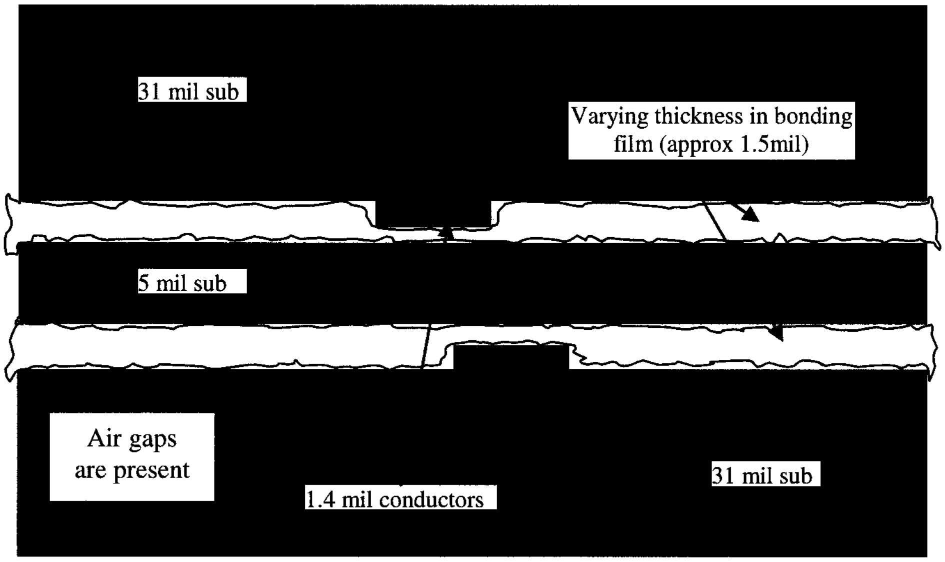

Figure 70. Cross-Sectional Manufacturing Consequence of the Bonding Film

An alternate and more conventional solution would be to avoid the bonding film all together by designing and machining a metallic jig that could encompass all three boards. The boards would be screwed firmly together using screws. This method would have the benefit of a better distributed ground, properly mounted connectors, and most importantly no added thickness due to a bonding film. The main disadvantages include a major increase in size and weight. It is expected that the overall thickness of the coupler would increase from approximately 70mils to 540mils (about the height of one SMA connector). The weight would increase by even a greater ratio. Also the planar dimension of the coupler would also need to be increased to allow room to place non interfering screws for even pressure distribution of the boards. Since one of the main focuses of this thesis is the minimization of size and weight, the research for the development and analysis of the coupler with the bonding film is more attractive. Additional benefits to our approach include less costs and manufacturing time.

Another very important consideration for the manufacturing of the coupler is the alignment of the three layers. In the simulation and optimization phase of the design, a 5 mil offset was introduced to the upper conductive line as a tolerance test. 5 mils were chosen as suggested by the CRC manufacturing team due to a worst case alignment error. Surprisingly enough there was a minor but still evident deterioration in the coupled port output. The through port provided desired performance while the coupled port showed about a 1 dB drop at frequencies above 7GHz. Assuming that a 5 mil offset is a worst case scenario situation, the design was cleared for manufacturing.

5.2.3.2 SMA Connector Integration for Stripline

Since the manufacturing method chosen does not allow for properly mounted connectors, the ideal process for this integration would be to connect the connectors before the boards are bonded together. This is generally the only alternate option for a stripline design and should offer a good solid contact with the trace line to provide minimal discontinuities. Due to reasons beyond our control, this was not an option and thus an alternate approach was developed. The root of the problem is that once the coupler is manufactured, the trace line is buried between bonded layers which prevent any ability to connect the SMA. To resolve this issue, a semicircle gap with a radius of 80mils and depth 31+5 mils was left out of the coupler design at the location of the launch. 80mils was chosen based on the length of the flange of the flat centre conductor. Although 80mils seems like a small length, this minor change had a significant affect on the simulated performance of the coupler. The return losses increased by approximately 10dB and the coupled output response dropped by 3 to 4.5dBs degrading with increasing frequency. This could not be ignored and required two modifications.

We decided that it may be possible to construct the missing semicircle separately, solder the connector onto the trace and securely fit the semicircle in place. Since the flange of the SMA connector is 5mils thick, the semicircle constructed was given a thickness of 31mils as opposed to 31 + 5 mils as in the gap size. An illustration of this is shown in Figure 71.

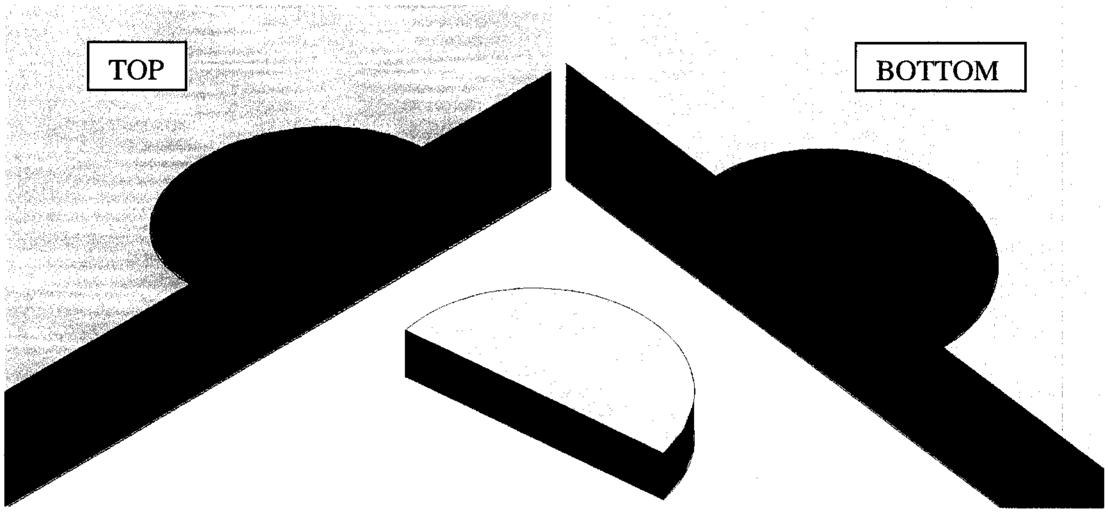

Figure 71. Coupler Modified Port Locations

Secondly we decided to extend the 50Ω stripline length to allow for a smoother transition at the connector discontinuity. This is generally a good practice for any design as it reduces the effects of the connector on the circuit.

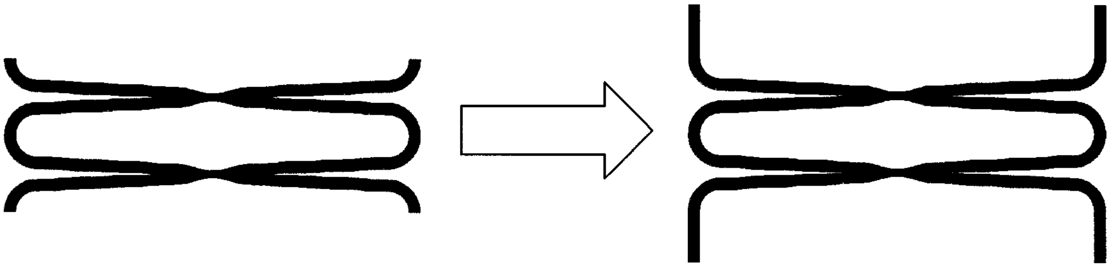

Figure 72. Coupler With and Without Extended 50Ω Stripline

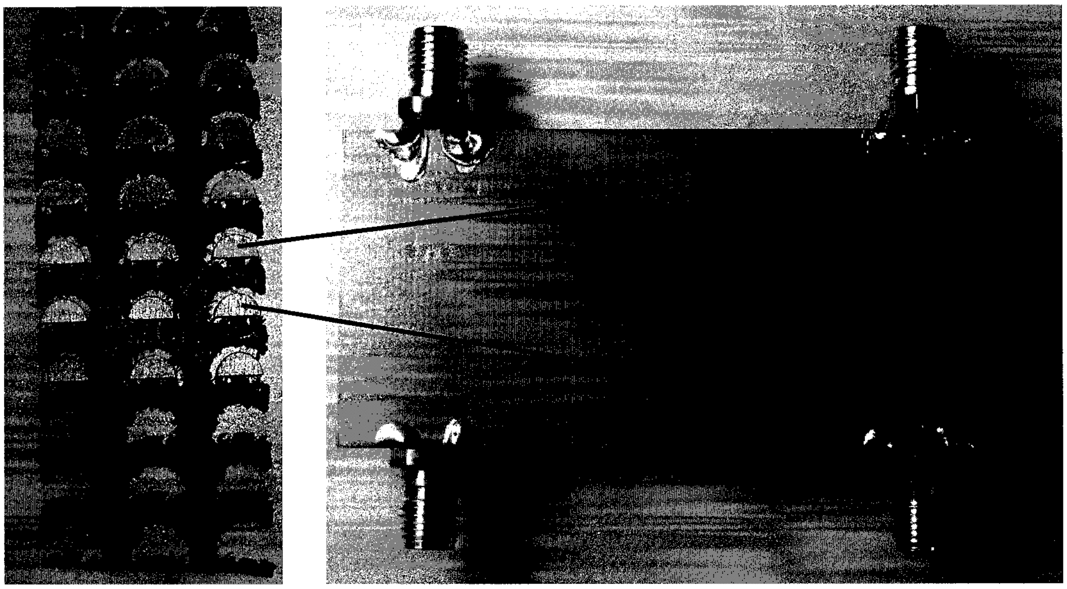

Figure 73. Manufactured Coupler with Semi Circle Cut-Outs

5.2.4 Non-Uniform 3dB Coupler Measured Results

Unfortunately there was a minor error in the manufacturing process of the coupler which affected two of the ports. It was discovered in the process of the removing of the excess glue that was forced out onto the transmission line trace while viewed under the microscope. Under the microscope one could see a clear cut of the trace where the semicircle was cut. The drilling of this semicircle should have been performed before the boards were bonded together. We were able to smooth out the connection using solder but it was not believed to have fully fixed the transition.

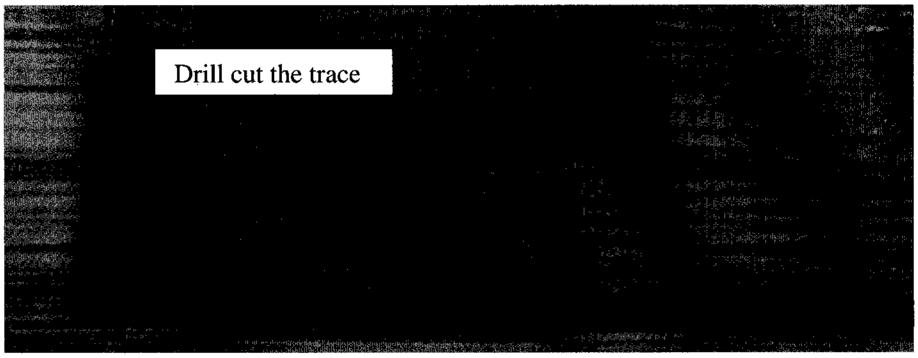

Figure 74. Close-up of a Port from the Coupler

Gold platted flat SMA connectors were soldered onto the ports of the coupler and four semi circles were inserted to fill in the gap to model a proper 50Ω stripline input. One of the undamaged ports was selected to be the input port. The measured results for return loss and isolation of the coupler portrayed similar behaviour with their respective simulated results. By similar behaviour we mean that the peaks and dips of the response were in accordance to the simulated performance. In both cases the absolute magnitude of the losses was notably worse. This is generally a result of the addition of the connectors which were not accounted for in the simulations. The through port output measured results performed precisely as predicted. However, the coupled output results exhibited unacceptable performance beyond 3GHz. The phase differential of the two output ports showed good agreement with the desired results with some deterioration at the upper frequency limit. It is unfortunate that the coupler exhibited significant insertion loss at the coupled port. Such a result is a more prominent case of some of the results that were observed when discussing the tolerances of the coupler.

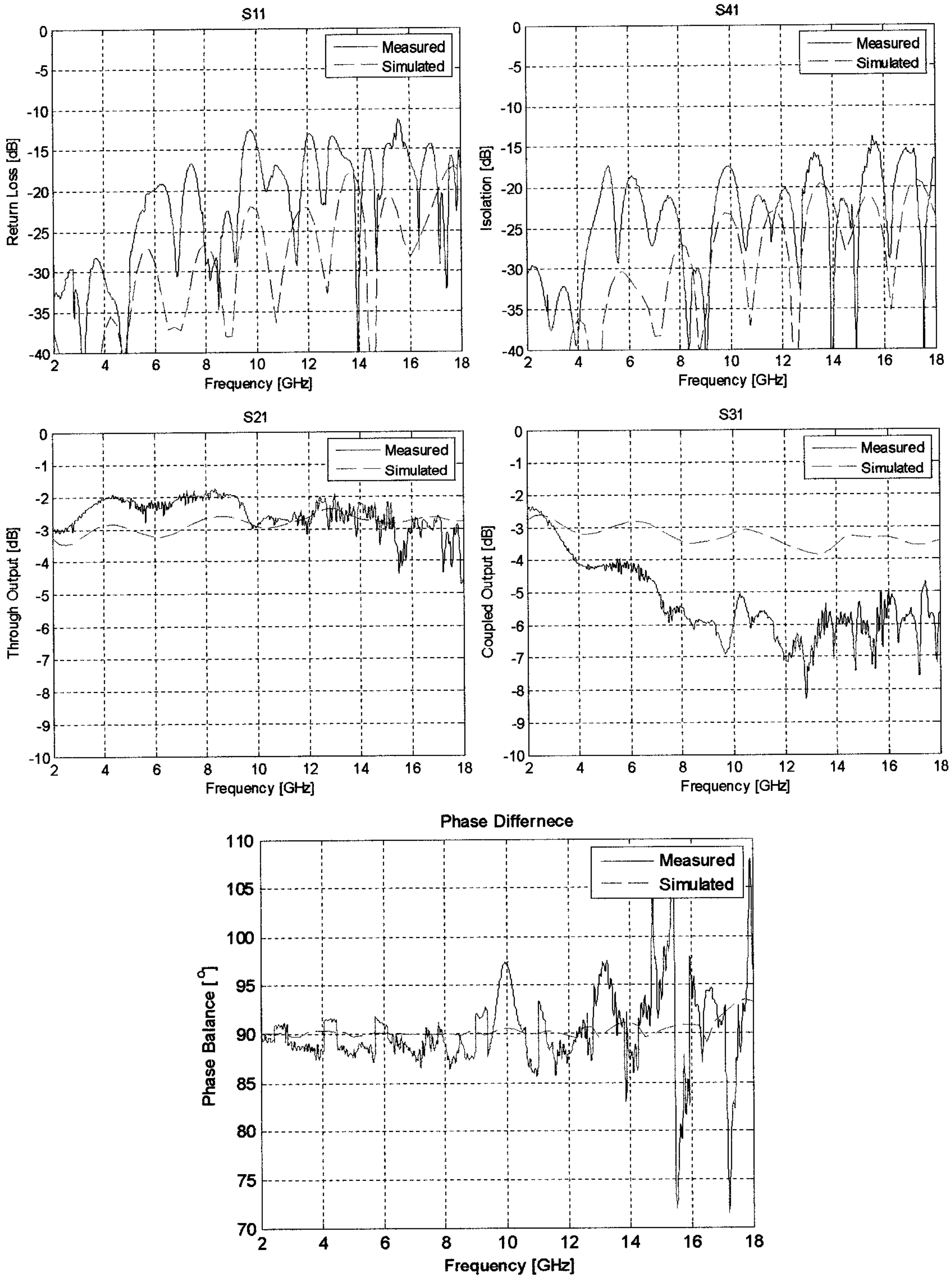

Figure 75. Simulated vs. Measured Results of the Tapered Coupler

The damage done to the ports during the manufacturing process raises uncertainty as to what the nature of the poor performance is. Since only two ports were damaged, it may be possible to analyze the symmetry of the coupler to see if one can extract the magnitude of its effect. Such a study is necessary to understand the cause of the problem which should help minimize the overall time required for a re-design and construction. To do this, the four ports were labelled with a fixed number for constant identification as the coupler was measured with each port acting as the input. Ports 3 and 4 were identified as the damaged ports, and thus should reveal non-symmetrical results. A repeatability analysis was also done for the return loss, and is shown in the legends as measurement A, B, and C. Figure 76 through to Figure 79 portray the measurements with the four configurations.

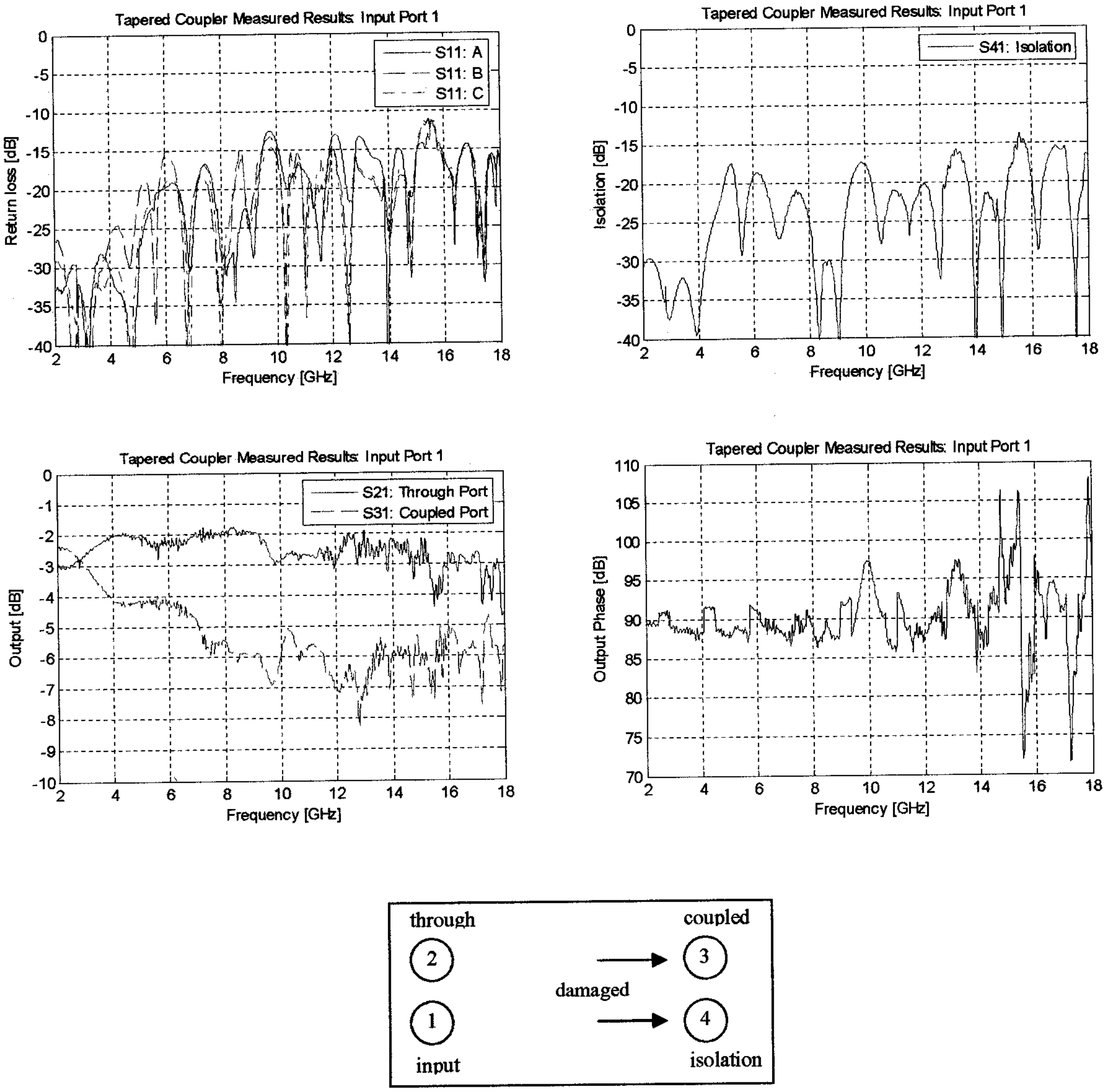

Figure 76. Measured Results of the Tapered Coupler with Input Signal at Port 1

With the input signal at port 1, we measure the same results previously compared with the simulated performance.

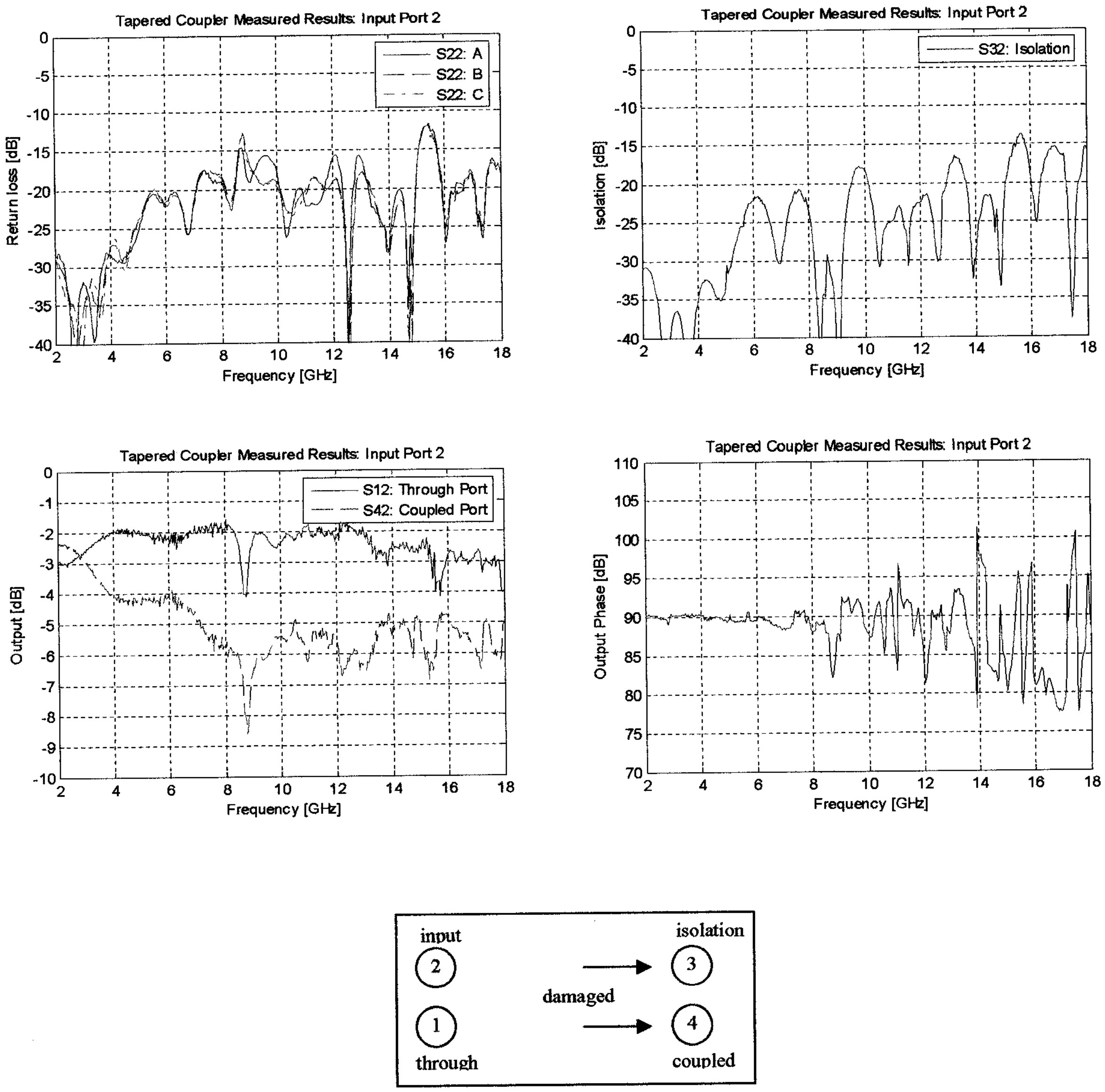

Figure 77. Measured Results of the Tapered Coupler with Input Signal at Port 2

The results here show comparable performance with the previous results suggesting a good reciprocal behaviour between ports 1 and 2. The return loss is below 15dB over the entire band except for a minor peak at precisely the same frequency noted before (15GHz).

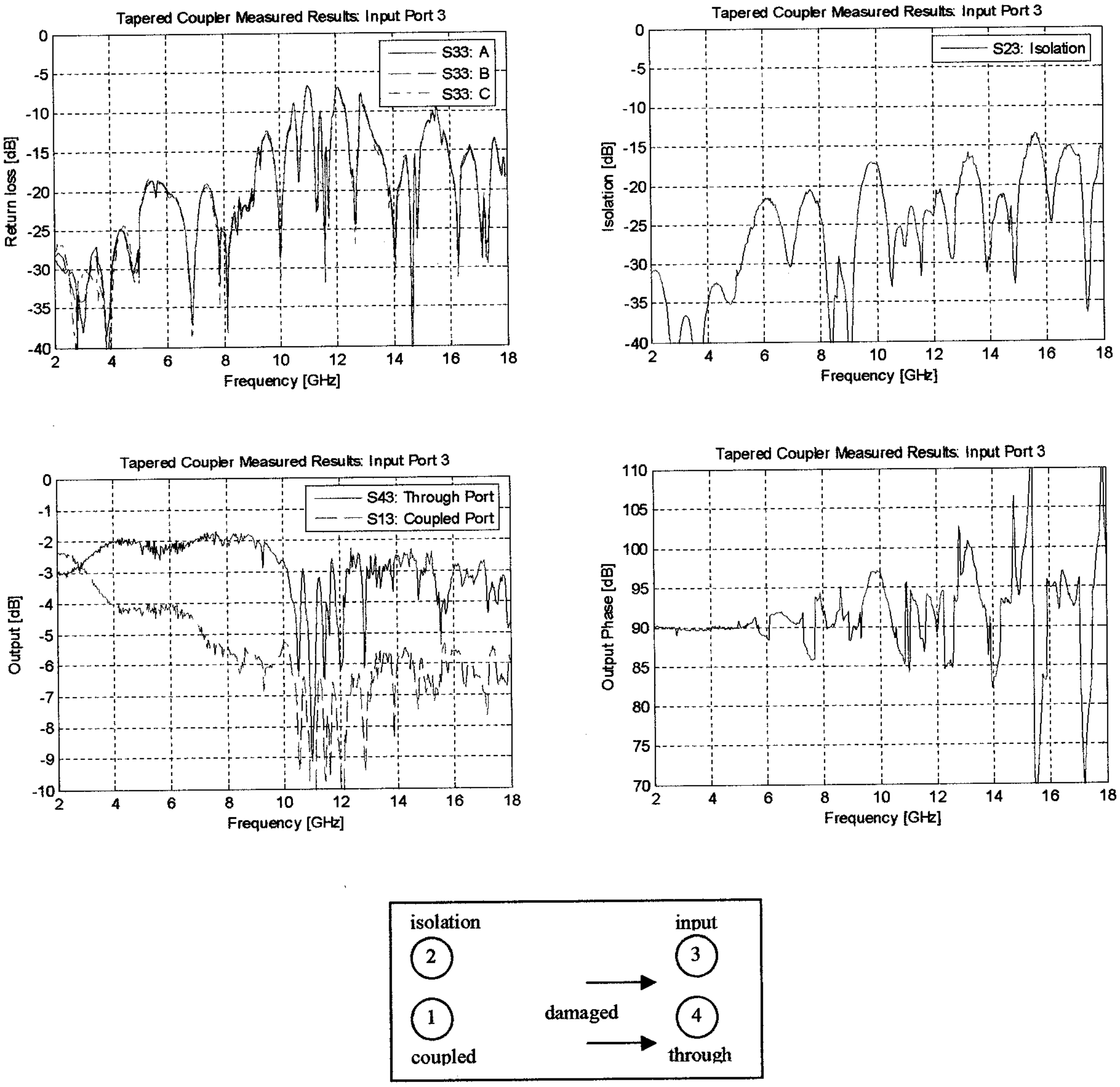

Figure 78. Measured Results of the Tapered Coupler with Input Signal at Port 3

When the input signal was placed at port 3, one of the damaged ports, an important observation is made. There is a significant degradation in performance in the return loss for frequencies between 10.5 and 13 GHz when compared with the first two measurements. Such an increase in reflections is typically observed whenever there is an obstruction or discontinuity in a line trace. The degradation in performance of the two output responses at the same frequency band is a direct result of their dependence on the return loss.

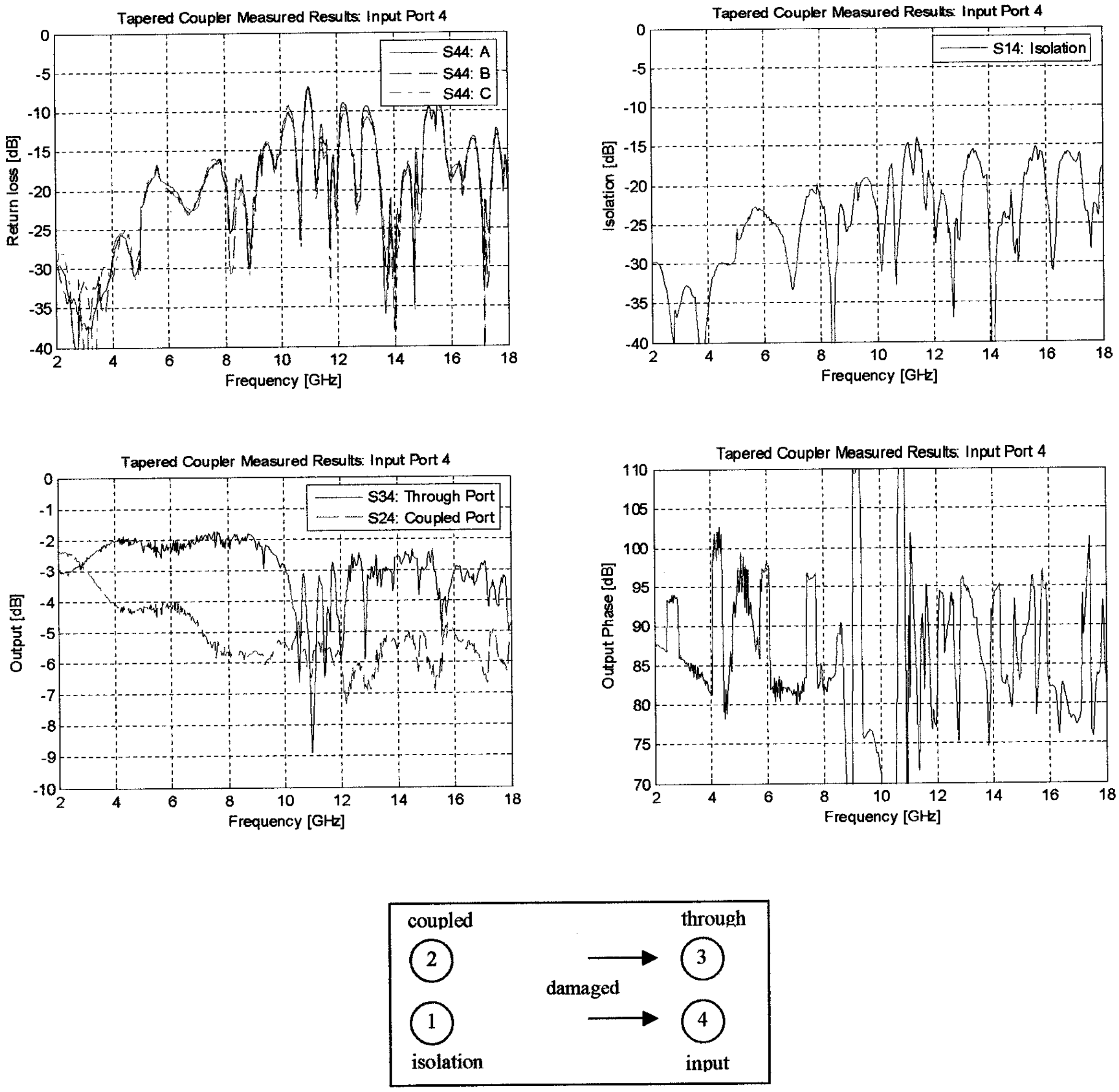

Figure 79. Measured Results of the Tapered Coupler with Input Signal at Port 4

Large reflections are also observed when the last remaining port is used as the input of the coupler. These observations confirm our initial concern about the lack of symmetry which suggests that ports 1 and 2 no longer have side-to-side symmetry with respect to ports 4 and 3. The end-to-end symmetry between ports 1 and 4 with ports 2 and 3 did not seem to be affected.

5.2.5 Final Remarks Regarding the Coupler

The analysis of the coupler suggests that one of the prime reasons for the degradation in performance is in fact due to a manufacturing error. However, due to the significant deviation in the coupled output of the coupler, it is not believed that the manufacturing error was the only reason. It is possible, and even very likely that the topics discussed in the 'Tolerances' section played a major role. It is believed that the combination of the tolerances on alignment, thickness of the glue, dielectric losses, along with the severed traces contributed to the high insertion loss of the coupler. The current performance of the coupler, although not perfect, does suggest that it is in fact possible to obtain the equal power split and maintain a 90° phase differential using the glued approach as opposed to the machined method. There are options that one could take to further improve the performance without sacrificing our desire to maintain the size, weight, and cost of the coupler.

One alternate option is to use a 3mil 5880Duroid laminate as opposed to 5mil. Although 3mil is not a standard thickness, Rogers Corporation has agreed to supply them as it would not be the first time. After the glue has been deposited on either side of the 3mil laminate, the total thickness would be close to 5 mils.

If the transmission lines were to be etched onto the same board, the alignment of the conductors would be significantly improved. This would also eliminate the contribution of the thickness of the glue between the conductors. This would mean we could utilize the standard 5mil board. As mentioned before, this option was not taken due to a conflict in a later design; however it would be possible to compensate.

The simulations of this coupler show the desired results required for this antenna system. It is evident that a second attempt is needed for the practical implementation. Other couplers are intended to be manufactured to replace the current design. It is expected that there will be no manufacturing errors, and much of the previously mentioned issues will be accounted for. Due to the availability of materials and fabrication facility dependence required for a reconstruction process, this work is designated towards future research and development beyond the scope of this thesis.

6. System Integration: Coupler, Balun, Sinuous

Thus far, we have discussed the individual designs of the sinuous antenna, the balun mode transformers, and the 3dB directional couplers. For the sinuous antenna, the radiation patterns were shown to illustrate good three-dimensional symmetry around broadside, representing circular polarization with a 3dB AR beamwidth of about 90°. Two baluns were designed and investigated to achieve a smooth mode transformation, while acting as a wideband matching network. Both baluns portrayed good insertion and return losses over a broad band. Finally a 3dB coupler was designed and optimized using a double offset stripline configuration to achieve a good half power split and a 90° phase differential while maximizing the directivity.

In the past, such designs for log-periodic, spiral, and sinuous antennas have made use of such block-element components. However, the problematic area has always been the practical implementation and integration of the system. More so for the sinuous antennas because of the dual polarization advantage, which requires two baluns instead of just the one. Such a task presents the designer with two problems:

1. The integration of the coupler with the two baluns.
2. The integration of the two baluns with the sinuous antenna

A discussion of each case will proceed followed by their respective electromagnetic simulation. It is unfortunate that a single simulation cannot be made to monitor the overall system performance due to memory restrictions of a 32-bit system. Thus the strategy for the design and manufacture of the sinuous antenna system is as listed below:

1. Design, optimization, and simulation of the sinuous antenna
2. Design, optimization, simulation, manufacture, and test of the baluns
3. Design, optimization, simulation, manufacture, and test of the directional coupler
4. Design, optimization, and simulation of the coupler-to-baluns integration
5. Design, optimization, and simulation of the baluns-to-sinuous antenna integration
6. Design, manufacture, and test of the coupler-to-balun-to-sinuous antenna system

6.1 Coupler to Baluns Integration

Recently Aghdam et al. [48] have attempted a similar configuration which consisted of two separate designs on two separate boards with a simple copper ribbon for the conductive link. Electromagnetically and more importantly mechanically, this may not be the optimal integration procedure. However its benefit is a quick and simple transition of polarization from linear to circular and back to linear if needed.

An alternative method that would maintain this easy transition would be to include SMA connectors on to each of the coupler and the baluns. Thus with a simple male-to-male connector the two devices can be united making a good electromagnetic connection as well as a solid and robust final unit. This method was implemented and manufactured for this thesis.

Another, more desired method would be to somehow integrate the coupler with the balun to produce a single structure. This should enhance the durability, the manufacturing simplicity, and the VSWR of the total structure. The difficulty of the task is not in the transition from stripline to microstrip, but in the fact that the coupler is a multilayered structure while the balun is single layered. Since the coupler and the baluns were conveniently designed with the same substrate material and the same thickness, we were able to incorporate the structures. The design that was developed is a completely new approach and is illustrated in Figure 80.

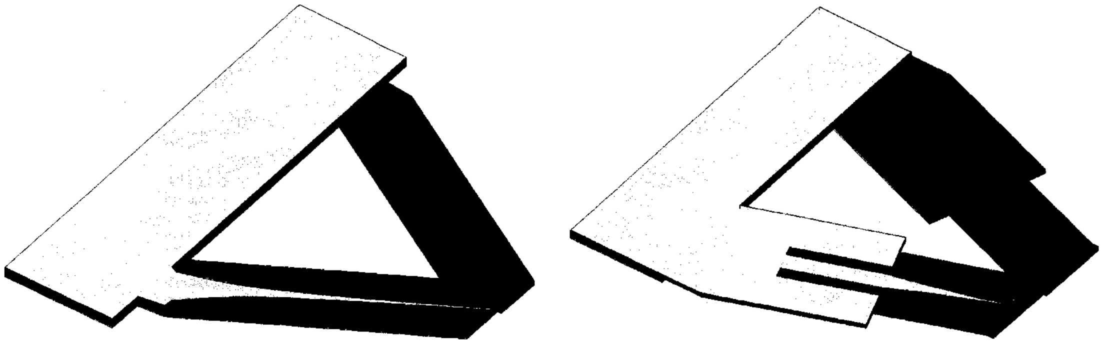

Figure 80. Coupler-Tapered Balun and Coupler-Slotted-Ground Balun Structure

The above figures consist of three substrate boards each:
Top Board – RT5880 31 mil
Middle Board – RT5880 5 mil (Unclad)
Bottom Board – RT5880 31 mil

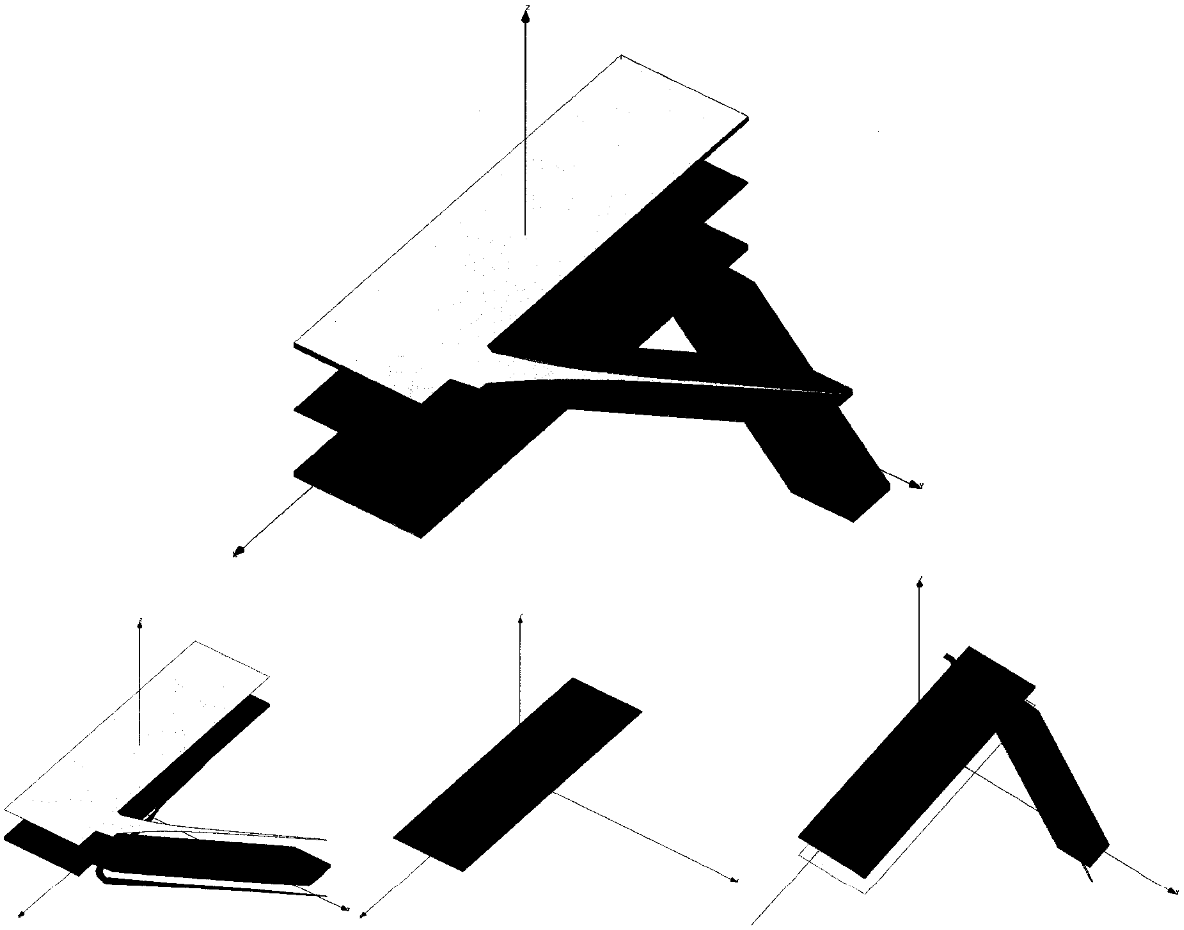

Top Middle Bottom

Figure 81. Three Board Layout

There are numerous advantages with such a layout:

1. Simple manufacturing layout allowing for a structurally robust single unit design.
2. Direct stripline to microstrip transition while avoiding connectors and other discontinuities.
3. Baluns are on separate mutually offset boards and are mirrored with respect to one another, ultimately enhancing the isolation between the two devices.
4. Solves one of the biggest problems for the feed integration of the sinuous antenna because it allows for undisturbed crossing of the balun lines at the BLP which is needed for dual circular polarization.
5. Allows for a totally different and innovative topology of integrating the sinuous antenna on to the same planar surface of the coupler and baluns (Chapter 7).

This device was carefully designed to allow for easy integration with the sinuous antenna. The baluns are oriented inwards so that their BLPs can align directly with the differential input of the antenna. The smoother the transition, the better the symmetry of the four arm antenna, and thus the better the performance. The closer the two BLPs are to each other, the better the symmetry of the antenna, but the worse the isolation will be. Thus a study was performed on the differential length between the BLPs of the baluns by monitoring the electric fields (Figure 83).

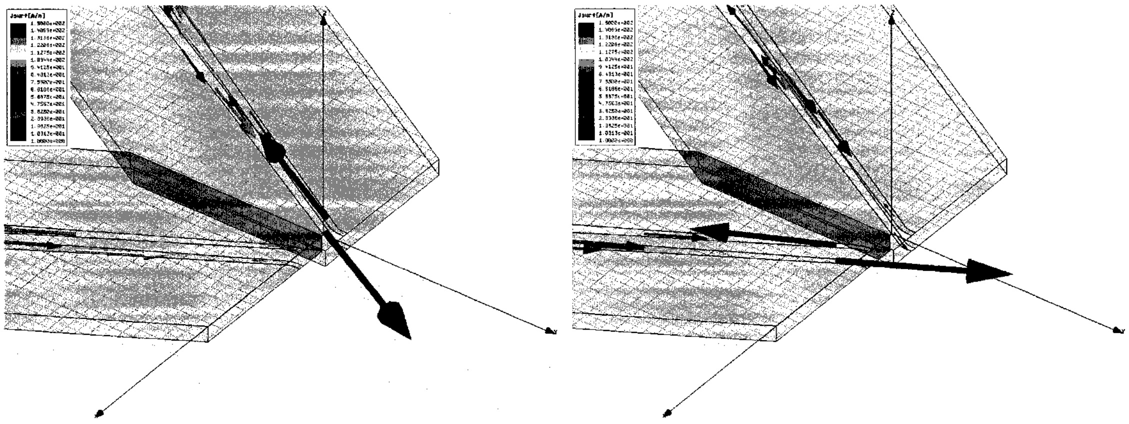

$\varphi = 0^{\circ}$ $\varphi = 90^{\circ}$

Figure 82. Current Distributions at the BLPs of the Baluns Taken at 90° Phase Offset

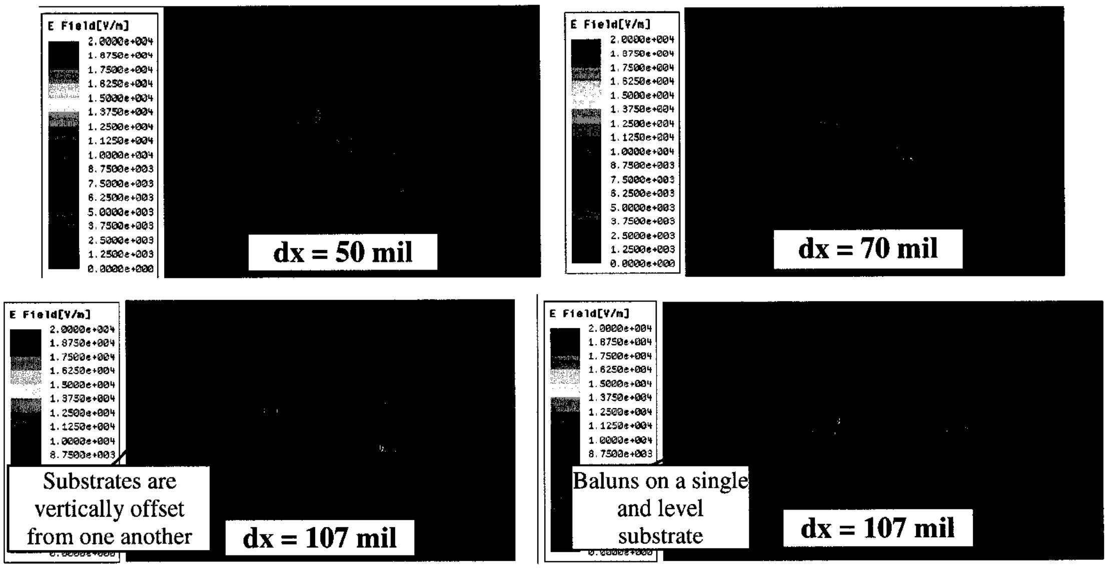

Substrates are vertically offset from one another

Baluns on a single and level substrate

Figure 83. Electric Fields at the Cross-Section of the BLPs of the Baluns

The above plots visually justify the final differential length of 107 mils chosen for manufacturing of the structure. As we progressively increased the separation, the electric field interference between the two baluns decreased. The fourth plot in Figure 83 was included to show that the consequence of having the baluns offset from one another as shown in Figure 81 is actually beneficial in minimizing the isolation.

6.1.1 Coupler Dual Tapered Balun Assembly Simulated Results

Between the two configurations shown back in Figure 80, the tapered balun performance was superior at the lower frequencies and thus will be presented. The coupler - tapered balun combination showed better isolation due to its narrower design allowing less coupling between the two baluns.

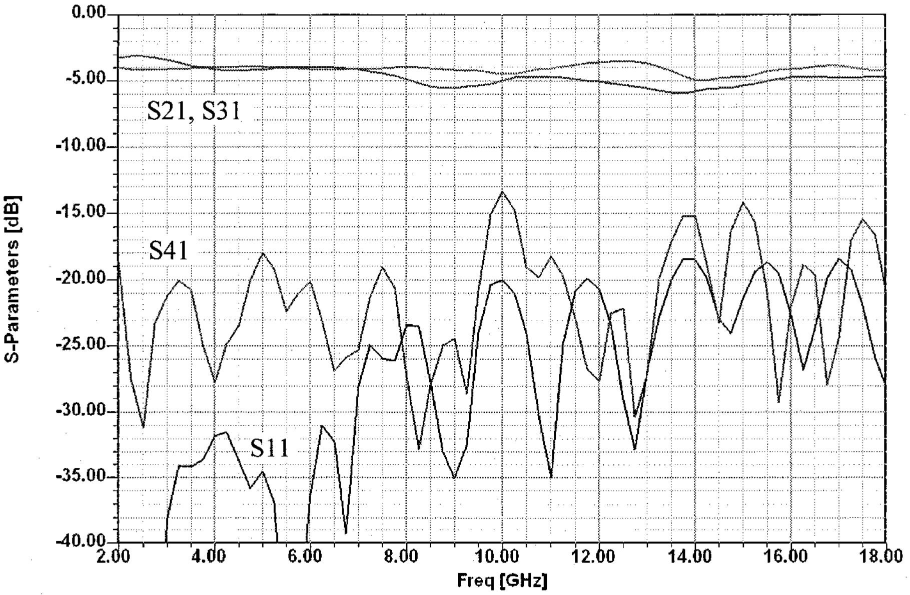

Figure 84. S-Parameters of the Tapered 3dB Coupler Integrated with Two Tapered Baluns

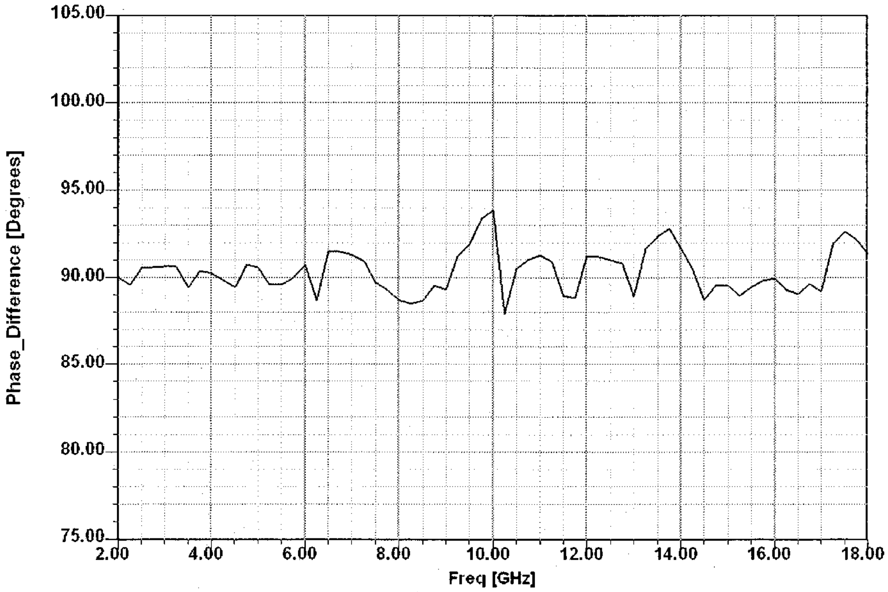

Figure 85. Phase Output of the Tapered 3dB Coupler Integrated with Two Tapered Baluns

The output and coupled port show good amplitude balance centred around -4dB. This seems reasonable, assuming -3dB for the coupler and -1dB for the insertion loss of the respective balun. The return loss is at its worst at 19dB indicating a good stripline to microstrip transition. The isolation is also good over the entire band peaking at the centre frequency to about 14dB. When considering the proximity of the BLPs of the two baluns, the isolation can only be further improved by sacrificing the transition onto the connecting sinuous antenna. The baluns are arranged in such a manner to allow easy integration with the sinuous antenna dual feed points. In the discussion of the sinuous antenna we calculated an ideal frequency independent free space input impedance of around 260Ω. Through HFSS simulations, incorporating a 10mil, 2.2 relative permittivity, we obtained an input impedance of 240Ω. Thus we can now begin to see why it was important to use such a low value for the relative permittivity of the baluns. One of our main design goals was to achieve the shortest possible structure which would require a high permittivity value. However it would not be possible to achieve such a high output impedance value due to non practical line widths. The current design has a width of 10mil at the balanced line port. Any less would not be desired due to limitations in manufacturing, power levels, and structural integrity of the device. The output impedance was simulated for this structure to show desired results.

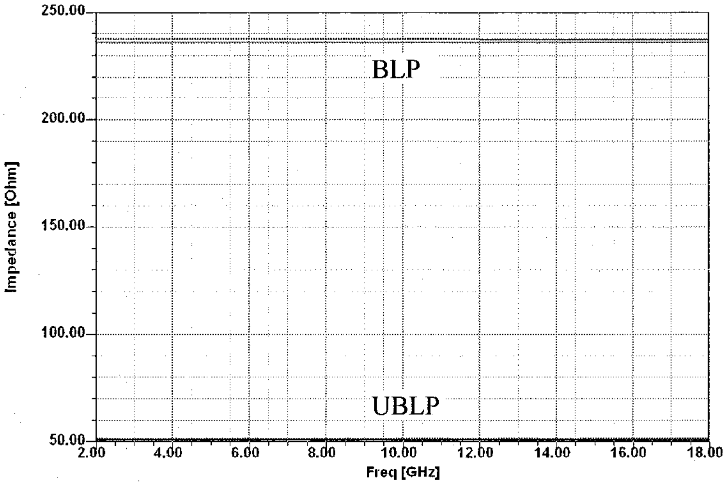

Figure 86. Port Impedances of the Coupler-Balun Structure

The designs including the tapered baluns as well as the slotted-ground baluns were both manufactured so that they may be incorporated into the cavity backed sinuous antenna.

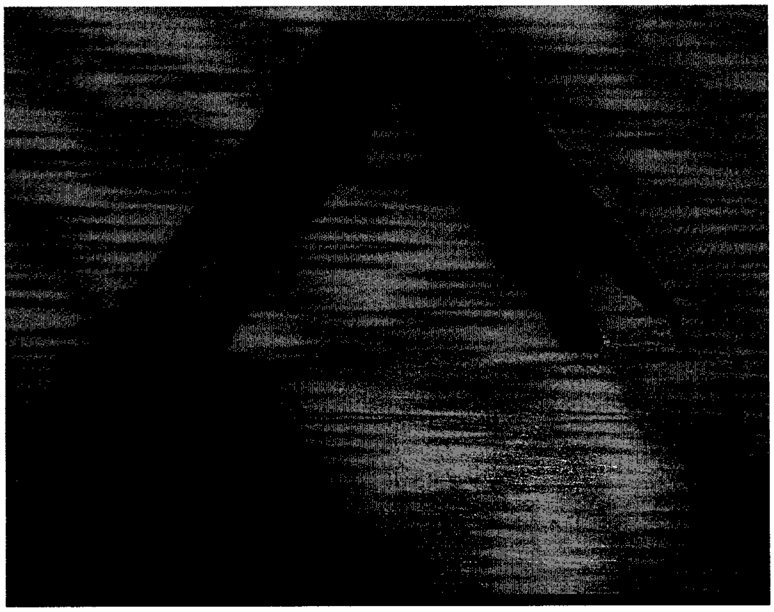

Figure 87. Coupler Integrated with Two Tapered Baluns

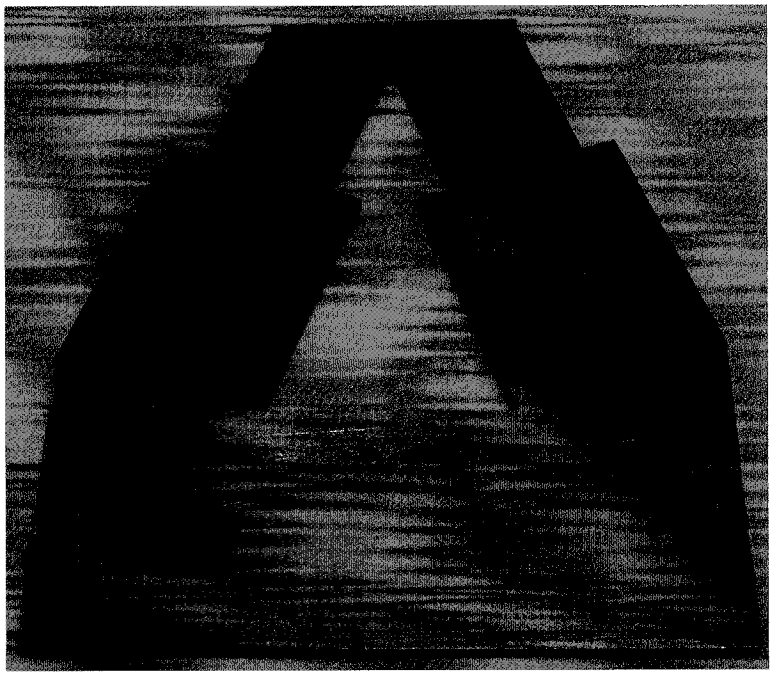

Figure 88. Coupler Integrated with Two Slotted-Ground Baluns

6.2 Baluns to Sinuous Antenna Integration

One of the biggest problems of the sinuous antenna, used for dual polarization, is its complex practical realization and implementation. This is because of the small feed location of the sinuous antenna which has a big effect on the overall symmetry of the antenna. Due to the dual polarization capability of the antenna, it requires that the balun lines intersect each other. This is the first time this option is possible due to the printing of the baluns on two different substrates while maintaining a single unit. This approach however was not taken due to other problematic possibilities and is considered as a highly worthwhile topic for future investigation. Two alternative methods were designed and manufactured. It is worth noting that the baluns were mounted to be at 45° rotation of both arm pairs, which should limit any direct effect on a single polarization. The first configuration resulted in four evenly distributed vias in the sinuous antenna so that four thin wires could be soldered on to the connectors as shown in Figure 89.

Figure 89. Baluns to Sinuous Antenna Wire Integration

An alternative and more practical method is to connect the baluns directly to the sinuous antenna by printing contact points on the back of the antenna.

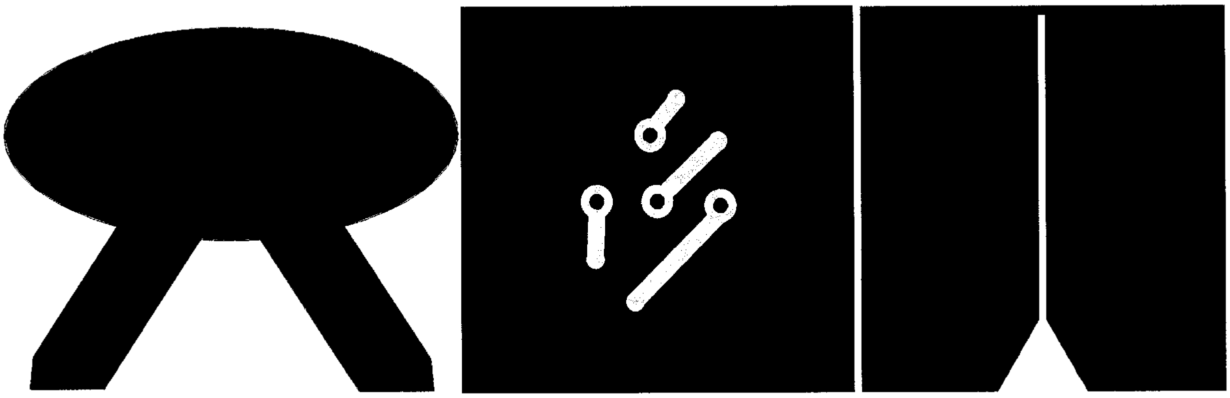

Figure 90. Baluns to Sinuous Antenna Printed Integration

Both types of sinuous antennas were manufactured for testing and are illustrated in Figure 91.

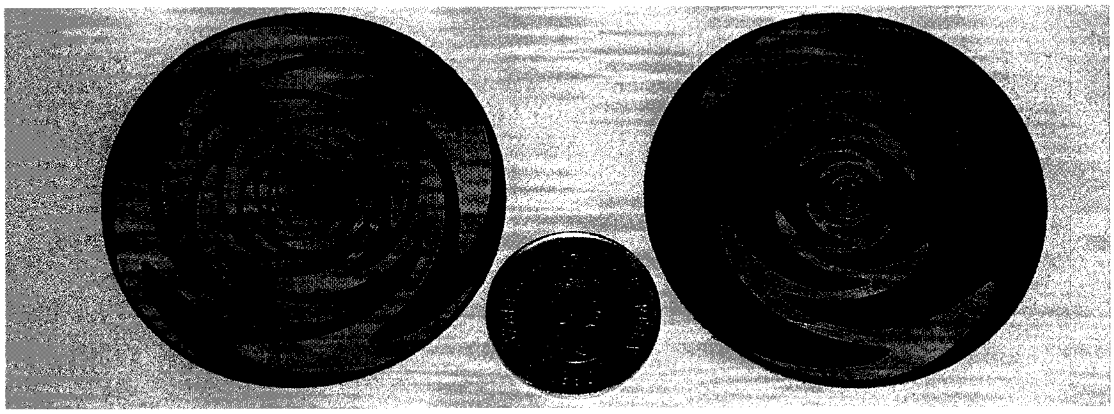

Top

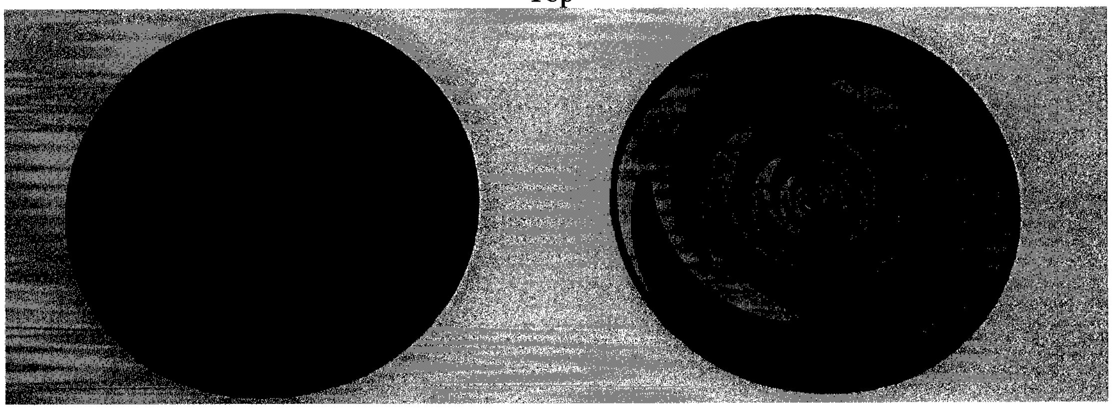

Bottom

Figure 91. Various Different Sinuous Antennas Constructed

6.2.1 Dual-Balun to Sinuous Antenna Simulated Results

The simulations for the configuration in Figure 90 showed better than 12dB return losses for both input ports while maintaining isolation better than 16dB over the 2-18GHz band. P. Gonnet et al. in 1999 [51] constructed two different designs for operation from 2-16GHz and achieved up to 6dB return loss. Aghdam et al. [7] in 2005 achieved experimental results better than 9.5dB from 1-5GHz.

The radiation patterns of E_θ and E_φ were also plotted at 2, 10, and 18 GHz for $\varphi=0^\circ$, 45°, and 90°. Similarly the AR beamwidth was also observed for the same frequency points. One can observe that the wide AR beamwidth has been maintained for the lower frequencies, but does show some degradation as the frequency is increased. At 18GHz we will look at the 4dB AR beamwidth rather than the 3dB AR beamwidth due to a decrease in performance.

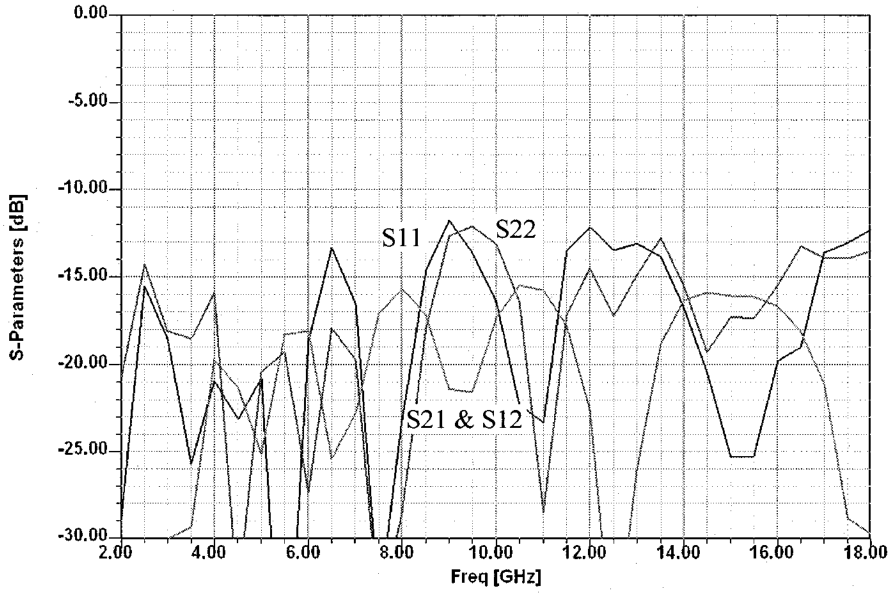

Figure 92. Dual Balun to Sinuous Antenna Simulated Results

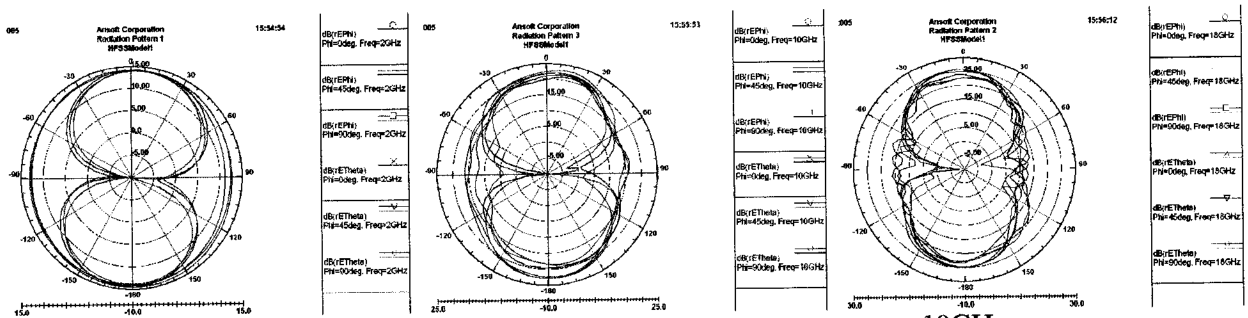

2GHz 10GHz 18GHz

Figure 93. Radiation Patterns at 2, 10, and 18GHz

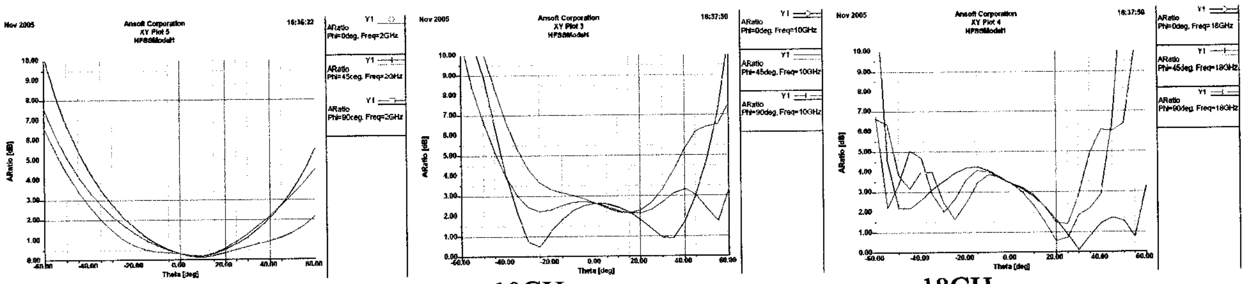

2GHz 10GHz 18GHz

Figure 94. Axial Ratio at 2, 10, and 18 GHz

Since dual polarization is desired, it is necessary to look at the co- and cross- polarization performance of the antenna. Due to the sinuous antenna's complex centre feed point, and high electric and magnetic field interference at the high radiation area of the antenna, obtaining polarization purity is a difficult task over the entire band. P. Gonnet et al. in 1999 [51] claimed they could not achieve better than 10dB cross polarization for frequencies larger then 6GHz. Aghdam et al. [7] in 2005 have claimed to measure better than 14dB from 1 to 5 GHz. Figure 95 shows our results which display the co- and cross- polarizations for a few selected frequencies over the band. Markers have been placed at broadside to show the numerical values. Other than the 2 GHz plot, the cross polarization rejection over the entire band varied from 17dB to 24dB. It is not yet understood why the 2GHz plot displays poor cross polarization rejection.

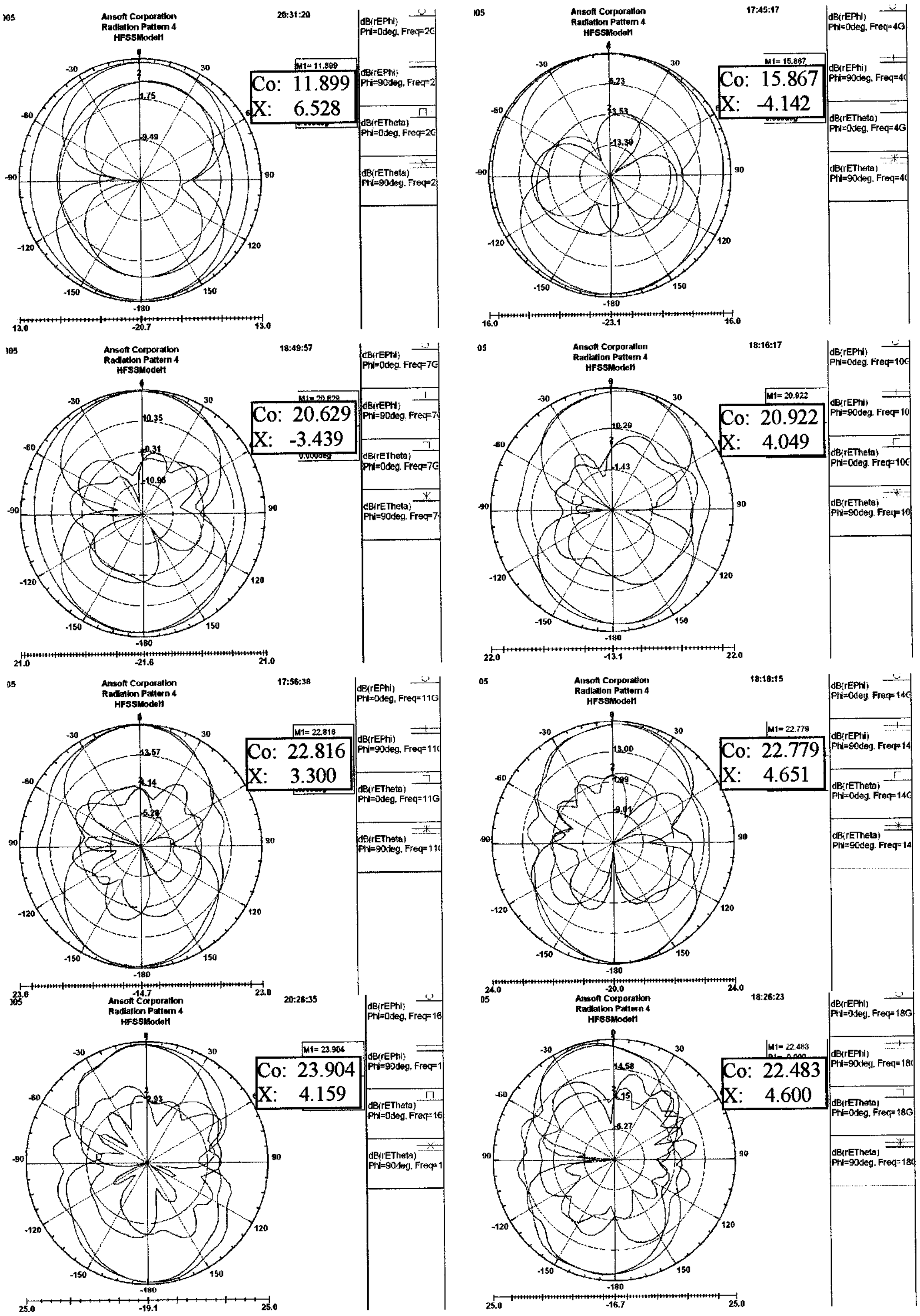

Figure 95. Co and Cross Polarizations

7. Future Research and Development

7.1 Sinuous Antenna Overall System Construction

The delicate nature of the construction of the sinuous antenna system requires special attention in the assembly process. The precise soldering required for the link between feed and antenna cannot easily be completed without contracting out the task. The machining of the cavity and its mechanical integration also demand the involvement of additional outside sources. Since the funds for such tasks were not immediately available and would require an indefinite period of time to complete, the mechanical construction and measurement of the complete antenna system should be considered as future work. For the purpose of this thesis, the antenna system is envisioned to be constructed based on an economical approach. All the material required for the construction of the antenna system was acquired, such as the absorbing material, the foam spacers, and special connectors. The configuration of the system is shown in Figure 96a. The cavity depth and repetitiveness of the absorbing layers need to be further investigated through measurements. Figure 96b displays the configuration without the supporting foam spacers.

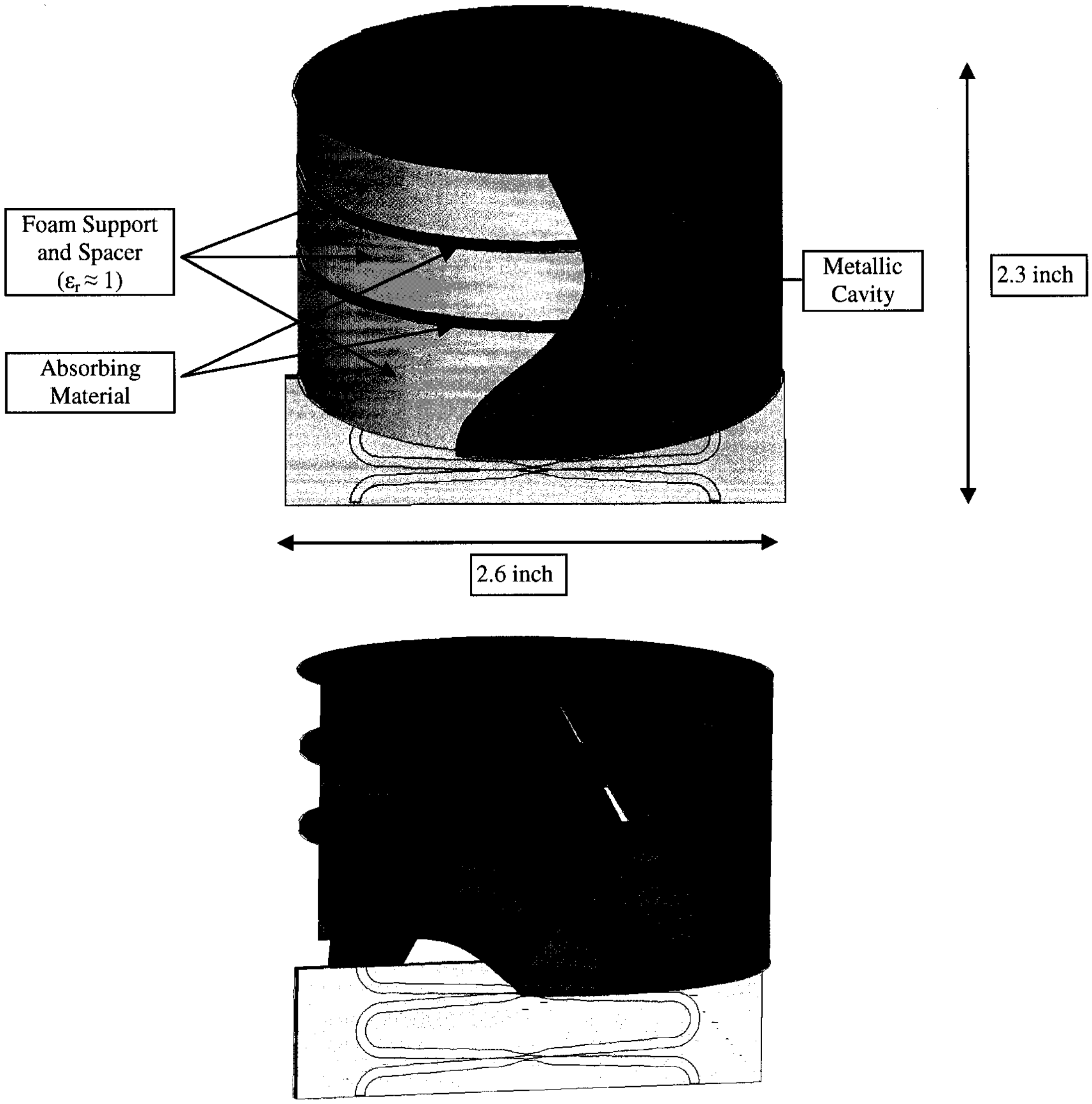

Figure 96. Cavity Backed Sinuous Antenna System Configuration

Since this research is based on the intent that the sinuous antennas will eventually replace the spiral antennas currently utilized in the military aircrafts, it should be expected that they should withstand structural testing conforming to military standards. It is not expected the current designs would meet such standards and thus is definitely an important aspect for further research.

7.2 Innovative Planar Sinuous Antenna System Configuration

The fifth point in the list of advantages for the coupler-baluns design introduced in a previous section discusses a new innovative topology of integrating the sinuous antenna on to the same planar surface of the coupler and baluns. The benefit of this is analogous of the transition of the large and heavy cathode ray tube (CRT) monitors to the liquid crystal displays (LCD). This new sinuous antenna system configuration is shown in Figure 97.

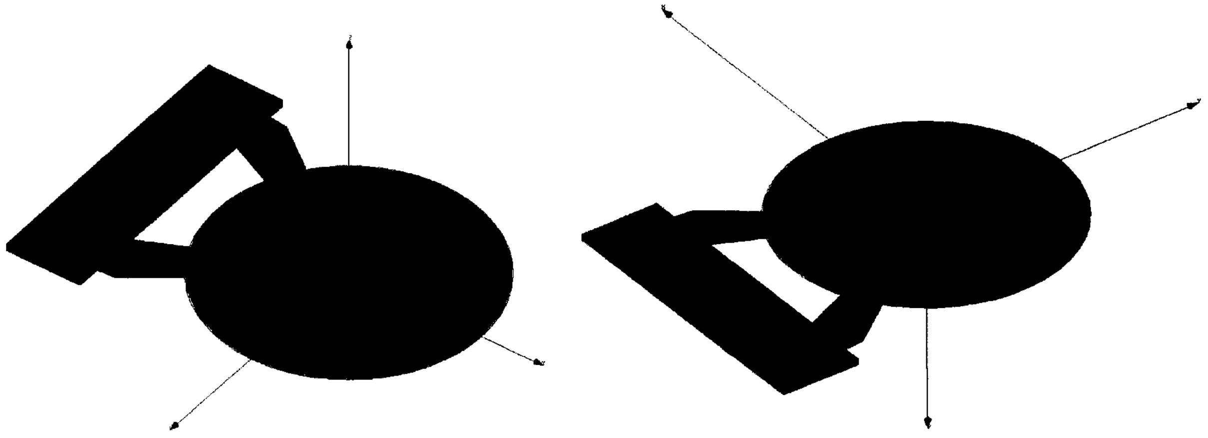

Top Bottom

Figure 97. Planar Sinuous Antenna System Configuration

The benefit of this design clearly shows a planar system with a significant reduction in overall volume. In addition to a benefit in size, this topology allows for a very simple manufacturing process with a significant decrease in costs. This is done by using the 5mil laminate used as a separator between the coupled lines in the coupler as the substrate of the sinuous antenna. This means that the entire system can be manufactured in one process using three bonded layers. Figure 98 portrays this design.

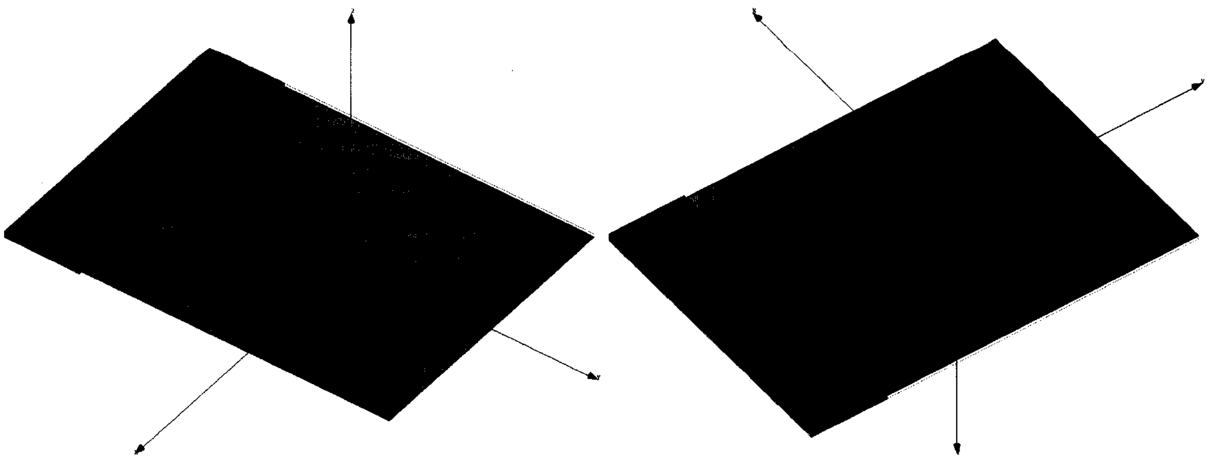

Top Bottom

Figure 98. Single Structure Planar Sinuous Antenna System Configuration

Further investigations are required to understand the effects of the balun feeds which clearly impinge on the radiating elements of the sinuous antenna. Each balun is currently oriented perpendicular to the radiating elements of the opposing arm pair. Much work is still required to understand the feasibility of this design, however, the benefits it proposes are considered to be well worth the effort.

8. Conclusion

In this thesis we designed, simulated, and constructed various ultra wideband sinuous antennas, baluns, and couplers. The feed contact point of the sinuous antenna was modified to allow a smooth transition from the feed network to the first radiating element at the upper frequency band. The two arm sinuous antenna structure was designed and investigated for linear polarizations. The bidirectional patterns exhibited good beamwidth and gain over the entire frequency band. A comprehensive analysis was preformed for the four arm sinuous antenna structure confirming circular polarization with almost identical electric field components (E_ϕ and E_θ) at 45° interval cuts around the azimuth. Various substrate types and thicknesses were investigated to achieve a practical design with optimal performance. A 10mil 5880Duroid substrate was eventually chosen and showed similar radiation patterns, beamwidth, and gain characteristics. Unidirectional performance was then investigated with the addition of a cavity. Investigations of cavity depth, absorbing and spacer depths, as well as selection of absorbing materials were carried out. Further investigations in this area are required to achieve good gain performance at the lower frequencies without sacrificing the circular polarization 3dB beamwidth.

Two different baluns have been designed using Ansoft HFSS. The traditional tapered balun portrayed a simulated return loss and insertion loss of less than 18dB and 1dB respectively over the entire band. Better performance could still have been achieved, but a compromise was made between the length of the balun versus its performance. A second balun was then introduced in this thesis in an attempt to reduce the overall length. The balun was shown to perform the mode transformation using a slotted-ground in about half the length as the conventional tapered balun. The results of this 1:1 balun portrayed better return and insertion losses when compared to the tapered balun. However, the large ratio of impedance transformation required for a good match made the length of the balun too long to be considered for our application. Both baluns were manufactured and measured to have very good agreement with simulations.

To achieve circular polarization, we designed a 2-18GHz symmetrical 3dB 90° directional coupler. We first investigated a stepped 9-section design that portrayed excellent amplitude balance, but suffered from poor phase balance, which seemed to get worse with frequency. The return loss and isolation were better than 10 dB over the entire band. After incorporating a carefully designed non-uniform taper to the stepped coupler, performance was significantly enhanced. The return loss and isolation had an improvement of about 10dB. The phase balance was also stabilized over the entire band. Upon manufacturing of the coupler, the measured results indicated significant deviation from the desired results. Return loss and isolation were degraded by approximately 10dB. Although the through port performed as predicted, the coupled port did not. Reasons were given for this, and suggestions were provided to resolve the problem.

After the sinuous antenna, baluns, and coupler were designed, simulated, and tested, a novel assembly was created to integrate the coupler with the two baluns. The effects of the electric fields were analyzed at the BLPs of the baluns to optimize their relative spacing in order to minimize coupling without sacrificing their role in a smooth transition to the antenna. The feed point of the sinuous antenna was adjusted to allow for the crossing of the balun paired strips which enables a simple and practical feed integration. The final system demonstrated good performance throughout the band, yielding results not previously obtained while conforming to minimized size and weight.

Lastly, we discussed what further research is required to further enhance these designs. Suggestions of new ideas and configurations were proposed and examined.

Appendix A – Neural Models for Spiral Antennas

Neural-Based Model of Spiral Antenna Radiation Patterns for Detection of Angle of Arrival

Neural networks have been continually growing in popularity and have been utilized in many new fields and applications. The neural network technique can replace the traditional 'look-up table' in electronic support (ES) receivers [58]. We will show how neural networks were implemented to model the desired spiral antenna radiation patterns. These spiral antennas are used in ES payload for UWB applications. It is not possible or practical to measure spiral antenna radiation patterns at all the radiation angles due to time limitations. Thus, we present a neural network that can model the measured antenna patterns of two adjacent ultra-wide bandwidth spiral antennas. The amplitude and phase of the spiral antenna radiation field at a given radiation direction can be predicted based on the knowledge of polarization, frequency, zenith angle (θ), and azimuth angle (ϕ). Using polarization, frequency, and the ratio of adjacent antenna received powers as inputs, a neural network was built to predict the angle of arrival (AOA) of an incoming wave.

Once the neural model is well trained and tested, the advantages of using neural networks to model spiral antenna patterns are:

1. Prediction of the radiation patterns at the angles which do not have measured results.
2. Replacement of the traditional look-up table in ES receivers.
3. Adaptation to new measured data.

Various measured spiral antenna patterns have been made as a function of frequency, polarization, zenith angle (θ), and azimuth angle (ϕ). To estimate the angle of arrival (AOA) of an incoming signal, a neural network was designed using frequency, polarization, and a ratio of adjacent antenna received power as input parameters. The output of the network is the direction of arrival of the incident wave.

SPIRAL ANTENNAS

Spiral antennas are ideal in ES payload of various aerial vehicles due to their ultra-wide bandwidth characteristics. Figure 99 illustrates a two-element configuration. Each antenna is mounted on a fixed zenith angle of 60° and offset 90° from each other in the azimuth. We will concentrate on two adjacent elements, which will be referred to as Antenna A and Antenna B. The measured patterns were taken at five frequencies within a 2-18GHz bandwidth. Frequencies S1, C1, X1, Ku1, and Ku2 are in the S, C, X, and Ku bands respectively. The measured radiation patterns were obtained for each antenna, both horizontal (E_ϕ) and vertical (E_θ) polarizations. The patterns of Antenna A and Antenna B are plotted in amplitude and phase in Figure 100. The plots concentrate primarily on the main lobe of each antenna, which is offset by 90° between the two antennas. Emphasis was placed on the patterns representing a 60° zenith angle (θ) as well as the near surrounding angles such as 50° and 70°.

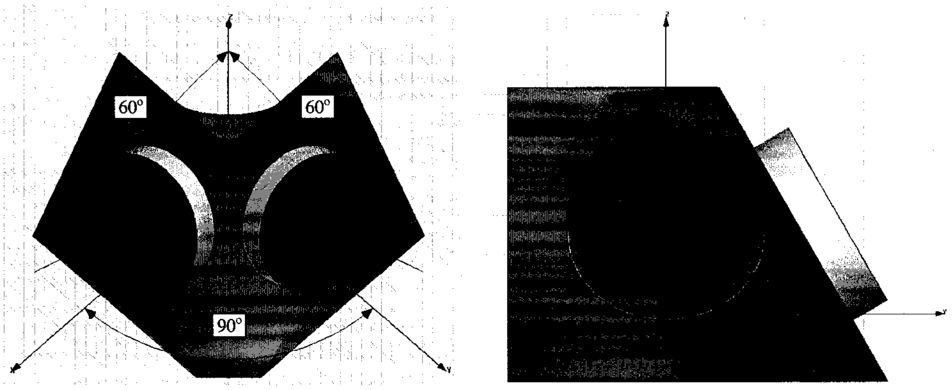

Figure 99. Two Element Spiral Antenna Configuration

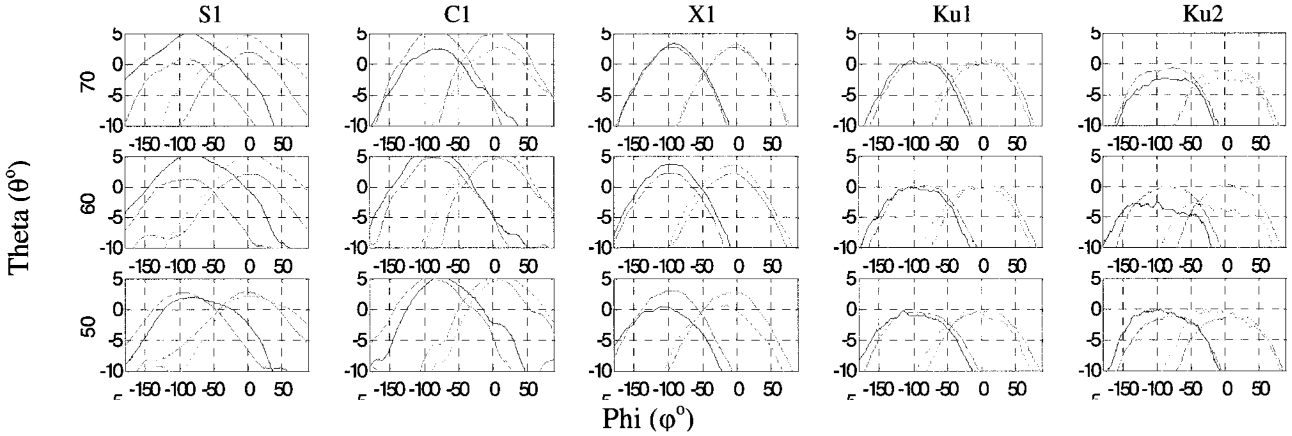

Antenna Amplitude Patterns (dB)

[Antenna A: Red-E$_\theta$, Green-E$_\phi$] - [Antenna B: Blue-E$_\theta$, Black-E$_\phi$]

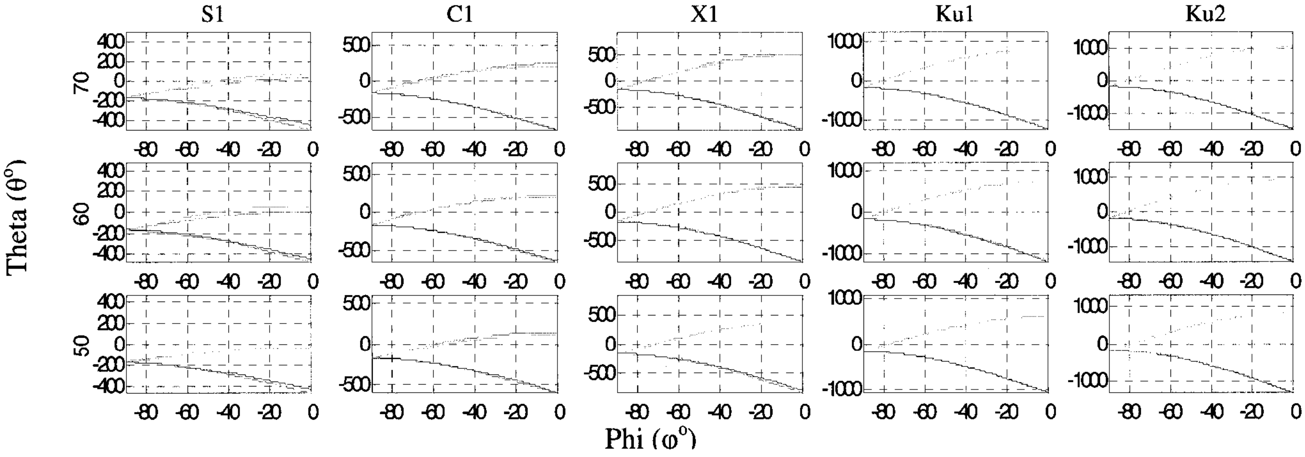

Antenna Phase Patterns (degree)

[Antenna A: Red-E$_\theta$, Green-E$_\phi$] - [Antenna B: Blue-E$_\theta$, Black-E$_\phi$]

Figure 100. Amplitude and Phase Measured Patterns

NEURAL NETWORK DESIGN

The data provided was organized using a Matlab code and is summarized below:

Frequency: S1, C1, X1, Ku1, Ku2
Zenith Angle - θ (Degree): 10, 20, 30, 40, 50, 60, 70, 80, 90
Azimuth Angle - ϕ (Degree): -180.0, -179.9, -179.8, … , 0, … , +179.8, +179.9, +180.0

The above data is for Antenna A and Antenna B, horizontal and vertical polarization, amplitude and phase. The Neural Network utilized was the Quasi Newton method implemented in [16]. A unique neural network was created for phase, amplitude, and azimuth angles for both Antenna A and Antenna B. The data used for training the networks were randomly chosen by a Matlab code and represented approximately 75% of the total data. 20% of the data was used for testing and 5% was left for future verification using the resultant C code supplied with each network.

Criteria of Performance

The performance or accuracy of each neural network will be portrayed in the same manner, primarily:

- Comparison of model output data with measured data
- Percentage error analysis

In each case, an average and a maximum percentage error will be provided. These values can be transferred into absolute errors by the following relationship.

$$\text{Absolute Error} = \text{Percentage Error} \cdot \text{Maximum Range}$$

Neural Nets (1 to 4): Amplitude and Phase

The objective of the following neural networks will be to generate the radiation amplitudes in decibels based on certain inputs. Additionally generate the radiation phases in degrees based on the same inputs. All neural networks generated had a very similar structure. Each had four inputs, 16 to 25 hidden neurons, and one output. The number of hidden neurons varied based on optimizations for each specific neural network. The data file was organized in five columns, containing four input columns and one output column. The first was polarization. The second column was zenith angles (θ), where 50, 60, and 70 degrees were considered. The third column was frequency, where five frequencies were chosen, representing each of the above mentioned bands. Next column included the azimuth angles (ϕ). The angle range utilized in the neural network was based on the radiation pattern plots shown earlier. Antenna A amplitude azimuth angles were ranged from -90° to +90°. Antenna B amplitude azimuth angles were ranged from -180° to 0°. The output column was either amplitude in decibels or phase in degrees. The output phase angles were unwrapped using a Matlab code prior to training the neural network. These four networks could then be joined into a single network with a conditional statement.

Neural Nets (5 to 10): Angle of Arrival

The objective of the next set of neural networks was to obtain the azimuth angle for a given radiation antenna amplitude ratio between Antenna A and Antenna B. From the data plots shown in Figure 100, we can see that the azimuth angles of interest lie between -90° and 0°. Antenna A has been arbitrarily chosen to be the reference amplitude. Thus all ratios were calculated as follows:

$$A / B = A_{dB} - B_{dB}$$

Where A and B represent the amplitudes of Antennas A and B respectively at certain azimuth angles.

Two sets of neural networks were created for θ equals to 50°, 60°, and 70°, one for horizontal polarization and one for vertical polarization. All neural networks generated had very similar structure. Each had two inputs, 14 to 28 hidden neurons, and one output. The number of hidden neurons varied based on optimizations for each specific neural network. The data file was organized in three columns, containing two input columns and one output column. The first input was frequency. The second column was the amplitude ratios in decibels between antenna A and antenna B. The output column represented the azimuth angle for that given ratio and frequency. In general the results were very good, all networks yielded and average error between 1° and 2°. As previously mentioned, these networks can also be combined into a single code for further simplicity.

RESULTS

The first neural network will be visually displayed as explained in the section 'criteria of performance'. The performance of all neural networks is highlighted in Table 4. They are shown as ten different networks only for the purpose of monitoring performance of particular parameters.

1. *Antenna A*
   I1: Polarization: Horizontal and Vertical
   I2: Frequency: S1, C1, X1, Ku1, and Ku2
   I3: Zenith: 50, 60, 70 Degrees
   I4: Azimuth: -90 to +90 Degrees
   O1: Amplitude (dB)

Type of Neural Model: 3 Layer Perceptrons (MLP3)
No. Input / Hidden / Output Neurons: 4 / 25 / 1
Last Training:
Data File: AntAHV50_70_TRAIN.dat
No. of Samples: 40308
Training Method: Quasi-Newton (MLP)
Training Error: 0.008543892
Last Testing:
Data File: AntAHV50_70_TEST.dat
No. of Samples: 10880
Average Error (%): 0.8667751 ≈ 0.2 dB
Max Error (%): 8.687202 ≈ 2.0 dB

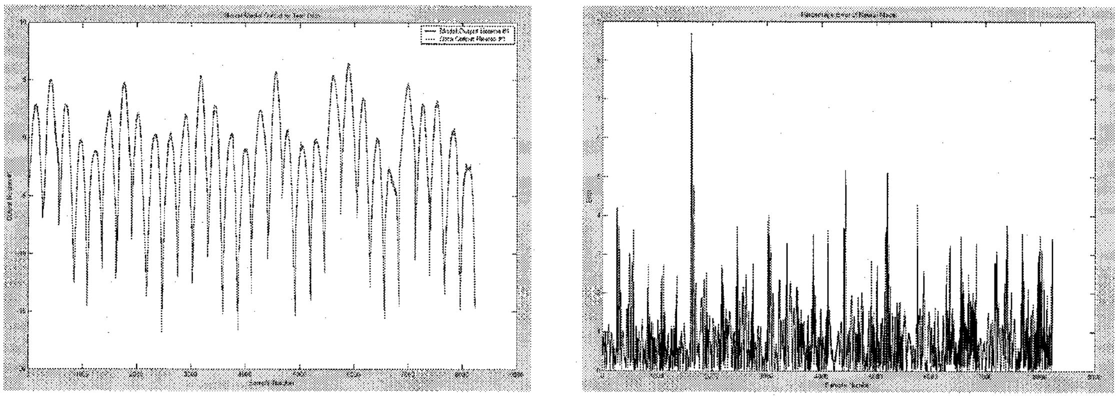

a) Comparison of Data b) Percent Error

Figure 101. Neural Network #1: Ant. A. 50°-60°-70° Zenith

Table 4. *Neural Networks Results Summary*

	Antenna	**Frequencies (GHz)**	**Polarizations**	**Zenith Angles (°)**	**I1**	**I2**	**I3**	**I4**	**O1**	**Avg. Error**		**Max. Error**	
										%	**Abs**	**%**	**Abs**
1) Ampl.	A	All	Horiz. & Vert.	50,60,70	Polarization	Frequency	θ	ϕ	Ampl.	0.8668	0.2 dB	8.6872	2.0dB
2) Phase	A	All	Horiz. & Vert.	50,60,70	Polarization	Frequency	θ	ϕ	Phase	0.1130	0.4°	0.7292	2.6°
3) Ampl.	B	All	Horiz. & Vert.	50,60,70	Polarization	Frequency	θ	ϕ	Ampl.	0.9109	0.2 dB	5.7060	1.3dB
4) Phase	B	All	Horiz. & Vert.	50,60,70	Polarization	Frequency	θ	ϕ	Phase	0.0922	0.3°	0.6264	2.3°
5) Ratios	A & B	All	Horizontal	50	Frequency	Ratio (A/B)	-	-	ϕ	0.4082	1.5°	1.9508	6.8°
6) Ratios	A & B	All	Vertical	50	Frequency	Ratio (A/B)	-	-	ϕ	0.4184	1.5°	4.2702	15.4°
7) Ratios	A & B	All	Horizontal	60	Frequency	Ratio (A/B)	-	-	ϕ	0.4517	1.6°	8.9706	32.0°
8) Ratios	A & B	All	Vertical	60	Frequency	Ratio (A/B)	-	-	ϕ	0.5561	2.0°	8.7809	31.6°
9) Ratios	A & B	All	Horizontal	70	Frequency	Ratio (A/B)	-	-	ϕ	0.3180	1.1°	2.9820	10.7°
10) Ratios	A & B	All	Vertical	70	Frequency	Ratio (A/B)	-	-	ϕ	0.4482	1.6°	2.1922	7.9°

The effectiveness of ES payload of an aerial vehicle directly depends on the quality of the antenna system aboard. To enhance direction-finding (DF) performance, multi-element antennas were employed. The spiral antennas considered were carefully designed and oriented for optimal performance. It is not possible to measure spiral antenna radiation patterns at all the radiation angles due to the limitation of the antenna pattern measurements. Thus, trained by measured spiral antenna patterns obtained in a microwave anechoic chamber, a set of neural networks has been successfully designed to model the spiral antenna radiation patterns. Using these neural networks, the spiral antenna far field radiation characteristics can be calculated at any radiation direction. To fulfill different applications, three different types of networks have been designed. The prediction of amplitude and phase, and most importantly a method to predict AOA was demonstrated.

Appendix B – Automated Program

The C++ code that was written was a top-level general code that would import Matlab generated data and create an HFSS 8.5 macro language to generate the particular geometry of the structure in HFSS. The C++ code is designed with a user interface to allow the user to specify certain parameters relating to the geometry of the structure. It was also designed to automate the FEM problem definition by defining the boundary conditions, material properties, port excitations, meshing frequencies, sweep frequency range, and other related tasks. The code, based on the user requirements could setup the problem, simulate the structure, save the results, and then repeat the procedure with new parameters. This could be of interest in an optimization process. It was found that in many cases such a method was better than the HFSS internal optimizer because the user was not restricted. For the most part this code was not used as an optimizer, but rather a way to automate the drawing of the geometry and setup the problem. HFSS 9.2 was then used to import the HFSS 8.5 project and simulate the problem. This indirect approach was taken because HFSS 9.2 does not support the macro language.

The code was designed to be as general as possible and was applied to the sinuous antennas, the balun designs, and the coupler designs.

Appendix C – Line Characteristic Calculations

These equations are based on the derivations of 'Impedances of Offset Parallel-Coupled Strip Transmission Lines' written by Shelton in [47].

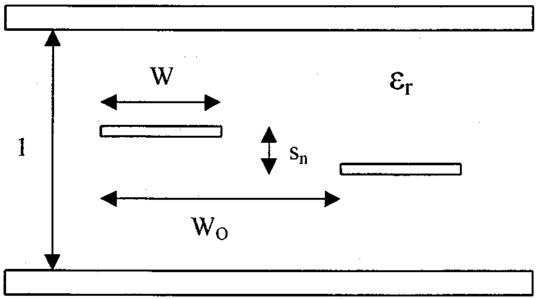

Loose Coupling

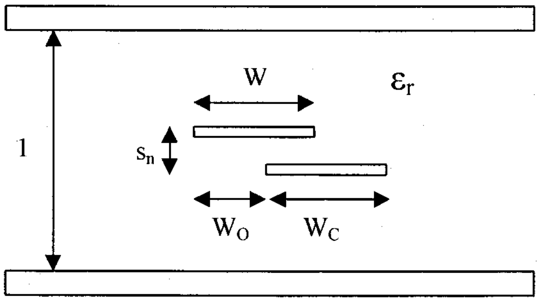

Tight Coupling

$$H_{norm} = 1$$

$$s_{norm} = \frac{H_{norm}}{s/H}$$

$$W_{multiplier} = \frac{H}{H_{norm}}$$

Tight Coupling Equations

$$p = \frac{Z_{0e}}{Z_{0o}}$$

$$A = e^{\left[\frac{60\pi^2}{Z_0\sqrt{\varepsilon_r}}\left(\frac{1-ps_n}{\sqrt{p}}\right)\right]}$$

$$B = \frac{A - 2 + \sqrt{A^2 - 4A}}{2}$$

$$\chi = \frac{(B-1)\left(\frac{1+s_n}{2}\right) + \sqrt{\left(\frac{1+s_n}{2}\right)^2 (B-1)^2 + 4s_n B}}{2}$$

$$r = \frac{s_n B}{\chi}$$

$$C_{fo} = \frac{1}{\pi}\left[\frac{-2}{1-s_n}\log(s_n) + \frac{1}{s_n}\log\left(\frac{\chi r}{(\chi+s_n)(1+\chi)(r-s_n)(1-r)}\right)\right]$$

$$C_o = \frac{120\pi\sqrt{p}}{Z_0\sqrt{\varepsilon_r}}$$

$$W_n = \frac{s_n(1-s_n)}{2}\left(C_o - C_{fo}\right)$$

$$W_{On} = \frac{1}{2\pi}\left[(1+s_n)\log\frac{\chi}{r} + (1-s_n)\log\left(\left(\frac{1+\chi}{s_n+\chi}\right)\left(\frac{r-s_n}{1-r}\right)\right)\right]$$

Finally,

$$W = W_n \cdot W_{multiplier}$$

$$W_O = W_{On} \cdot W_{multiplier}$$

Loose Coupling Equations

$$C_o = \frac{120\pi\sqrt{p}}{Z_0\sqrt{\varepsilon_r}}$$

$$\Delta C = \frac{120\pi}{Z_0\sqrt{\varepsilon_r}} \frac{p-1}{\sqrt{p}}$$

$$k = \frac{1}{e^{\frac{\pi\Delta C}{2}} - 1}$$

$$a = \sqrt{\left(\frac{s_n - k}{s_n + 1}\right)^2 + k} - \left(\frac{s_n - k}{s_n + 1}\right)$$

$$q = \frac{k}{a}$$

$$C_{fo} = \frac{2}{\pi}\left[\frac{1}{1+s_n}\log\left(\frac{1+a}{a(1-q)}\right) - \frac{1}{1-s_n}\log q\right]$$

$$W_c = \frac{1}{\pi}\left[s_n \log\frac{q}{a} + (1-s_n)\cdot\log\left(\frac{1-q}{1+a}\right)\right]$$

$$C_{f(a=\infty)} = -\frac{2}{\pi}\left[\frac{1}{1+s_n}\log\left(\frac{1-s_n}{2}\right) + \frac{1}{1-s_n}\log\left(\frac{1+s_n}{2}\right)\right]$$

$$W_n = \frac{1-s_n^2}{4}\left[C_o - C_{fo} - C_{f(a=\infty)}\right]$$

$$W_{On} = W_n - W_c$$

Finally,

$$W = W_n \cdot W_{multiplier}$$

$$W_O = W_{On} \cdot W_{multiplier}$$

References

[1] L3 Communications – Randtron Antenna Systems. 2000.

[2] J. E. Hershey, 'Wideband antennas – A short survey', General Electric Company, 2000.

[3] J. Il. Kim, 'Log-periodic loop antennas', Blacksburg, Virginia. 1999.

[4] R. C. Johnson, 'Antenna engineering handbook', McGraw-Hill, Inc., 1993. Chapter 14.

[5] V. Rumsey, 'Frequency independent antennas', Academic Press, 1966.

[6] F. T. Ulaby, 'Fundamentals of applied electromagnetics', Prentice-Hall, Inc., New Jersey, 2001.

[7] K. M. P. Aghdam, R. Faraji-Dana, and J. Rashed-Mohassel, 'The sinuous antenna – a dual polarized feed for reflector based searching systems', International Journal of Electronics and Communications, vol. 59. No. 7. 2005.

[8] S. Y. Suh, 'A comprehensive investigation of new planar wideband antennas', PhD Thesis in Electrical and Computer Engineering, Blacksburg, Virginia. 2002.

[9] DuHamel, R. H.: Dual polarized sinuous antennas. U.S. Patent No. 4,658,262, 1987.

[10] W. L. Stutzman and G. A. Thiele, 'Antenna theory and design', 2nd edition, John Wiley & Sons, New York, 1998.

[11] J. D. Kraus, 'Antenna', 2nd edition, McGraw-Hill, Inc., 1988. Chapter 15.

[12] R. H. DuHamel and D. E. Isbell, 'Broadband logarithmically periodic antenna structures', IRE National Convention Record, Part I, pp. 119-128, 1957.

[13] D. E. IsBell, 'Log periodic dipole arrays', *IRE Trans on Antennas and Propagation*, vol. AP-8, pp. 260-267, May 1960.

[14] C. E. Smith, 'Log periodic antenna design handbook', 1st edition, Ohio, 1966.

[15] Ansoft High Frequency Structure Simulator (HFSS), Ansoft Corporation, 2004.

[16] NeuroModeler v. 1.2. Q. J. Zhang, Carleton University, Ottawa, Canada. 2000.

[17] M. C. Buck, D. S. Filipovic, 'Split-beam mode four-arms sinuous antenna', *Antennas and Wireless Propagation Letters*, vol. 3, No. 1. pp. 83-86. 2004.

[18] N. G. Alexopoulos, P. B. Katehi and D. B. Rutledge, 'Substrate Optimization for integrated circuit antennas', *IEEE Transactions on Microwave Theory and Techniques*, vol. 31, pp. 550-557. July. 1983.

[19] B. C. Wadell, 'Transmission line design handbook', Teradyne, Artech House, 1991.

[20] D. M. Pozar and B. Kaufman, 'Increasing the bandwidth of a microstrip antenna by proximity coupling,' *Electronics Letters*, vol. 23, pp. 368-369. April. 1987.

[21] D. M. Pozar, 'Microwave engineering', John Wiley & Sons, 1988.

[22] S. D. Targonski, R. B. Waterhouse and D. M. Pozar, 'Wideband aperture coupled stacked patch antenna using thick substrates', *Electronics Letters*, vol. 32, pp. 1941-1942. Oct. 1996.

[23] R. N. Simons, 'Coplanar waveguide circuits, components, and systems', Ohio, John Wiley & Sons, 2001.

[24] R. Garg, K. Bhartia, I. Bahl, A. Ittipiboon, 'Microstrip antenna design handbook', Arctech House, 2001.

[25] A. A. Oliner, 'Leakage from higher modes on microstrip line with application to antennas', *URSI International Symposium on Electromagnetic Theory*, pp. 25-27. 1986.

[26] A. Petosa, 'Antennas and arrays', Course Notes. ELEC 5607, 2004.

[27] H. Mott, 'Polarization in antennas and radar', John Wiley & Sons, 1986.

[28] M. H. Carpentier, 'Principles of modern radar systems', Artech House, 1988.

[29] R. S. Elliot, 'An introduction to guided waves and microwave circuits', Prentice Hall, 1993.

[30] C. Plett, J. Rogers, 'Radio frequency integrated circuit design', Artech House, 2003.

[31] R. G. Corizine, J. A. Mosko, 'Four-arm spiral antennas', Artech House, 1990.

[32] J. Chang, B. A. Centiner, F. Flaviis, 'A single-arm circular spiral antenna with inner/outer feed circuitry for changing polarization and beam characteristics', *Antennas and Propagation Society International Symposium,* vol. 4, pp. 474-477. June 2003.

[33] J. Thaysen, K. B. Jakobsen, J. Appel-Hansen, 'Characterization and optimization of a coplanar waveguide fed logarithmic spiral antenna', *IEEE-APS Conference on Antennas and Propagation for Wireless Communications*, pp. 25-28. Nov. 2000.

[34] N. Marchand, 'Transmission-line conversion', *Electronics*, pp. 142-145. 1944.

[35] J. W. Duncan and V. P. Minerva, '100:1 Bandwidth balun transformer', *Proc. IRE*, 48, pp. 156-164. 1960.

[36] A. B. Smolders, M.J. Arts, 'Wideband antenna element with integrated balun', Netherlands Foundation for Research in Astronomy (NFRA), *Presented at the IEEE APS int. Symposium Atlanta USA, 1998.*

[37] K. M. P. Aghdam, R. Faraji-Dana, and J. Rashed-Mohassel, 'Optimization of microstrip tapered balun for sinuous antenna feeding circuits', *Antem Conference*, pp. 209-212. 2004,

[38] R. W. Klopfenstein, "A transmission line taper of improved design", *Proceedings of IRE*, vol. 44, No.1, pp. 31-35. Jan. 1956.

[39] M/A-COM, 'RF directional couplers and 3dB hybrids overview'. Application Note M560.

[40] E. G. Cristal and L. Young, 'Theory and tables of optimum symmetrical TEM-mode coupled-transmission line directional couplers,' *IEEE Trans. Microwave Theory & Tech.,* vol. 13, pp. 544-558, Sept. 1965.

[41] E. M. T. Jones and J. T. Bolljahn, 'Coupled-strip-transmission line filters and directional couplers', *IRE Trans. on Microwave Theory and Tech.,* vol. MTT-4 pp. 75-81, April 1956.

[42] R. Levy, 'Tables for asymmetric multi-element coupled Transmission line directional couplers', *IRE Trans. on Microwave Theory and Tech.*, vol. MTT-12, pp. 275-279, May 1964.

[43] J. P. Shelton, R. Van Wagoner, and J. J. Wolf, 'Tandem couplers and phase shifters: A new class of unlimited bandwidth components', *Microwave*, vol. 4, pp. 14-19, April 1965.

[44] C. P. Tresselt, 'The design and construction of broadband, high-directivity, 90-degree couplers using nonuniform line techniques,' *IEEE Trans. on Microwave Theory & Tech.,* vol. MTT-14, pp. 647-656, Dec. 1966.

[45] S. Uysal and A. H. Aghvami, 'Synthesis and design of wideband symmetrical nonuniform directional couplers for MIC applications', *IEEE MTT-S Digest*, pp. 587-590. 1988.

[46] D. C. Youla, 'An introduction to coupled-line network theory', Microwave Research Institute, Polytechnic Institute of Brooklyn, Brooklyn, N. Y., Rept. 960-961, 1961.

[47] J. P. Shelton, 'Impedances of offset parallel-coupled strip transmission lines,' *IEEE Trans.* MTT-1966.

[48] K. M. P. Aghdam, 'Design and construction of dual polarized sinuous and log-periodic antennas in the 2-18GHz frequency range', M.S. Thesis in Electrical Engineering, University of Tehran, Tehran, 2003.

[49] F. Sporleder, H. G. Unger, 'Waveguide tapers transitions and couplers', Peter Peregrinus, 1979.

[50] R. Mongia, I. Bahl and P. Bhartia, *'RF and Microwave Coupled Line Circuits'*, Artech House, Inc., 1999.

[51] Ph. Gonnet, A. Sharaiha, C. Terret, and A. Skrivervik, 'Feeding networks for sinuous antennas', *Microwave and Optical Technology Letters*, vol. 20. No. 3. February 1999.

[52] Q. J. Zhang, K. C. Gupta, 'Neural networks for RF and microwave design', Norwood, MA. Artech House. 2000.

[53] P. Salem, C. Wu, M. C. E. Yagoub, 'Non-uniform tapered ultra wideband directional coupler design and modern antenna system integration', *IEEE MTT-S International Microwave Symposium.* San Francisco, CA. USA. (Pending Acceptance)

[54] P. Salem, C. Wu, M. C. E. Yagoub, 'Neural-based model of spiral antenna radiation patterns for detection of angle of arrival', *IEEE International Workshop on Antenna Technology: Small Antennas and Novel Metamaterials.* White Plains, NY. USA. (Publication Date: March 2006)

[55] P. Salem, C. Wu, M. C. E. Yagoub, 'Novel ultra wideband printed balun design using the FEM and FDTD methods', *IEEE Antennas and Propagation Society International Symposium. Washington*, DC. USA. July 2005.

[56] P. Salem, C. Wu, M. C. E. Yagoub, 'Four arm dual circular polarized sinuous antenna design for 2-18GHz operation', *IASTED International Conference on Antennas, Radar, and Wave Propagation.* Banff, AB. Canada. vol. 2, 377-382. July 2005.

[57] P. Salem, M. C. E. Yagoub, 'Dual polarized sinuous antenna and ultra wideband feed design', Defence Research and Development Canada Contracted Report. Document Number: CR 2005-035. 2005.

[58] P. Salem, M. C. E. Yagoub, 'Use of neural networks to model spiral antenna radiation patterns', Defence Research and Development Canada Contracted Report. Document Number: CR 2005-024. 2005.